DOE F 4600.6#

(09-92)

U.S. DEPARTMENT OF ENERGY

OMB Control No.

1910-0400

FEDERAL ASSISTANCE PROGRAM/PROJECT STATUS REPORT

Replaces EIA-459F

All Other Editions Are Obsolete

OMB Burden Disclosure Statement

Public reporting burden for this collection of information is estimated to average 47.5 hours per response, including the time for reviewing instructions, searching existing data sources, gathering and maintaining the data needed, and completing and reviewing the collection of information. Send comments regarding this burden estimate or any other aspect of this collection of information, including suggestions for reducing this burden, to Office of Information Resources Management, AD-241.2 - GTN, Paperwork Reduction Project (1910-0400), U.S. Department of Energy, 1000 Independence Avenue, S.W., Washington, DC 20585; and to the Office of Management and Budget (OMB), Paperwork Reduction Project (1910-0400), Washington, DC 20503.

1. Program/Project Identification No.	2. Program/Project Title: **FUNDAMENTALS OF NATURAL GAS AND SPECIES FLOWS FROM HYDRATE DISSOCIATION - APPLICATIONS TO SAFETY AND SEA FLOOR INSTABILITY**	3. Reporting Period
DE-FC26-00-NT40916		November 2000 through August 2006

4. Name and Address

Goodarz Ahmadi
Department of Mechanical and Aeronautical Engineering
Clarkson University
Potsdam, NY 13699-5725

5. Program/Project Start Date: November 2000

6. Completion Date: August 2006

7. Approach Changes

None

None

8. Performance Variances, Accomplishments, or Problems

Semi-analytical 1-D and axisymmetric computational models for natural gas flow in the hydrate reservoir were developed. Variations of pressure and temperature profiles, as well as the movement of dissociation front and amount of natural gas production were evaluated.

An experimental setup for formation and dissociation of hydrate, which allows for the visual inspection of the process, was developed. Variations of gas pressure and temperature during hydrate formation and dissociation processes in crushed ice and mixture of crushed ice and glass beads were measured.

Formulation of a thermodynamically consistent model for multiphase liquid-gas flows in porous media was completed. Progress was made in the formulation of a thermodynamically consistent model for multiphase flows during hydrate dissociation.

A computational model for multidimensional analysis of gas hydrate dissociation was developed and the dissociation of a core sample weree analyzed.

9. Open Items

None

10. Status Assessment and Forecast

No Deviation from Plan is Expected

No Deviation from Plan is Expected

11. Description of Attachments

Detail progress report

None

12. Signature of Recipient and Date	13. Signature of U.S. Department of Energy (DOE) Reviewing Representative and Date
Go Goodarz Ahmadi	

DOE DE-FG26-00NT-40916

FINAL REPORT

August 2006

TITLE: **Fundamentals of Natural Gas and Species Flows from Hydrate Dissociation - Applications to Safety and Sea Floor Instability**

PI: Goodarz Ahmadi

INSTITUTION: Clarkson University
Potsdam, NY 13699-5725
Tel: (315) 268-2322
Fax: (315) 268-6438
Email: ahmadi@clarkson.edu

GRANT NO.: DE-FC26-00-NT40916

PROJECT DURATION: November 2000 to August 2006

DISCLAIMER

TITLE: **Fundamentals of Natural Gas and Species Flows from Hydrate Dissociation - Applications to Safety and Sea Floor Instability**

PI: Goodarz Ahmadi

INSTITUTION: Clarkson University
Potsdam, NY 13699-5725
Tel: (315) 268-2322
Fax: (315) 268-6438
Email: ahmadi@clarkson.edu

GRANT NO.: DE-FC26-00-NT40916

PROJECT DURATION: November 2000 to August 2006

DOE Project Officer: Dr. Thomas Mroz

ABSTRACT

Semi-analytical computational models for natural gas flow in hydrate reservoirs were developed and the effects of variations in porosity and permeability on pressure and temperature profiles and the movement of a dissociation front were studied. Experimental data for variations of gas pressure and temperature during propane hydrate formation and dissociation for crushed ice and mixture of crushed ice and glass beads under laboratory environment were obtained.

A thermodynamically consistent model for multiphase liquid-gas flows trough porous media was developed. Numerical models for hydrate dissociation process in one dimensional and axisymmetric reservoir were performed. The computational model solved the general governing equations without the need for linearization.

A detail module for multidimensional analysis of hydrate dissociation which make use of the FLUENT code was developed. The new model accounts for gas and liquid water flow and uses the Kim-Boshnoi model for hydrate dissociation.

TABLE OF CONTENTS

INTRODUCTION

Objectives

The general objective of this project is to provide the needed fundamental understanding of natural gas-water mixture flows in the reservoir during hydrate dissociation. The main goal is to develop an advanced computational capability for handling the safety issues related to natural gas production and pressure buildup during drilling into a hydrate reservoir. The specific objectives are:

- To develop a model for multiphase flows of natural gas and water for application to natural gas production from hydrate dissociation in natural reservoirs.

- To provide reliable data for phasic mean velocities during the dissociation of the propane hydrate in an experimental hydrate chamber.

- To develop an accurate computational capability incorporating the new model for analyzing natural gas, water and/or slurry flows in configurations of interest to natural gas production from hydrate reservoir and during drilling.

- To solve a number of technologically important safety-related problems relevant to gas pressure buildup and gas-water mixture flows during drilling into a reservoir due to hydrate dissociation.

- To verify the validity of the developed model by comparing the predicted results with the experimental data under idealized conditions and the available field observation.

Significance

The current state of understanding of hydrate dissociation process is in its infancy. In particular, the nature of gas-liquid and solid flows in consolidated and unconsolidated sediments during the hydrate dissociation is not well understood. In addition, a satisfactory computational model describing the natural gas production and pressure buildup during the drilling into a hydrate reservoir does not exist. The goal of this project is to provide the needed fundamental understanding of the flow properties and such a computational model. We plan to make use of the thermodynamically consistent modeling approach of multiphase mixture flows, in addition to innovative experimentation. A fundamental understanding of multiphase flow during hydrate dissociation will have a significant impact on the safety of fossil fuel exploration and to the future development of environmentally acceptable hydrate-based energy production.

FINAL TECHNICAL REPORT

Summary

In this section several computer simulations of the hydrate dissociation process in a reservoir are presented and sample results are described. Additional simulation results were published in the peer reviewed journals and/or presented in a number of technical conferences. The report summarizes the semi-analytical analysis of the dissociation process following approximation suggested by Makagon for one dimensional and axisymmetric models of hydrate reservoirs. This is followed by the results of computer simulations of one-dimensional and axysymmetric reservoirs without the linearization. Finally a computational model for multidimensional analysis of the hydrate dissociation process is described and is applied to a hydrate core dissociation case.

The report also includes a description of the theoretical model for flow in poroelastic media and the experimental study of formation and dissociation of propane hydrate.

1. AXISYMMETRIC RESERVOIR CONDITION DURING HYDRATE DISSOCIATION (LINEARIZED MODEL)

We have performed a new study concerning natural gas production with constant well output from a hydrate reservoir. This case is more realistic as in practice the well output is expected to be kept at a constant rate. The case that the reservoir is partially saturated with hydrate and also contains pressurized natural gas is analyzed. The linearized form of the governing equations is used in the analysis. The special case that a well is drilled in an unbounded axisymmetric hydrate reservoir is studied. When the well output is at a fixed rate, a set of self-similar solutions for temperature and pressure distributions in the reservoir can be found. The approach leads to a system of coupled algebraic equations for the location of the decomposition front and the temperature and pressure at the front. This system of equation is then solved by an iterative scheme. Numerical results for time evolutions of pressure and temperature profiles in the hydrate reservoir, as well as the location of the front, are obtained for several well natural gas production rates and reservoir temperatures.

Mathematical Model

In this section, the mathematical formulations of the model for evaluation of pressure and temperature fields are summarized. Consider a hydrate reservoir with a fixed production rate depressurizing well as shown in Figure 1. The governing equation for the pressure

distribution in the reservoir, which is obtained from the continuity equation and Darcy's law, is given as

$$\frac{k_n}{2\Phi_n \mu}\left(\frac{\partial^2 P_n^2}{\partial r^2} + \frac{1}{r}\frac{\partial P_n^2}{\partial r}\right) = \frac{\partial P_n}{\partial t} \tag{1-1}$$

where

$$\Phi_1 = (\,1 - \alpha\,)\,\Phi \tag{1-2}$$

$$\Phi_2 = (1 - \beta\,)\,\Phi \tag{1-3}$$

and r is the radial distance from the well, t is time, μ is the coefficient of viscosity of the gas, k_n is the gas permeability in zone 1 or 2, P_n is the pressure in zone 1 or 2, Φ is the reservoir porosity, α is the water saturation, and β is the hydrate saturation. In Equation (1-1) and in the subsequent analysis, n = 1 corresponds to the gas-region with $r_o < r < R(t)$, and n = 2 denotes the hydrate-region with $R(t) < r < \infty$. Here R(t) is the distance of the dissociation front from the center of well, and r_o is the well radius.

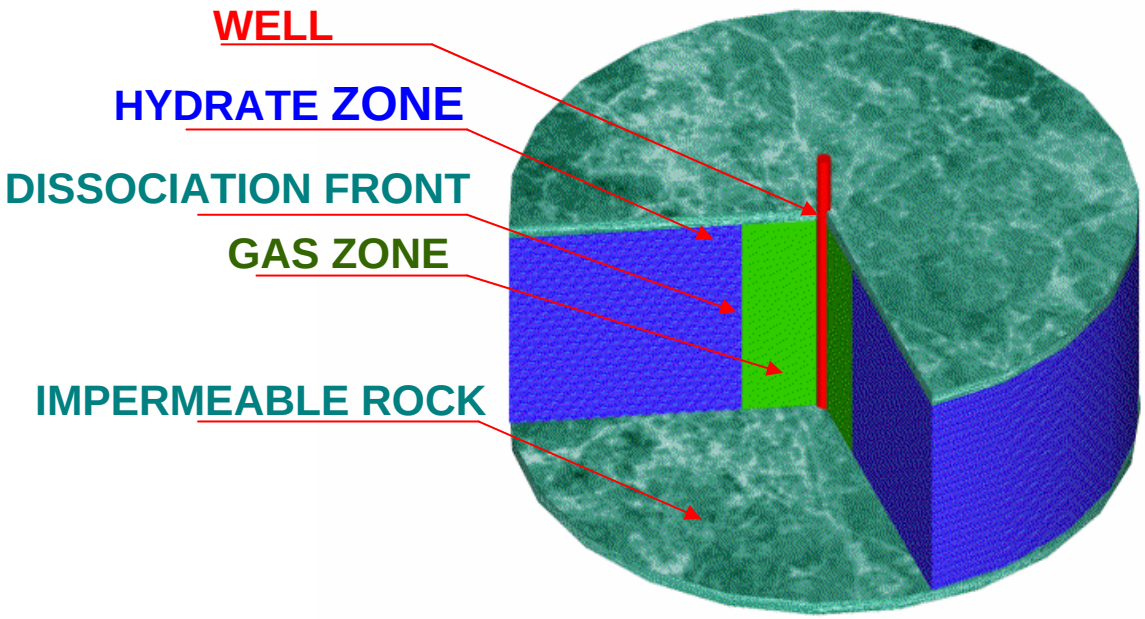

Figure 1. Schematics of a hydrate reservoir with a depressurizing front.

The relation between dissociation temperature T_D and pressure P_D at the decomposition front for phase equilibrium between natural gas and hydrate is given as

$$\log_{10} P_D = a\,(T_D - T_o) + b\,(T_D - T_o)^2 + c \tag{1-4}$$

where T_o is 273.15K and a, b and c are empirical constants that depend on the hydrate composition. Values of a, b, and c are obtained using the least square error fit to the equilibrium pressure-temperature data for methane hydrate (Makogon, 1997, Ji et al. 2000). i.e.,

$$a = 0.0342\ K^{-1},\ b = 0.0005\ K^{-2},\ c = 6.4804$$

where in Equation (1-4) P_D is in Pa.

Ji et al. (2000) showed that the prediction of Equation (1-4) is in good agreement with the data of Marshal et al. (1964). The mass balance for gas at the decomposition front at the distance of R(t) from the well is given as

$$\rho_1 \upsilon_1 - \rho_2 \upsilon_2 = -[\beta\varepsilon\rho_3 - (1-\alpha)\rho_1 + (1-\beta)\rho_2]\Phi\frac{dR}{dt} \tag{1-5}$$

where ρ_1 is the density of natural gas in zone 1, ρ_2 is the density of natural gas in zone 2, and ρ_3 is the density of hydrate, and ε is the mass fraction of methane gas in the hydrate. Here υ_1 and υ_2 are, respectively, the velocities of natural gas at the dissociation front in zones 1 and 2.

The densities of the natural gas in zone 1 and 2 at the dissociation front are described by the same equation:

$$\rho_1(R,t) = \rho_2(R,t) = \rho_0 \frac{P_D T_0}{z P_0 T_D} \tag{1-6}$$

where z is the gas compressibility (deviation) factor, and ρ_o is the gas density at standard pressure P_o and temperature T_o. Insertion of (1-6) into (1-5) gives

$$\upsilon_1(R,t) - \upsilon_2(R,t) = -[\varepsilon\beta\frac{\rho_3 P_0 T_D}{\rho_0 P_D T_0} z - (\beta - \alpha)]\Phi\frac{dR}{dt} \tag{1-7}$$

Similarly, the mass balance equation for water is:

$$\rho_W \Phi \alpha = (1-\varepsilon)\rho_3 \Phi \beta \tag{1-8}$$

where ρ_W is the density of water.

The temperature field is governed by the convective-conductive heat transfer equation

$$\frac{a_n}{r}\frac{\partial}{\partial r}\left(r\frac{\partial T_n}{\partial r}\right) = \frac{\partial T_n}{\partial t} - \frac{c_v k_n}{c_n \mu}\frac{\partial P_n}{\partial r}\left(\frac{\partial T_n}{\partial r} - \delta\frac{\partial P_n}{\partial r}\right) - \eta\frac{\Phi_n c_v}{c_n}\frac{\partial P_n}{\partial t} \tag{1-9}$$

Here a_n is the heat diffusivity, c_n is the heat capacity, c_v is the constant volume heat capacity of gas, δ is the throttling coefficient, and η is the adiabatic coefficient of the gas. Note that the Joule-Thompson throttling process is accounted for in Equations (1-1 to 1-9).

For wells with a fixed natural gas output, Q, the boundary conditions are

$$Q = 2\pi r_0 h\frac{k_1}{\mu}\left[\rho\frac{\partial P_1}{\partial r}\right]_{r=r_0} = \frac{\pi k_1 h}{\mu}\frac{\rho_0}{P_0}\left[r\frac{\partial P_1^2}{\partial r}\right]_{r=r_0} = \frac{\pi k_1 h}{\mu}\frac{\rho_0}{P_0}c_1 \tag{1-10}$$

$$P_2(r,0) = P_2(\infty,t) = P_e \tag{1-11}$$
$$P_1(R(t),t) = P_2(R(t),t) = P_D(T_D) \tag{1-12}$$
$$T_2(r,0) = T_2(\infty,t) = T_e \tag{1-13}$$
$$T_1(R(t),t) = T_2(R(t),t) = T_D \tag{1-14}$$

where h is the thickness of the hydrate reservoir and c_1 is a constant (related to the pressure gradient at the well wall. As noted before, it is assumed that the dissociation front is at the equilibrium pressure and temperature (P_D and T_D) for dissociation of the hydrate

Linearization and Self-Similar Solution

To be able to obtain similar solutions, the governing equations must be first linearized. Here the reservoir and the dissociation pressures are, respectively, used to linearize the pressure equation in the hydrate and the gas zones. That is, using the approximation

$$\frac{\partial P_1^2}{\partial t} \approx 2P_D\frac{\partial \overline{P}_1}{\partial t} \qquad \frac{\partial P_2^2}{\partial t} \approx 2P_e\frac{\partial \overline{P}_2}{\partial t} \tag{1-15}$$

Equation governing the pressure variation may then be linearized as:

$$\frac{\partial \overline{P}_n^2}{\partial r^2} + \frac{1}{r}\frac{\partial \overline{P}_n^2}{\partial r} = \frac{1}{\chi_n}\frac{\partial \overline{P}_n^2}{\partial t} \tag{1-16}$$

where

$$\chi_1 = \frac{k_1 P_D}{\mu \Phi_1} \qquad \chi_2 = \frac{k_2 P_e}{\mu \Phi_2} \tag{1-17}$$

Self-similar solutions of Equation (1-16) with appropriate boundary conditions are:

$$\overline{P}_1^2 = P_D^2 - \frac{Q\mu}{2\pi k_1 h}\frac{P_0}{\rho_0}\left[E_i(-\lambda_1^2) - E_i(-\alpha_1^2)\right] \tag{1-18}$$

$$\overline{P}_2^2 = P_e^2 - (P_e^2 - P_D^2)\frac{E_i(-\lambda_2^2)}{E_i(-\alpha_2^2)} \tag{1-19}$$

where

$$E_i(-\xi) = -\int_{\xi}^{\infty} \frac{e^{-u}}{u} du \tag{1-20}$$

$$\lambda_1 = \frac{r}{2\sqrt{\chi_1 t}} \qquad \lambda_2 = \frac{r}{2\sqrt{\chi_2 t}} \tag{1-21}$$

$$\alpha_1 = \sqrt{\frac{\gamma}{4\chi_1}} \qquad \alpha_2 = \sqrt{\frac{\gamma}{4\chi_2}} \tag{1-22}$$

Under the condition that the hydrate reservoir contains free natural gas, neglecting the conductive heat transfer in the porous media, which is several orders of magnitude smaller than the convective heat transfer, the heat transfer equation becomes

$$\frac{\partial T_n}{\partial t} = \frac{c_v k_n}{c_n \mu}\frac{\partial P_n}{\partial r}\left(\frac{\partial T_n}{\partial r} - \delta\frac{\partial P_n}{\partial r}\right) + \eta\frac{\Phi_n c_v}{c_n}\frac{\partial P_n}{\partial t} \tag{1-23}$$

Similarly**,** solutions to the linearized form of Equation (1-23) satisfying the appropriate thermal boundary conditions are:

$$T_1 = T_D + A_1\delta\left[E_i(-\lambda_1^2) - E_i(-\alpha_1^2) + (\frac{\eta}{\delta}B_1 - 1)(\Psi_1(\lambda_1^2) - \Psi_1(\alpha_1^2))\right] \tag{1-24}$$

$$T_2 = T_e + A_2\delta\left[E_i(-\lambda_2^2) - (\frac{\eta}{\delta}B_2 - 1)\Psi_2(\lambda_2^2)\right] \tag{1-25}$$

where

$$\Psi_1(\xi) = \int_0^{\xi} \frac{e^{-\eta}}{\eta + C_1 e^{-\eta}} d\eta \qquad \Psi_2(\xi) = \int_{\xi}^{\infty} \frac{e^{-\eta}}{\eta + C_2 e^{-\eta}} d\eta \tag{1-26}$$

$$A_1 = \frac{Q\mu P_0}{4\pi P_D k_1 \rho_0 h}; \qquad A_2 = -\frac{1}{2E_i(-\alpha_2^2)} \frac{P_e^2 - P_D^2}{P_e} \tag{1-27}$$

$$B_1 = \frac{\Phi_1 c_v}{c_1}; \qquad B_2 = \frac{\Phi_2 c_v}{c_2} \tag{1-28}$$

$$C_1 = \frac{Qc_v P_0}{4\pi P_D c_1 \chi_1 h \rho_0}; \qquad C_2 = -\frac{P_e^2 - P_D^2}{P_e} \frac{c_v}{c_2} \frac{1}{2E_i(-\alpha_2^2)} \frac{k_2}{\mu \chi_2} \tag{**1**-29}$$

The values of pressure P_D and temperature T_D at the dissociation front, and the constant γ, which determines the motion of the decomposition front, are still unknown and must be evaluated numerically for a given set of conditions. From the evaluation of Equation (1-25) at the decomposition front (i.e. $\lambda_2 = \alpha_2$), it followed that

$$T_D = T_e + A_2 \delta [E_i(-\alpha_2^2) - (\frac{\eta}{\delta} B_2 - 1)\Psi_2(\alpha_2^2)] \tag{1-30}$$

The equilibrium pressure P_D and the equilibrium temperature T_D are related. Using Equations (18) and (19), the balance of mass at the decomposition front becomes:

$$Q\frac{P_0}{\pi} \frac{e^{-\alpha_1^2}}{h\rho_0} + \frac{2k_2}{\mu}(P_e^2 - P_D^2) \frac{e^{-\alpha_2^2}}{E_i(-\alpha_2^2)} = A\gamma \tag{1-31}$$

where

$$A = [\varepsilon\beta \frac{\rho_3 P_0 T_D}{\rho_0 T_0} z - (\beta - \alpha) P_D]\Phi \tag{1-32}$$

Equation (1-31) may be used to determine the constant γ. Equations (1-31) and (1-32) and the relationship between the dissociation temperature and pressure given given by Equation (1-4) are three nonlinear coupled equations for determining γ, T_D and P_D.

The linearization model described in this section that was suggested by Makogon (1997) assumes that the heat convection dominates the conduction and the neglects the heat conduction in the entire reservoir. While this assumption is reasonable away from the dissociation front, it does not allow for the energy balance at the dissociation front to be

enforced. Despite this important limitation of the approach, the linearization method provides for a convenient (semi-analytical) method for studying many features of the natural gas production from hydrate reservoirs.

Results

In this section, results for the time evolution of pressure and temperature profiles in the hydrate reservoir due to the presence of a well with different fixed natural gas outputs are presented. In addition, time variations of location of the dissociation front are also evaluated. An initial reservoir pressure of 15MPa is used in these simulations. For different values of well-output and initial reservoir temperatures, the solutions to Equations (1-31)-(1-33) are obtained. The resulting values of the dissociation temperature and pressure at the front and of the parameter γ (with an error bound of 0.1%) are listed in Table 1. Here the permeability in the gas zone is 5.2 md and the hydrate zone permeability is 0.4 md.

Table 1. Values of dissociation temperature and pressure and parameter γ for different natural gas production rates for a reservoir with k_1=5.2 md and k_2=0.4 md.

P_e (MPa)	T_e (K)	Natural Gas Output(kg/s)	T_D (K)	P_D (MPa)	γ (m^2/sec)
15	283	0.03	277.25	4.314	1.61×10^{-6}
15	285	0.03	279.46	5.526	2.45×10^{-6}
15	287	0.04	281.96	6.65	2.71×10^{-5}
15	287	0.03	281.96	6.647	4.67×10^{-6}
15	287	0.02	281.93	6.628	1.4×10^{-7}
15	287	0.01	281.92	6.61	2.51×10^{-8}

When the reservoir pressure, temperature and production rates are specified, the present linearized axisymmetric model leads to fixed values of dissociation-front pressure and temperature. The well pressure, however, changes gradually with time. Table 1 shows that for a fixed reservoir temperature of 287K, when the natural gas output decreases, the dissociation pressure and temperature decrease slightly. The value of parameter γ, which controls the movement of the dissociation front, however, decreases sharply as the gas production decreases. The dissociation pressure and temperature are sensitive functions of reservoir temperature. When the gas production is kept fixed at 0.03 kg/s, a decrease of 2K in the reservoir temperature drops the dissociation pressure by about 17%. In this case, parameter γ also decreases with the decline of reservoir temperature.

For a reservoir temperature of 287K and a natural gas production rate of 0.04 kg/s, variations of decomposition temperature and pressure, and parameter γ with zone permeability are shown in Table 2. When the permeability in the gas zone is fixed at 5.2 md,

as the hydrate zone permeability decreases from 3 md to 0.4 md, the dissociation pressure and temperature decrease slightly, while parameter γ increases sharply. This is because, when the hydrate zone permeability is low, the amount of hydrate that needs to dissociate increases to maintain the well gas flow at a fixed rate. When the permeability in the hydrate zone is fixed, variations of gas zone permeability have a very slight effect on the dissociation temperature, pressure and parameter γ. As noted before, here the natural gas output is fixed, and therefore, the equilibrium conditions at the front do not change appreciably. The main effect of variations of gas zone permeability is on the temperature and pressure profiles, which will be discussed later.

Table 2. Values of dissociating temperature and pressure and parameter γ for a natural gas production rate of 0.04 kg/s for different zone permeabilities

P_e (MPa)	Permeability of gas zone(md)	Permeability of Hydrate zone(md)	T_D (K)	P_D (MPa)	γ (m^2/sec)
15	5.2	3	282.038	6.7	4.96×10^{-10}
15	5.2	1	281.976	6.66	2.5×10^{-8}
15	5.2	0.6	281.964	6.65	2.9×10^{-6}
15	5.2	0.4	281.963	6.65	2.71×10^{-5}
15	1	1	281.978	6.66	2.51×10^{-8}

For a reservoir temperature of 287K and a natural gas production rate of 0.04kg/s, Figure 2 shows variations of pressure and temperature profiles at different times. Here the case that the permeabilities in the hydrate and gas zones are, respectively, 5.2 md and 0.4 md is consider. As noted before, the hydrate reservoir is divided into two zones by the dissociation front, and the temperature variations in the two zones are quite different. Figures 2a and 2b show that the temperature decreases gradually from the undisturbed reservoir value far from the front to the dissociation temperature at the front. In the gas zone, the temperature varies gradually near the dissociation front, but decreases sharply to its minimum values at the well. The temperature profiles in the hydrate and the gas zones are also self-similar, and evolve with time as the decomposition front moves outward.

The corresponding pressure profiles for different times under the same conditions for the far and the near fields are presented in Figures 2c and 2d. The pressure decreases gradually from the reservoir pressure to the decomposition pressure at the front, and then decreases toward the well to its minimum value at the well. Near the well, the pressure gradient becomes quite high.

For the present case where the permeability of the gas zone is thirteen times that of the hydrate zone, the change in the slope of the pressure profile at the dissociation front can be clearly seen from Figure 2c. This is quite different from the one-dimensional model of Ji et al. (2000), in which the gradient change at the front was hardly noticeable. It should be emphasized that in the earlier study of Ji et al. (2000), the permeability in the gas zone was almost the same as that in the hydrate zone**.** Figure 2c also shows that the pressure profiles for different times are self-similar in each zone, and expand outward as the dissociation front moves away from the well.

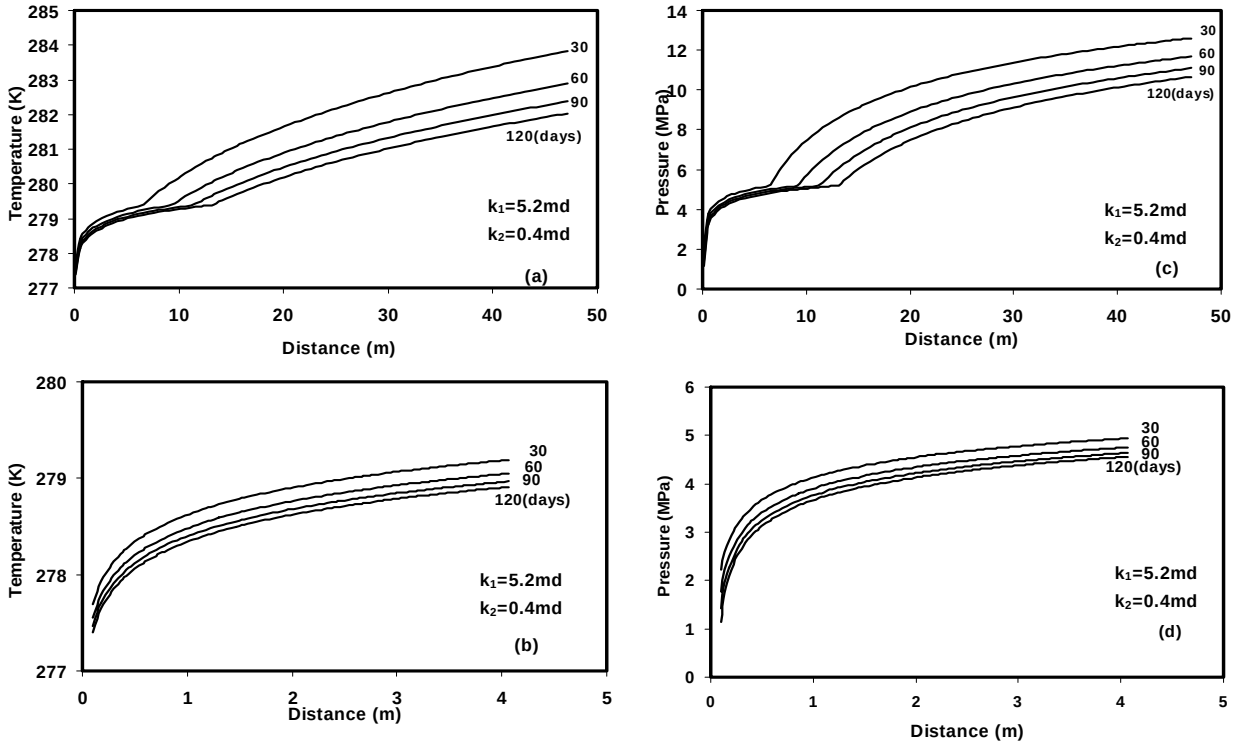

Figure 2. Time variations of pressure and temperature profiles for a reservoir temperature of 287K and a well natural gas output of 0.04kg/s. (a), (c) extended field. (b),(d) near-well.

Figure 2d shows that the pressure at the well drops with time when the natural gas output is kept fixed (at 0.04kg/s). That is, to maintain a constant gas output, the well pressure must be reduced continuously with time. Obviously, this can not continue forever, and after certain time, the pressure at the well becomes too low to allow maintaining a constant flow rate.

For a natural gas production rate of 0.04 kg/s, the time evolutions of the gas mass flux (**D**v) and the total mass flow (2**B**r**D**v) across the reservoir are displayed, respectively, in Figure 3a and 3b. Figure 3a shows that the gas mass flux increases toward the well, and the variation in each zone is roughly time independent. This figure also clearly shows the details of natural gas production at the dissociation front. At the front, there is a jump in the mass flux due to hydrate decomposition. The jump moves outward with time as the decomposition front penetrates deeper into the hydrate reservoir.

Mass flux and total mass flow profiles for a reservoir temperature of 287K and a well natural gas output of 0.04kg/s are shown in Figure 3. Figure 3b shows the time variation of the total mass flow per unit length at a radial distance of r from the well. The total mass flow profiles in the hydrate and the gas zones remain roughly fixed, except for the jump at the dissociation front. This figure clearly shows the variation of the amount of natural gas generated by hydrate dissociation at the front. There is also a slight decrease in the gas flow in the hydrate zone that is compensated by the slight increase in the gas production by dissociation at the front. Figure 3a indicates that the mass flux due to hydrate dissociation decreases with time. On the other hand, Figure 3b indicates that the total mass flow due to hydrate dissociation remains fixed (or increases slightly) with time.

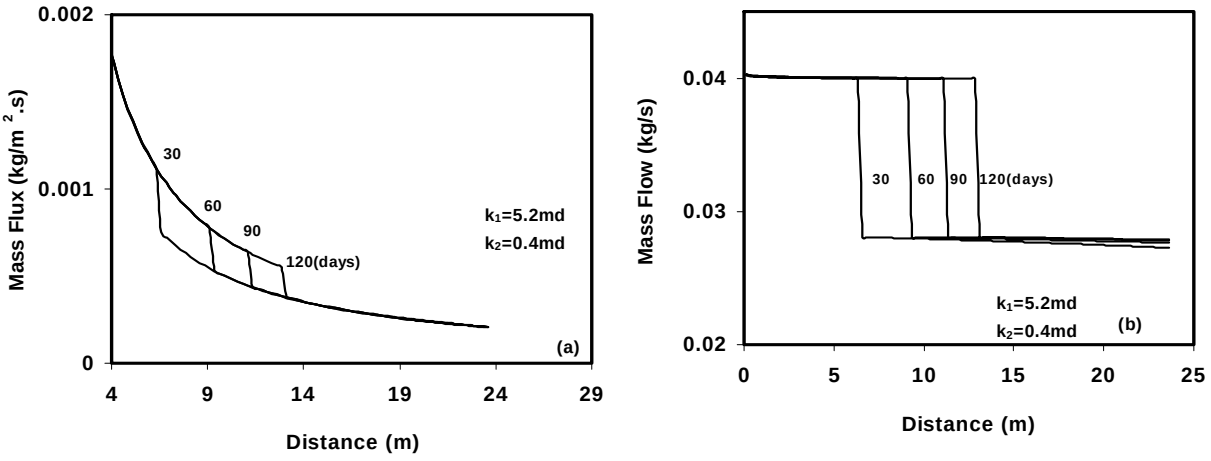

Figure 3. Mass flux and total mass flow profiles for a reservoir temperature of 287K and a well natural gas output of 0.04kg/s.

Figure 4 shows the pressure and temperature profiles for a natural gas production rate of 0.03kg/s in a reservoir with permeabilities in the hydrate and gas zones being equal to 5.2md and 0.4md. The reservoir pressure and temperature are kept constant at 15 MPa and 287 K. This figure shows that large pressure and temperature gradients occur near the front on the hydrate side. The pressure and temperature in the gas region then decrease gradually

toward their minimum values at the well. The pressure and temperature profiles in gas zone in Figure 4 are similar to those shown in Figure 2 with certain differences. In addition to the slower movement of the dissociation front for the lower well output in this case, the temperature and pressure gradients near the well become more gradual. Comparing Figures 2d and 4d shows that the time variation of the well pressure also becomes much slower when the gas output decreases. This implies that a constant well output of 0.03 kg/s can be maintained for a much longer time period when compared to that of 0.04 kg/s.

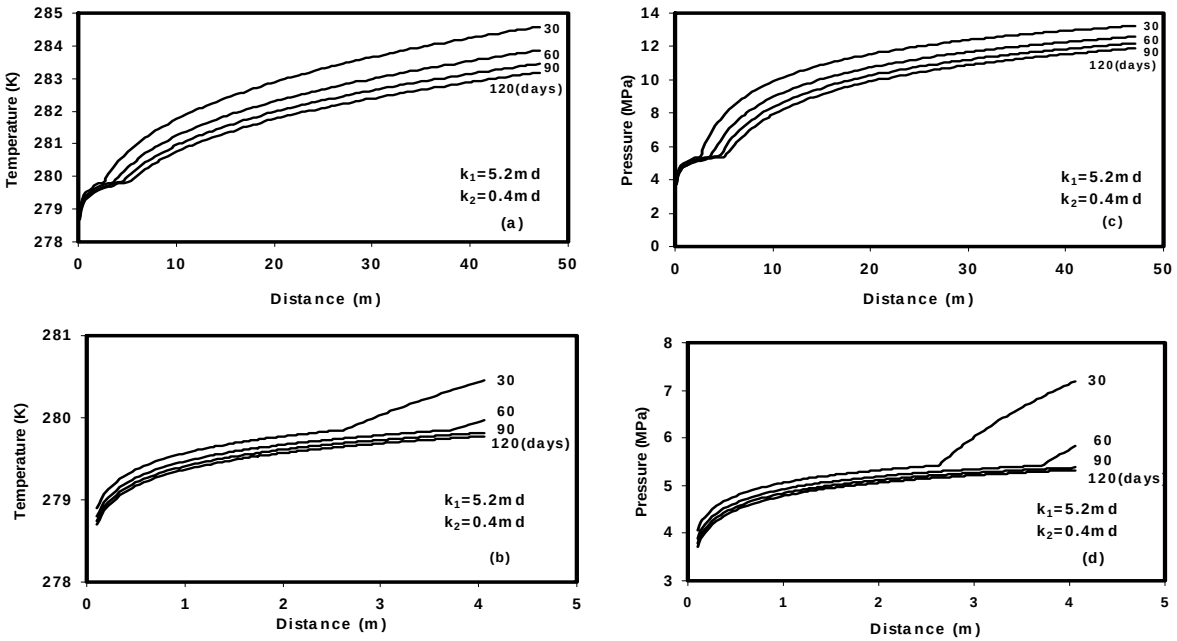

Figure 4. Time variations of pressure and temperature profiles for a reservoir temperature of 287K and a well natural gas output of 0.03kg/s. (a),(c) extended field. (b),(d) near-well.

Time evolutions of mass flux and total mass flow in the reservoir for a well output of 0.03 kg/s are shown in Figure 5. Except for the lower magnitudes, the mass flux and the total mass flow profiles are quite similar to those shown in Figure 3. The details of the hydrate dissociation at the front and the motion of the front can also be seen from this figure.

Under the same reservoir conditions, when the natural gas output is fixed at 0.02 kg/s, Figure 6 shows that the dissociation front moves at a much slower rate. Other features of pressure and temperature profiles in the hydrate zone are similar to those for higher well gas outputs. In this case, however, the pressure and temperature profiles in the hydrate zone have sharp gradients near the front. Figures 6b and 6d show the details of temperature and pressure profiles near the well. The temperature and pressure vary smoothly toward the well and decrease slightly with time. The corresponding mass flux and mass flow profiles are shown in Figure 7. The general features of these profiles are similar to those for higher well outputs.

In this case, however, the dissociation front moves only a few meters after 120 days, but similar jumps in the mass flux and mass flow rate are observed.

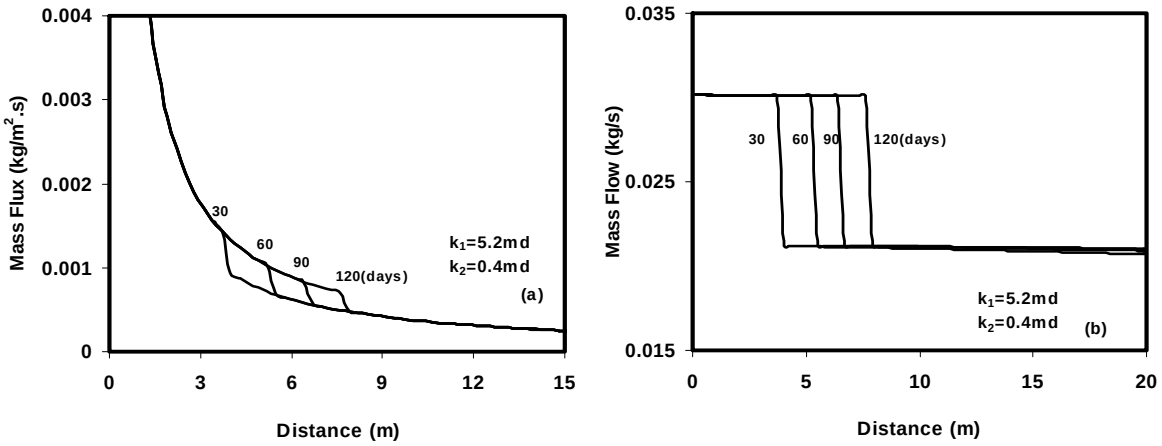

Figure 5. Mass flux and total mass flow profiles for a reservoir temperature of 287K and a well natural gas output of 0.03kg/s.

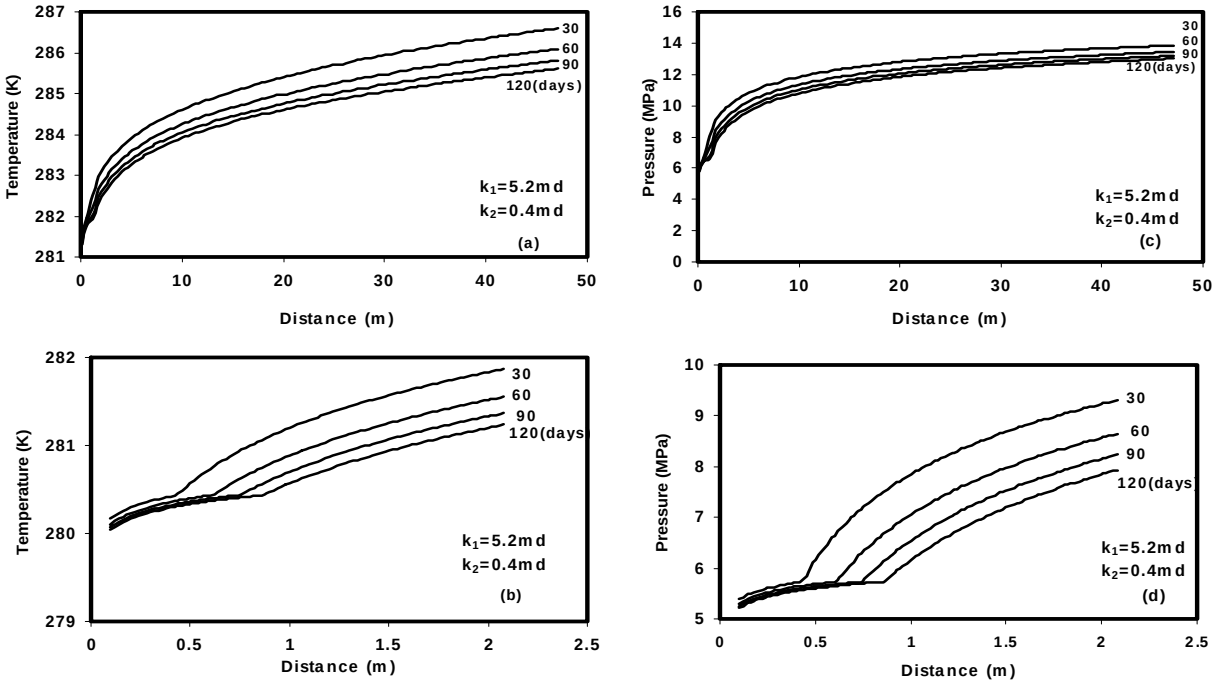

Figure 6. Time variations of pressure and temperature profiles for a reservoir temperature of 287K and a well natural gas output of 0.02kg/s. (a),(c) extended field. (b),(d) near-well.

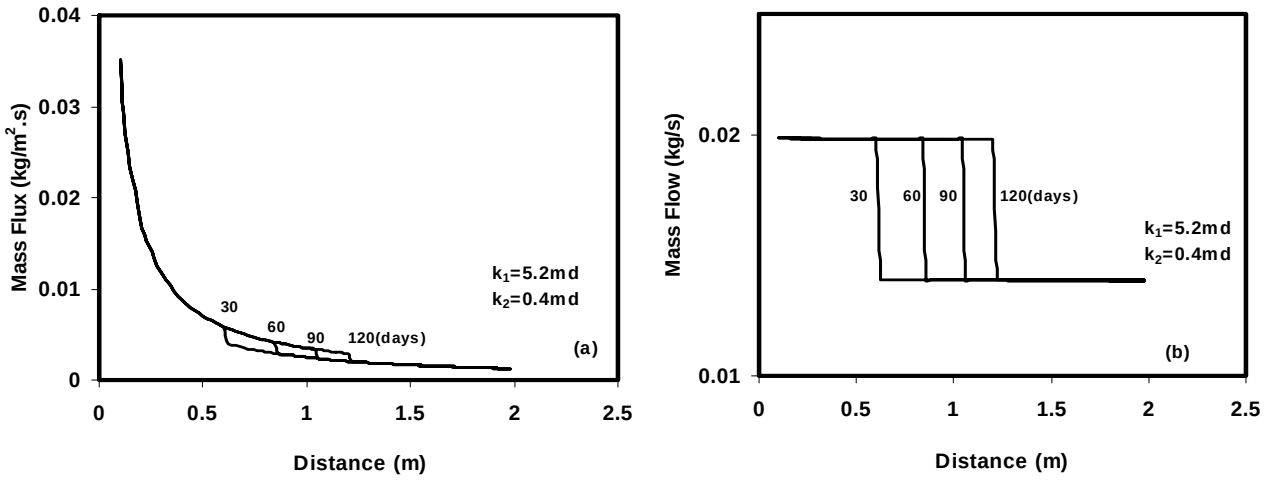

Figure 7. Mass flux and total mass flow profiles for a reservoir temperature of 287K and a well natural gas output of 0.02kg/s.

For the case that the natural gas output is kept fixed at 0.03kg/s, for a reservoir temperature of 285 K (2 K lower that the case shown in Figure 4), the pressure and temperature profiles are presented in Figure 8. The zone permeabilities are also kept the same. While the general features of the pressure and temperature profiles in Figure 8 are similar to those shown in Figure 4, the dissociation pressure and temperature at the front are somewhat smaller. The movement of the front has also noticeably slowed down for this lower-temperature reservoir. This observation further emphasizes the importance of heat transfer for hydrate dissociation and natural gas production processes. In this axisymmetric model, the heat required for hydrate dissociation must be supplied by the hydrate reservoir. Therefore, the reservoir temperature becomes an important controlling parameter. It should be emphasized that, for thin hydrate reservoirs, heat could also be supplied from the lower warmer region, which would significantly affect the natural gas production process.

Figure 9 shows the temperature and pressure profiles when the reservoir temperature is 283K, the other reservoir conditions are kept fixed, and the well output is 0.03 kg/s. Compared with Figure 4 and Figure 8, it is seen that the temperature and the pressure profiles are quite similar. However, due to the lower decomposition temperature and pressure, the rate of reduction of pressure at the well increases. In particular, Figure 9d shows that the well pressure becomes too low at about 120 days to maintain a constant gas output of 0.03 kg/s. Therefore, as the reservoir temperature decreases, the time duration that a fixed natural gas output can be maintained becomes shorter.

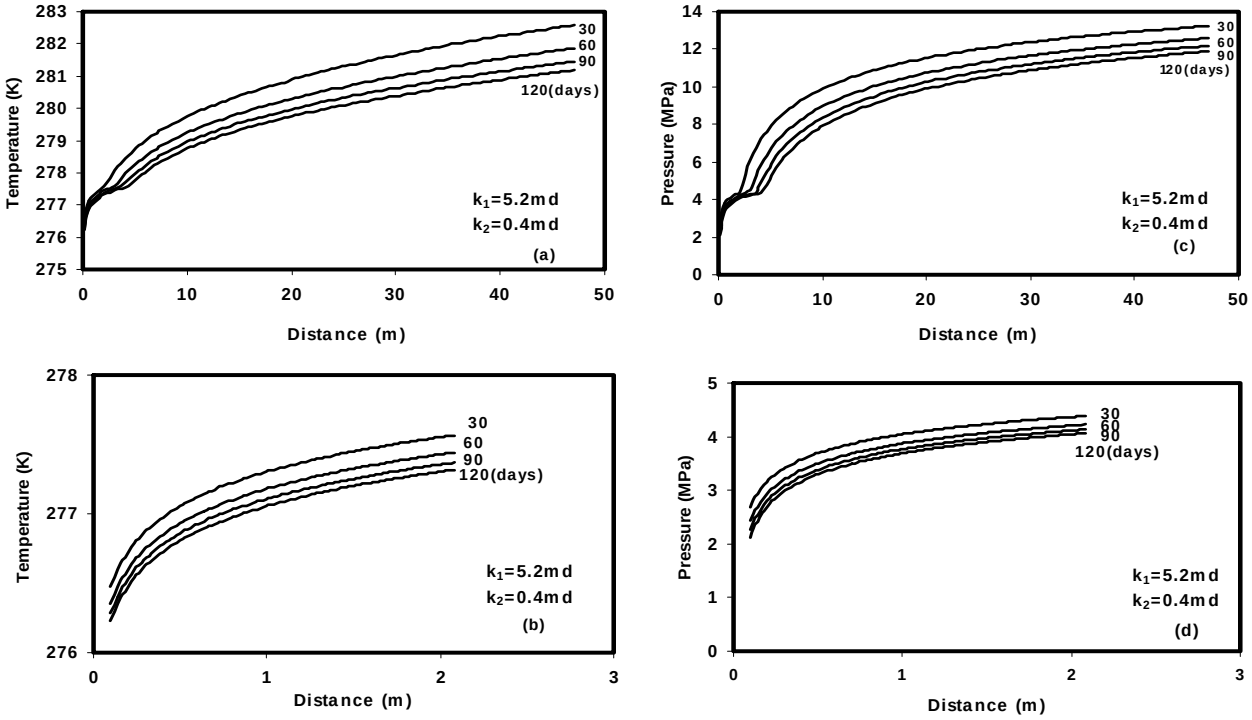

Figure 8. Time variations of pressure and temperature profiles for a reservoir temperature of 285K and a well natural gas output of 0.03kg/s. (a),(c) extended field. (b),(d) near-well.

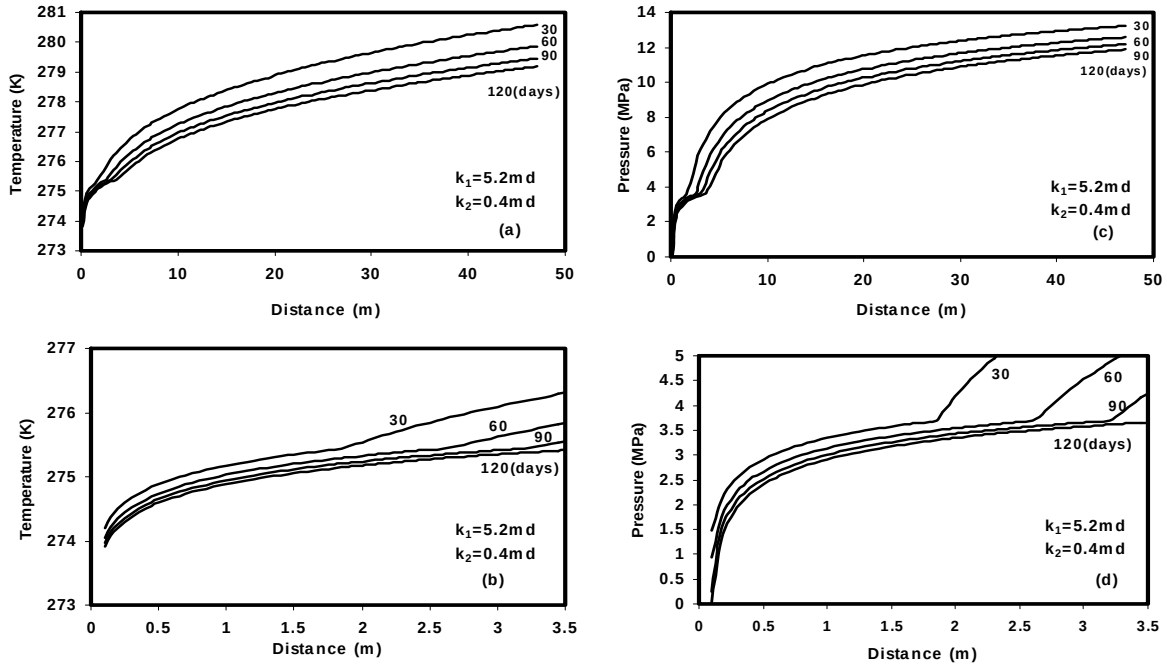

Figure 9. Time variations of pressure and temperature profiles for a reservoir temperature of 283K and a well natural gas output of 0.03kg/s. (a),(c) extended field. (b),(d) near-well.

Mass flux and mass flow profiles for reservoir temperatures of 283 K and 285 K are compared in Figure 10. While the mass flux jumps for different reservoir temperatures are comparable, the decomposition front moves faster as when the reservoir temperature is higher. Comparing Figures 5 and 10 shows the same trend of variations.

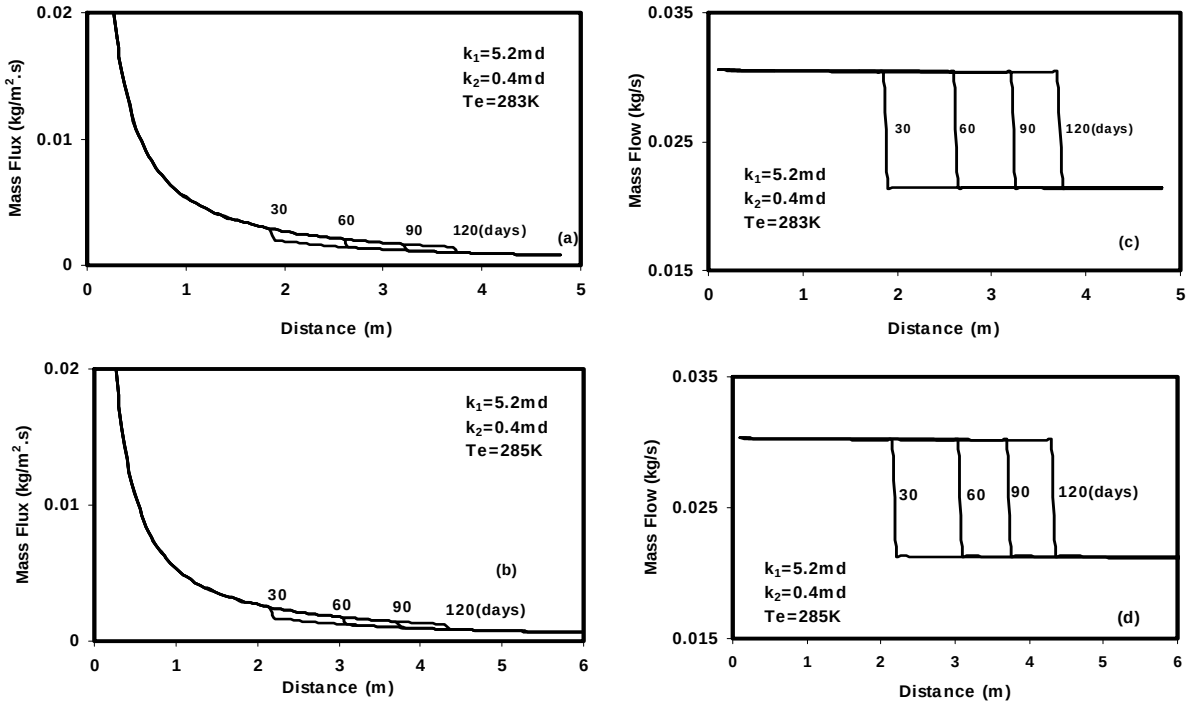

Figure 10. Mass flux and total mass flow profiles for a reservoir pressure of 15 MPa and a well natural gas output of 0.03kg/s with different reservoir temperatures.

Effect of variations in zone permeability on the reservoir temperature and pressure profiles are shown in Figure 11. Here the case that the reservoir temperature is 287K and the natural gas output is 0.04kg/s is studied. Figure 11a and 11b shows the profile for the case that the permeabilities in the gas and hydrate zones are both 1 md. In this case the temperature has a smooth decreasing trend in the hydrate zone and decreases with a sharper slope in the gas zone. The pressure shows a gradual reduction in the entire reservoir, but with a sharper slope in the gas zone. Similar to the one-dimensional case reported by Ji et al. (2000), it is rather difficult to identify the change in slope in the pressure profile at the front when the zone permeabilities are equal.

Figures 11c and 11d show the profiles when the permeability in gas zone is 5.2 md and the hydrate zone permeability is 1 md. In this case, there is an obvious pressure gradient change at the dissociation front. From Equation (5), we expect that the gas flow out of front

into the gas zone should be larger than the gas flow into the front from hydrate zone. While at the dissociation front, the pressure gradient at the hydrate side is larger than that at the gas side difference in the zone permeability compensate and the flow rate is larger on the gas side.

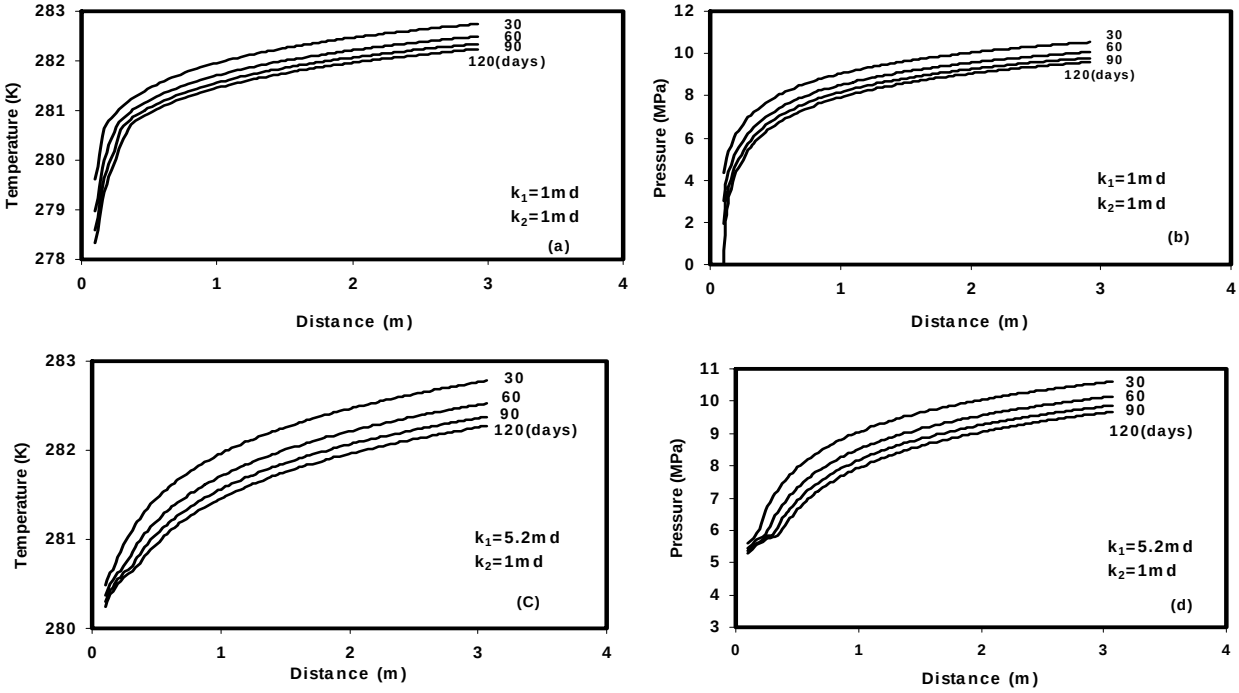

Figure 11. Time variations of pressure and temperature profiles for a reservoir temperature of 287K and a well natural gas output of 0.04kg/s with different permeabilities.

Figure 12 shows the effect of gas zone permeability on the mass flux and total mass flow profiles. The reservoir conditions are identical to those for Figure 11. Comparing Figures 12a and 12c indicates that the variation of gas zone permeability has little effect on the mass flux and total mass flow profiles, as well as the location of dissociation front. This observation shows that the variation of gas zone permeability only affects the reservoir temperature and pressure profiles, and its effect on hydrate dissociation at the decomposition front is slight.

Comparing Figures 3 and 12 shows that the hydrate zone permeability significantly affects the natural gas total mass flow profiles. For $k_2 = 0.4$ md, the front is at 15 m after 90 days, while for a reservoir with $k_2 = 1$ md the dissociation front is at about 0.5 m from well. That is, at a constant well mass flow rate, smaller k_2, will lead to a faster penetration of the front into the reservoir. This is because more hydrate needs to be dissociated to compensate for the lower gas flow rate in the hydrate zone.

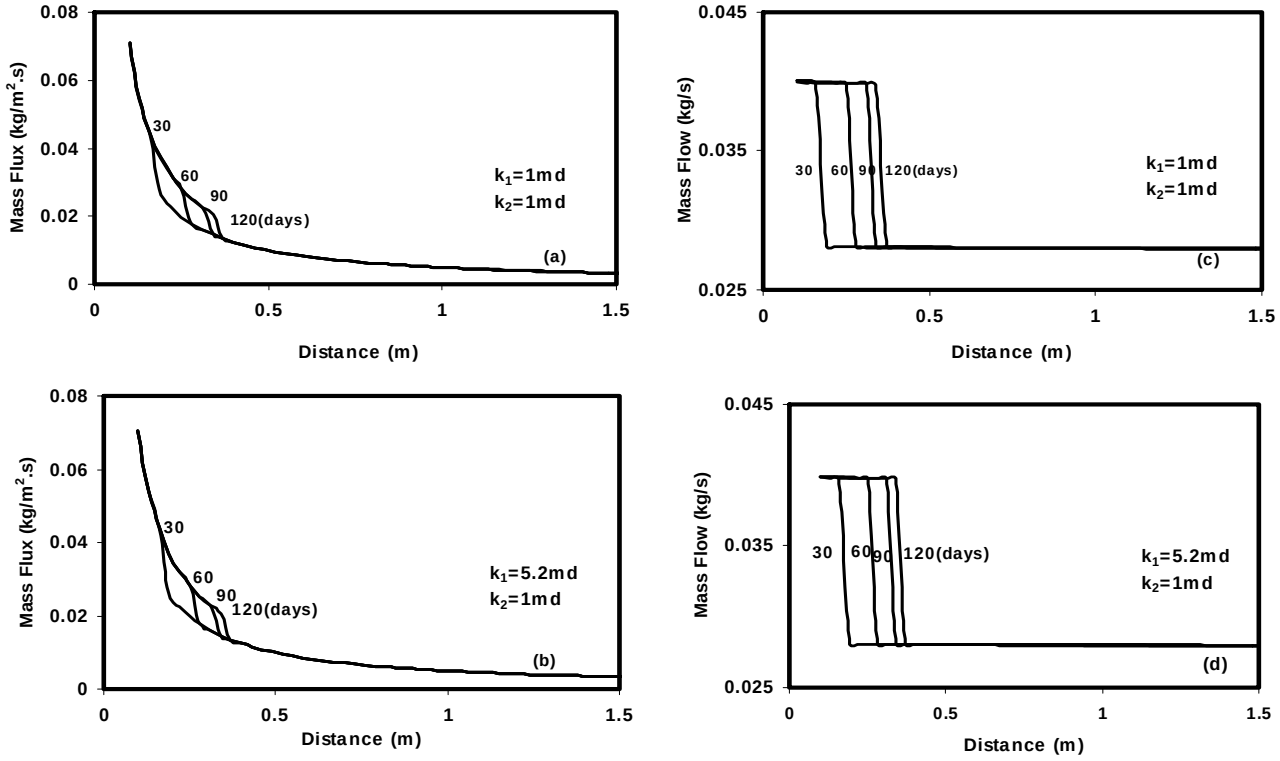

Figure 12. Mass flux and total mass flow profiles for a reservoir temperature of 287K and a well natural gas output of 0.04kg/s for different permeabilities.

Figure 13 shows the movement of the dissociation front for different natural gas outputs. Here the reservoir conditions are assumed to be fixed at 15 MPa and 287 K. The permeabilities in gas and hydrate zones are, respectively, 5.2 md and 0.4 md. Figure 13 shows that the distance of the front from the well increases proportional to the square root of time. As the natural gas output increases, the outward motion of the front speeds up.

For a fixed reservoir pressure and a natural gas output of 0.03 kg/s, time evolutions of dissociation front for different reservoir temperatures are shown in Figure 14. It is observed that at higher reservoir temperature the dissociation front moves away from the well at faster speed. At a fixed flow rate, a higher reservoir temperature leads to higher level of hydrate dissociation that causes a more rapid motion of the front.

Figure 15 shows the time evolution of dissociation front for different hydrate zone permeabilities for a natural gas output of 0.04kg/s. Here, the reservoir pressure and temperature are, respectively, 15MPa and 287K. This figure shows that the dissociation front moves faster as the hydrate zone permeability decreases. As noted before, this is because at smaller hydrate zone permeability, the natural gas flow toward the front decreases. To

maintain a fixed flow rate, a large amount of hydrate has to dissociate to compensate, and therefore, the dissociation front moves faster.

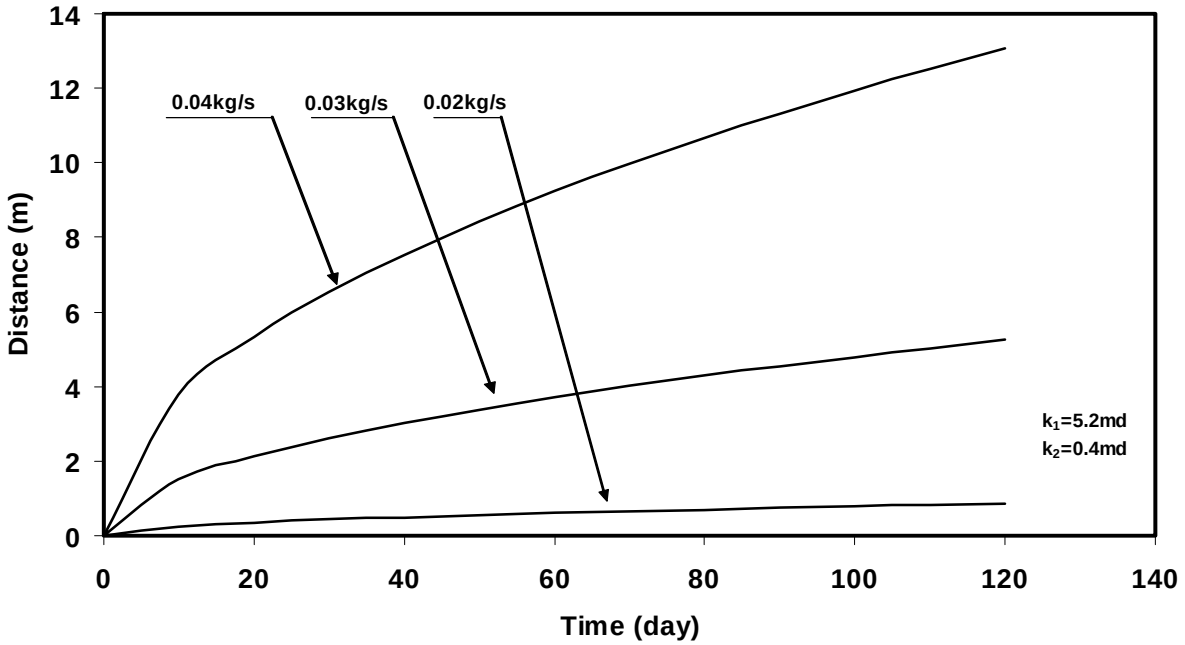

Figure 13. Time variations of the position of the dissociation front for different natural gas outputs.

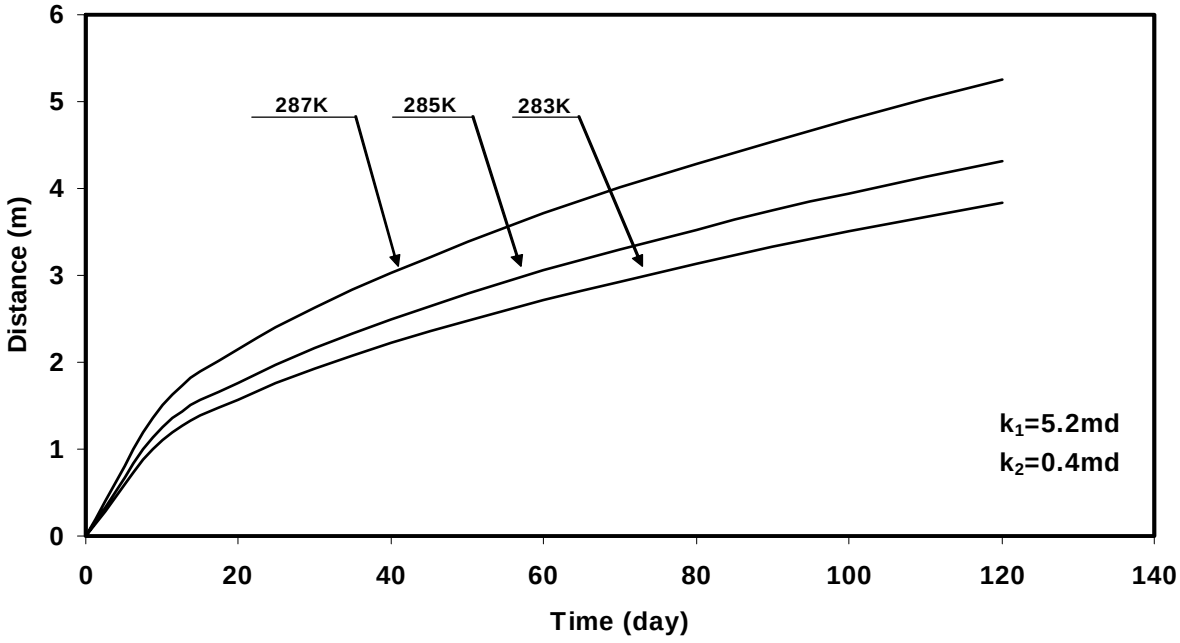

Figure 14. Time variations of the position of the dissociation front for different reservoir temperature for a well natural gas output of 0.03 kg/s.

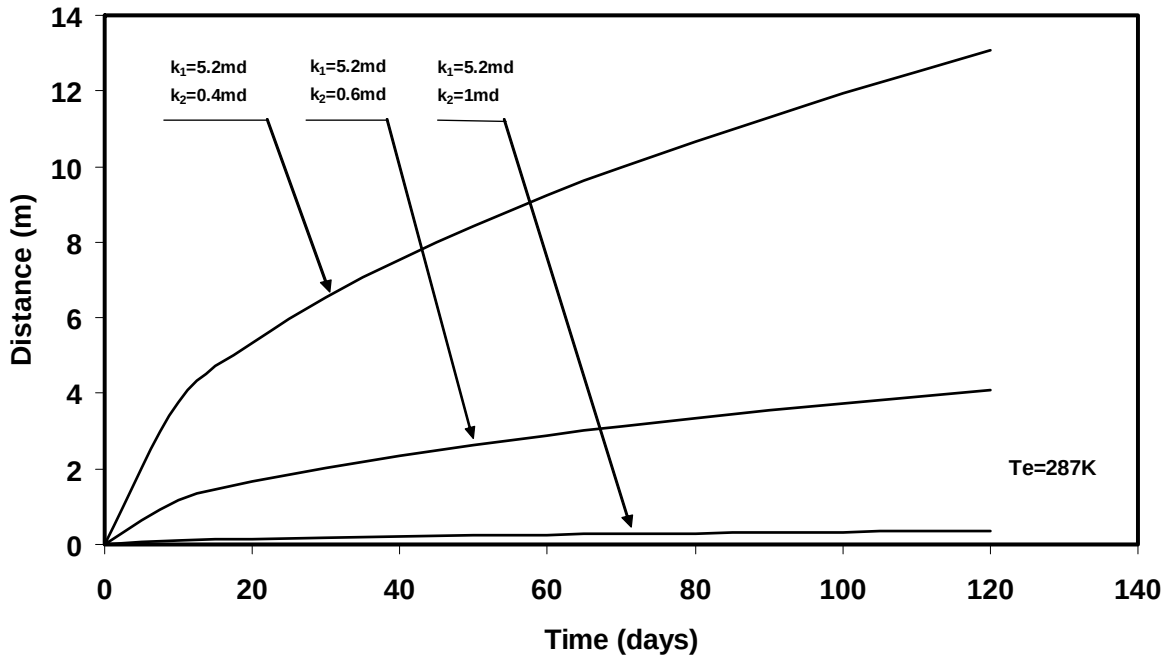

Figure 15. Time variations of the position of the dissociation front for a well natural gas output of 0.04 kg/s and for different permeabilities.

Conclusions of the Linearized Dissociation Model

Dissociation of methane hydrate in confined, pressurized reservoirs for fixed well outputs is studied. Evolutions of pressure, temperature, mass flux and mass flow rate profiles in axisymmetric reservoirs under various conditions are analyzed. The effects of variation in well output, reservoir temperature and reservoir zone permeabilities are studied. On the basis of the results presented, the following conclusions may be drawn:

i. Under favorable conditions natural gas can be produced at a fixed rate from hydrate reservoirs by a depressurization well.

ii. For a large homogenous hydrate reservoir containing free natural gas, the dissociation pressure and temperature are fixed, and depend only on the reservoir conditions and the well output.

iii. For fixed reservoir pressure and temperature, and a constant well production rate, the well pressure decreases with time. Thus, to maintain a constant natural gas output, the well pressure needs to be continuously reduced.

iv. At low well output, the decrease in the well pressure is very slight. At high well outputs, the well pressure decreases rather quickly and constant output can only be maintained for a short period of the time.

v. The reservoir permeability in the hydrate zone significantly affects the natural gas production process.

vi. For a fixed natural gas output, the pressure and temperature profiles have a smooth variation in the hydrate zone, but have sharper slope in the gas zone.

vii. The gas mass flow rates in the hydrate and in the gas zone are roughly constant, with a sharp jump at the dissociation front.

As noted before, the presented linearization approach neglects the heat conduction in the reservoir and cannot enforce the balance of energy at the dissociation front. When this limitation is removed, the similarity solutions do not hold and the original nonlinear governing equations must be solved numerically. Such a study is also performed and the results are presented in the next section.

2. NUMERICAL SOLUTION FOR NATURAL GAS PRODUCTION FROM METHANE HYDRATE DISSOCIATION

This paper describes a one-dimensional model for natural gas production from the dissociation of methane hydrate in a confined reservoir by a depressurizing well. The approach accounts for the heat released by hydrate dissociation and convection-conduction heat transfer in the gas and hydrate zone. The system of governing equations is solved using a finite difference scheme. For different well pressures and reservoir temperatures, the gas flow, the pressure and temperatures conditions in the reservoir are simulated. Distributions of temperature and pressure in the hydrate and gas regions and time evolutions of natural gas output also are evaluated. It is shown that the gas production rate is a sensitive function of well pressure. In addition, both heat conduction and convection in the hydrate zone is important. The simulation results are compared with the linearization approach and the shortcomings of the earlier approach is discussed.

Hydrate Dissociation Model

Assume that there is a methane hydrate reservoir with pressure P_e and temperature T_e containing stable solid hydrate and free methane gas. When a well is drilled into the reservoir, the pressure in the drilled area drops to the well pressure P_G. For sufficiently low pressure P_G below the pressure-temperature equilibrium condition, the hydrate in the neighborhood of the well dissociates. The process of hydrate dissociation is assumed to be analogous to ice melting, which occurs at a front instead of the entire volume. The so-called dissociation front separates the reservoir into two zones. The gas zone forms near the well, where only natural gas and water exist. The hydrate zone is further away from the well, where the solid hydrate and natural gas exist. Natural gas can then be recovered from the well, while the dissociation front moves outward into the reservoir with time.

In the present study it is assumed that the pressure and temperature at the dissociation front are respectively the equilibrium pressure, P_D, and temperature, T_D, which vary slowly with time. Water flow in the reservoir and the Joule-Thomson cooling effect are, however, neglected.

Mathematical Model

Consider a section of Fig. 1 as the one-dimensional model used in the computation. In this figure, the location of well is at x=0, where the well pressure is fixed at P_G. A length of L=100 m of the hydrate reservoir is modeled in the present analysis. At x=L, it is assumed that the reservoir pressure and temperature are, respectively, fixed at Pe and Te. In this figure the dissociation front, which is located at X(t), separates the reservoir into two zones. The

region 0<x<X(t) is referred to as the gas zone, and the area X(t)<x<L is the hydrate zone. The dissociation front X(t) moves outward as the gas production from the well continues.

In the subsequent analysis, subscript n identifies the region, with n=1 or 2 corresponding to the gas zone or the hydrate zone, respectively. Pressure distribution in the reservoir is governed by

$$\frac{\partial P_n}{\partial t} = a_n \frac{\partial^2 P_n^2}{\partial x^2} \tag{2-1}$$

where

$$a_n = \frac{k_n}{\Phi_n \mu} \tag{2-2}$$

and

$$\Phi_1 = (1- \alpha) \Phi \tag{2-3}$$

$$\Phi_2 = (1 - \beta) \Phi \tag{2-4}$$

Here P_n and k_n are the pressure and the gas permeability, respectively, μ is the gas viscosity, α is the water saturation, β is the hydrate saturation, Φ is the porosity, Φ_1 is the content of free gas in the gas zone, and Φ_2 is the content of free gas in the hydrate zone.

The velocity of natural gas ν_n in the gas and the hydrate zones is given by Darcy's law. i.e.,

$$\nu_n = -\frac{k_n}{\mu} \frac{\partial P_n}{\partial x} \tag{2-5}$$

Assuming that the time variation of gas density is small, the heat transfer equation in the gas and hydrate zone is given as

$$\frac{\partial T_n}{\partial t} + \nu_n \frac{\partial T_n}{\partial x} = \alpha_n \frac{\partial^2 T_n}{\partial x^2} \tag{2-6}$$

where T_n is the temperature, and α_n is the heat diffusivity in the gas and hydrate zone

In general, the equilibrium temperature and pressure at the dissociation front are functions of time. The phase equilibrium relation between temperature T_D and pressure P_D at the dissociation front is given as (Makogon, 1997)

$$\log_{10} P_D = a\,(T_D - T_0) + b\,(T_D - T_0)^2 + c \tag{2-7}$$

where T_0 is 273.15K and a,b,c are empirical constants that depend on the hydrate composition. Values of a, b, and c are obtained from the equilibrium pressure-temperature data of methane hydrate. Using a least square fit, it follows that (Ji et al. 2001)

$$a = 0.0342\ K^{-1},\ b = 0.0005\ K^{-2},\ c = 6.4804$$

where in Equation (2-7) P_D is in Pa.

The process of hydrate dissociation at the dissociation front is an endothermic phase-change process. The dissociation heat for per kilogram of hydrate in J/kg is given as (Kamath, 1983)

$$\Delta H = AT_D + B \tag{2-8}$$

where T_D is the dissociation temperature, and A, B are constants given by

$$A=-1050\ J/kg,\quad B=3527000\ J/(kgK)$$

The initial and boundary conditions are given as

$$P_1(0,t) = P_G \tag{2-9}$$
$$P_1(X(t),t) = P_2(X(t),t) = P_D\ (t) \tag{2-10}$$
$$T_1(X(t),t) = T_2(X(t),t) = T_D\ (t) \tag{2-11}$$
$$P_2(L,t) = P_2(x,0) = P_e \tag{2-12}$$
$$T_2(L,t) = T_2(x,0) = T_e \tag{2-13}$$

Energy balance at the dissociation front is given by

$$v_1(X,t)\rho_1(X,t)C_P T_1(X,t) - v_2(X,t)\rho_2(X,t)C_P T_2(X,t) - K_1 \frac{\partial T_1}{\partial x}\Big|_{x=X} + K_2 \frac{\partial T_2}{\partial x}\Big|_{x=X} = \Delta H \dot{m}_h \tag{2-14}$$

where K_n is the heat conductivity in the gas and hydrate zone, ρ_n is the density of natural gas in zone 1 or 2, $\dot{m}_h$ is the hydrate dissociation rate per unit area, and C_p is the heat capacity of natural gas. In Equation (2-14), the first term on the left hand side is the convective heat flux out of the dissociation front into the gas zone; the second term is the convective heat flux from the hydrate zone into the dissociation front. The third term is conductive heat flux from the dissociation front to gas zone. The fourth term is the conductive heat flux from hydrate

zone into the dissociation front. The term on the right hand side is the rate of heat supplied for hydrate dissociation per unit time per unit area.

The densities of the natural gas in the gas and hydrate zone at the dissociation front are the same and are given as

$$\rho_1(X,t) = \rho_2(X,t) = \rho_0 \frac{P_D T_0}{z P_0 T_D} \tag{2-15}$$

where z is the gas compressibility, and ρ_0 is the gas density at atmospheric pressure P_0 and temperature T_0.

The mass rate of hydrate dissociation is given by

$$\dot{m}_h = \rho_3 \Phi \ \beta \frac{dX}{dt} \tag{2-16}$$

where ρ_3 is hydrate density, $\frac{dX}{dt}$ is the speed of the dissociation front movement, and, as noted before β is hydrate saturation.

Substituting Equations (2-15) and (2-16) into Equation (2-14), it follows that

$$v_1(X,t) - v_2(X,t) - \frac{z P_0 K_1}{C_P \rho_0 P_D T_0} \frac{\partial T_1}{\partial x}\Big|_{x=X} + \frac{z P_0 K_2}{C_P \rho_0 P_D T_0} \frac{\partial T_2}{\partial x}\Big|_{x=X} = \Delta H \frac{z \rho_3 P_0 \Phi \beta}{C_P \rho_0 P_D T_0} \frac{dX}{dt} \tag{2-17}$$

The mass balance at the dissociation front is given as

$$\rho_1 v_1(X,t) - \rho_2 v_2(X,t) = -[\beta \varepsilon \rho_3 - (1-\alpha)\rho_1]\Phi \frac{dX}{dt} \tag{2-18}$$

where ε is the mass fraction of gas in methane hydrate.

Using Equation (2-15), Equation (2-18) may be restated as

$$v_1(X,t) - v_2(X,t) = -[\varepsilon\beta \frac{\rho_3 P_0 T_D}{\rho_0 P_D T_0} z - (1-\alpha)]\Phi \frac{dX}{dt} \tag{2-19}$$

Equations (2-7), (2-8), (2-17) and (2-19) describe the mass and energy balance at the dissociation front.

Numerical Method of Solution

In the numerical simulation, initially the length of reservoir is 100 m, which is divided into 500 grids. That is, a grid spacing of 0.2m is used. To start the computation, it is assumed that the dissociation front is formed with a 1m-long gas zone. The temperature and pressure profiles in the gas zone at the initial time are assumed to be linear.

Equations (2-1) and (2-6) are four coupled equations governing the temperature and pressure variations in the reservoir. These equations are nondimensionalized and solved with a finite difference method as described in Appendix A. An explicit central difference method is used to solve the pressure Equation (2-1) and an upwind explicit method is used to solve heat transfer Equation (2-6) in the gas zone. To solve the conduction-convection heat transfer Equation (2-6) in the hydrate zone, an implicit method is used.

The dissociation front X(t) is a moving boundary at the interface between the hydrate and the gas zones. At the initial time, T_D and P_D are unknown. The correct values of T_D and P_D must satisfy the balance of energy and mass given by Equations (2-17) and (2-19). A bisection method is used to obtain the correct P_D and T_D at the dissociation front. At the start, the values of P_D and T_D, are assumed; Equations (2-1) and (2-6) are then solved iteratively for 20 hours, which is the estimated time for forming a 1m-long gas zone. The velocity of dissociation front motion, $\frac{dX}{dt}$, is then evaluated from both Equations (2-17) and (2-19). The initially assumed values for P_D, T_D are adjusted until the values of $\frac{dX}{dt}$ obtained from Equations (2-17) and (2-19) are the same within a specified tolerance.

In the computation, values of $\frac{dX}{dt}$ are evaluated from Equations (2-17) and (2-19) at every time step and are compared. The bisection method is then used to adjust $T_{D(t)}$ and $P_{D(t)}$ until the values of $\frac{dX}{dt}$ become the same (with the specified tolerance). Since the dissociation temperature T_D and pressure P_D are slowly varying functions of time, only a few iterations are needed to find a converge solution for the velocity of dissociation front.

At each time step, the dissociation front moves outward a small step $\Delta X(t)$. In the computation, the front is kept at the same grid until the accumulated motion of the front reaches one-grid length (0.2 m). Then the front is moved by one grid in the computational domain. To simulate an unbound reservoir, the length of the computational domain of the hydrate zone is kept fixed. As the dissociation front moves outward the outer boundary of the

hydrate reservoir also is moved by the same distance. That is, at the step that the dissociation front moves one grid, the gas zone becomes one grid longer and hydrate zone has the same length. The new dissociation temperature and pressure are then obtained by the bisection method, and the computation scheme continues.

Results

This section presents the numerical solution results for time evolutions of pressure and temperature profiles in the hydrate reservoir under various conditions. In addition, time variations of methane gas production, and location of the dissociation front also are evaluated..

For a reservoir temperature of 287 K, and a reservoir pressure of 15 MPa, Fig. 16 shows variations of pressure and temperature profiles at different times. Here the permeability in hydrate and gas zones are, respectively, 0.6 md and 2.4 md. As noted before, the hydrate reservoir is divided into two zones by the dissociation front, and the temperature variations in the two zones are quite different. Fig. 16a shows that in hydrate zone the temperature decreases gradually from the reservoir temperature far from the front to the dissociation temperature at the front. In the region near the dissociation front, the gradient of temperature variation becomes sharp, indicating a sharp increase in the heat conduction to the front. In the gas zone, temperature decreases gradually from the dissociation temperature at the dissociation front to its minimum value at the well. For different times, the temperature profiles in the gas region from well to the dissociation front remains roughly the same. Fig. 16a also shows that as the dissociation front moves outward, the temperature at the dissociation front, $T_{D,}$ increases slightly with time. The time dependence of dissociation temperature observed here is in contrast to the result obtained from the linearization method suggested by Makogon (Ji et al., 2001), which leads to constant T_D.

The corresponding pressure profiles for different times under the same conditions for the far field and the near field are presented in Fig. 16b. The pressure decreases gradually from the reservoir pressure to the dissociation pressure at the dissociation front, and then decreases to its minimum value at the well. For the present case where the permeability of the gas zone is four times that of the hydrate zone, there is a sharp change in the slope of the pressure profile at the dissociation front as can be seen in Fig. 16b. This figure shows that the pressure profile in the gas region from well to the dissociation front remains unchanged.

For a reservoir pressure of 15 MPa, time evolutions of the gas mass flux (kg/m^2s) across the reservoir are displayed in Fig. 16c. In the gas zone, the gas mass flux is nearly fixed, while in the hydrate zone, the gas mass flux increases towards the dissociation front. Fig. 16c shows that there is a jump in the mass flux due to the hydrate dissociation, which moves outward with time as the dissociation front penetrates deeper into the hydrate

reservoir. The gas mass flux in the reservoir and the amount of natural gas generated due to hydrate dissociation decrease with time.

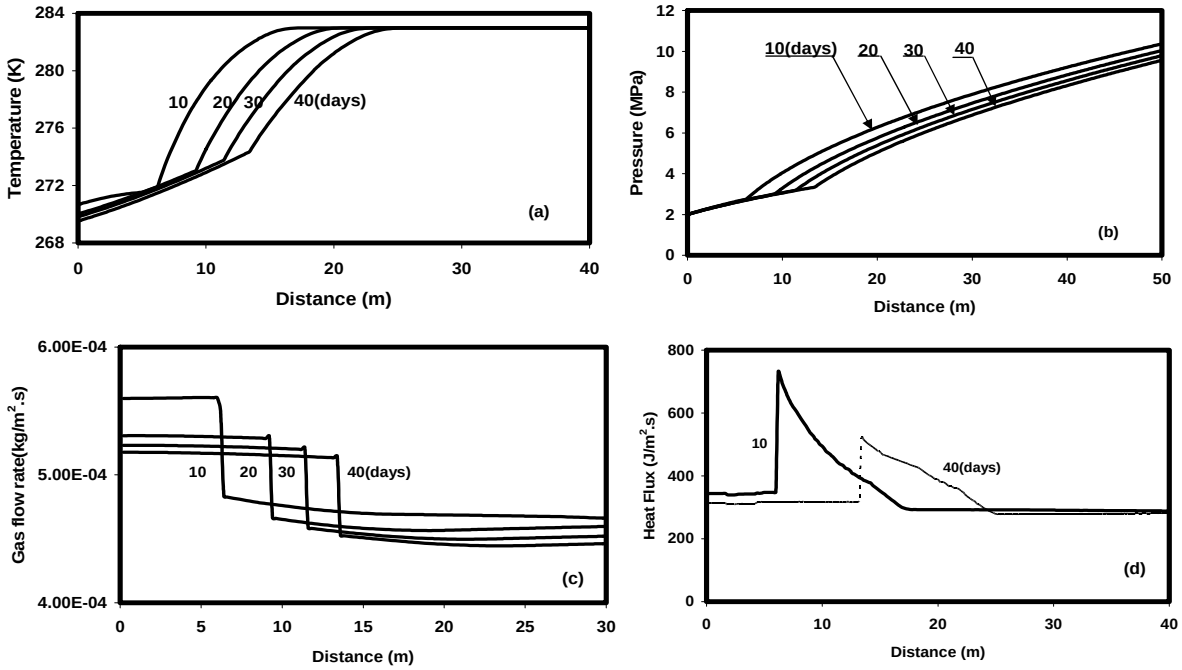

Figure 16. Time variations of temperature, pressure, mass and heat flux profiles in a reservoir for a well pressure of 2MPa and a reservoir temperature of 287K.

To provide an understanding of the nature of the heat transfer during hydrate dissociation, the heat flux profiles throughout the reservoir are shown in Fig. 16d. In this figure, the conductive and the convective heat fluxes are displayed separately at different times. Here solid lines show the profiles at 10 days, while the 40-day profiles are shown by dashed lines. In the hydrate zone, the conductive heat flux is very small in the region far away from the dissociation front, but increases sharply in the region near the dissociation front due to the large temperature gradient. In the gas zone, the conductive heat is negligibly small. The convective heat flux in both hydrate and gas zones are roughly constant. There is a jump of convective heat flux at the dissociation front, which indicates that the convective heat flow out of the dissociation front is always larger than the convective heat flow into the dissociation front. This is due to the added mass of gas that is generated at the dissociation front. Fig. 16d also shows that both convective heat flux and conductive heat flux decrease with time.

Comparisons of temperature, pressure and gas flow profiles as predicted by the present numerical method with the linearization method suggested by Makogon (Ji et al. 2001) are presented in Fig. 17. Here a reservoir temperature of 287 K, a reservoir pressure of 15 MPa and a well pressure of 2 MPa are used and all other parameters are kept identical. In these figures, the solid lines show the numerical simulation results, while the dashed lines show those of the linearized method. From Fig. 17a, it is seen that both temperature profiles reach the same boundary conditions far from the front, however, near the dissociation front, the temperature profiles of the numerical method have much sharper gradient when compared with that of the linearization method. The reason is that in linearization method suggested by Makogon, the heat conduction was ignored.

To solve a conductive-convective heat transfer equation, two boundary conditions are needed. For solving Equation (2-6), one boundary condition is given by Equation (2-13), and the other is given by Equation (2-11). The unknown dissociation temperature $T_{D,}$ is obtained from the energy balance at the dissociation front given by Equation (2-17). The linearization model suggested by Makogon (Ji et al., 2001), which neglects the heat conduction effects, requires only one boundary condition, which is given by Equation (2-13). Thus, the energy balance at the dissociation front could not be included in the linearization model, which is a severe limitation of the linearization approach. In the absence of heat conduction, the temperature gradient in hydrate zone near the dissociation front becomes small.

To show the role of various heat fluxes at the dissociation front, time variations of conductive heat flux into the dissociation front, convective heat fluxes in and out of dissociation front are shown in Fig. 17b. It is clear that the convective heat flux into the dissociation front is roughly equal to the convective heat flux out of the front. This means that the conductive heat flux plays the dominant role in supplying the heat for hydrate dissociation. Fig. 17b implies that without the heat conduction, the energy balance at the dissociation front cannot be satisfied.

Fig. 17c compares the numerically predicted pressure profiles with those obtained by the linearization method. While the trends of the pressure profiles are comparable, there are quantitative differences. In the hydrate zone, the pressure as predicted by the linearization method is somewhat lower than that of the numerical method. In the linearization method, Equation (2-1) is linearized with reservoir pressure P_e in the hydrate zone or well pressure P_G in the gas zone. Because the dissociation pressure P_D is close to P_G, the linearization does not alter the pressure profiles in the gas zone. While in the hydrate zone, the large difference between P_D and Pe leads to noticeable differences in the computed pressures by the two methods. Fig. 17c implies that the linearization method leads to pressure profiles that are qualitatively comparable to those obtained by the numerical method, with amount of error being larger in the hydrate zone.

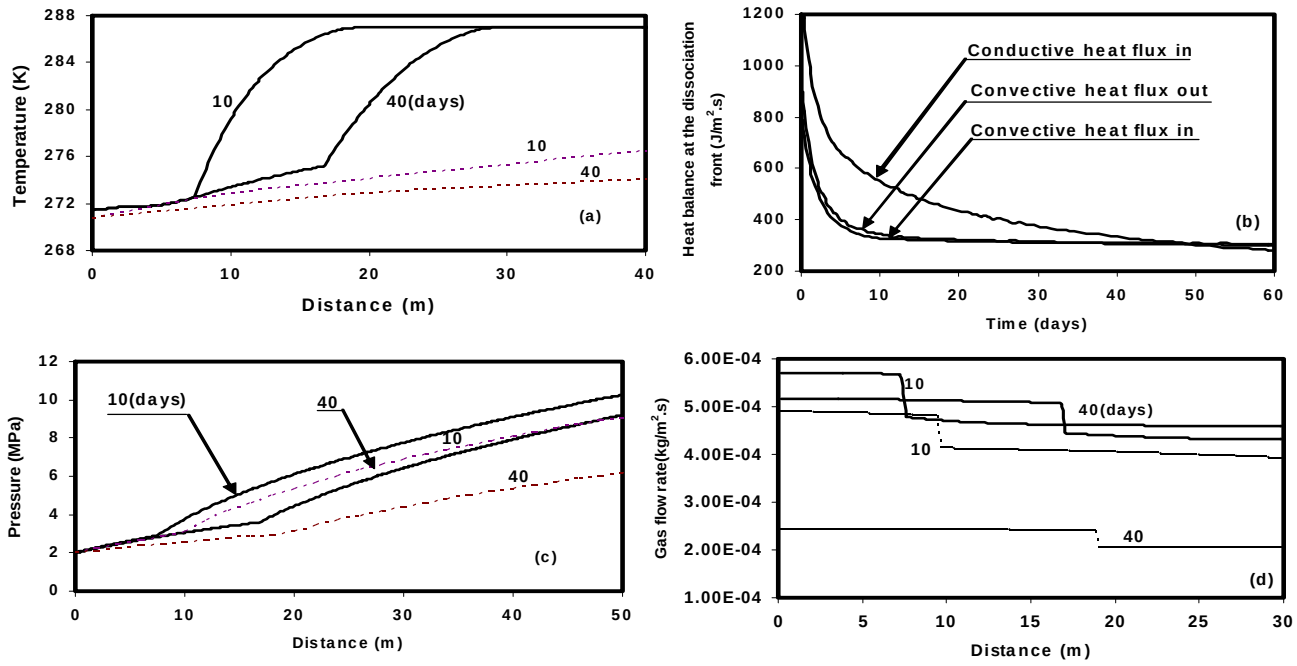

Figure 17. Comparison of the present temperature and pressure profiles and mass flow rate with linearized solutions for a reservoir temperature of 287K and a well pressure of 2MPa. Solid lines: numerical solutions. Dashed lines: linearized solutions suggested by Makogon (Ji et al., 2001).

Comparison of the mass flux ($\rho\upsilon$) profiles of the numerical and the linearization methods is shown in Fig. 17d. For both methods, the predicted trends of mass flux profiles throughout the reservoir are similar; however, mass flux of the linearization method is lower than that of the numerical method. The reason is that the velocity, as given by Darcy's law, is proportional to the pressure gradient, and density is proportional to the ratio of pressure over temperature. At a fixed time, Fig. 17 shows that the temperature and pressure of the numerical method are higher than that of the linearization method. Furthermore, pressure gradient in the hydrate zone is much larger than that of linearization method. The combined effects of a larger pressure gradient and a higher temperature and pressure of the numerical method lead to a higher mass flux throughout the reservoir.

For a well pressure of 1MPa and reservoir temperature of 287K, Fig. 18a presents temperature profiles at different times. Similar to Fig. 18a, the dissociation front divides the reservoir into the gas and the hydrate zones. The gradients of temperature in two zones are different. In the gas zone, the temperature decreases gradually from the dissociation temperature at the front to the temperature at the well. In the hydrate zone, the temperature decreases gradually from the reservoir temperature far from the dissociation front and sharply decreases to dissociation temperature in the region near the dissociation front. Fig. 18a also

shows that the temperature in the gas zone varies slightly with time. Compared with Fig. 18a, the dissociation temperature at the dissociation front is lower and the dissociation front moves faster due to a lower well pressure. The corresponding pressure profiles are shown in Fig. 18b. Except for the lower dissociation pressures and the faster movement of the dissociation front, these profiles are quite similar to those shown in Figure 16b.

Fig. 18c shows the time evolutions of the gas mass flux (kg/m^2s) across the reservoir. In the gas zone, mass flux is roughly fixed, while in the hydrate zone, it increases towards the dissociation front. There is a jump in the mass flux at the dissociation front due to the hydrate dissociation. Comparing Figs. 18 and 16, shows that in the gas zone, the mass flux at lower well pressure is higher. In the hydrate zone, however, the mass fluxes in both figures are nearly the same. The jump of mass flux in Fig. 18c is larger than that in Fig. 16c, which indicates that under the same conditions, a lower well pressure leads to a higher rate of hydrate dissociation.

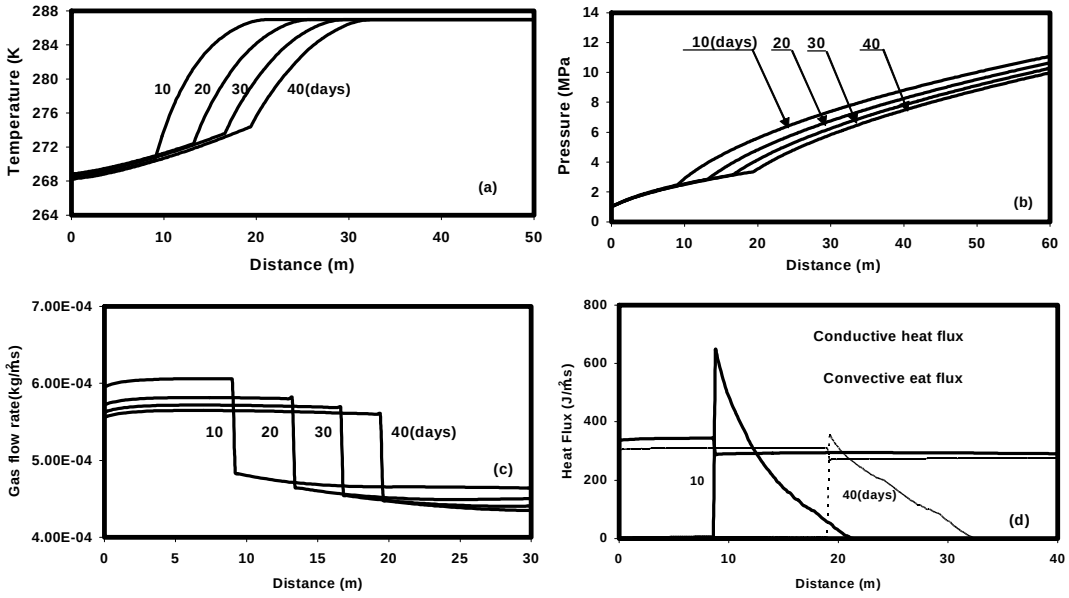

Figure 18. Time variations of temperature, pressure, mass and heat flux profiles in a reservoir for a well pressure of 1MPa and a reservoir temperature of 287K.

Fig. 18d presents the heat flux profiles throughout the reservoir. Here the conductive heat flux and convective heat flux are also shown separately at different times. The trends of heat flux profiles in Fig. 18d are similar to those shown in Fig. 16d. The conductive heat flux varies sharply in the region near the dissociation front and is higher than that shown in Fig. 16d. Fig. 18d shows that the convective heat flux, in the gas zone is slightly higher than that of Fig. 16d, while in the hydrate zone, they are nearly identical.

For a reservoir with a temperature of 285K and a well pressure of 2MPa, the temperature, pressure, mass and heat flux profiles are shown in Fig. 19. The gas permeabilities in the gas zone and the hydrate zone are kept fixed at 2.4 md and 0.6 md. Fig. 19a shows that the temperature profiles have trends similar to those shown in Fig. 16a. The only difference is that temperature in the gas zone noticeably decreases with time. Similarly, the pressure profiles shown in Fig. 19b are nearly the same as those shown in Fig. 16b. The dissociation front, however, moves slower in Fig. 19. Fig. 19c displays the mass flux profiles for the lower reservoir temperature. Comparing Figs. 19c and 16c, shows that the difference of mass flux profiles in two figures are very small. This indicates that the effect of small variation of reservoir temperature on the gas flux is rather small.

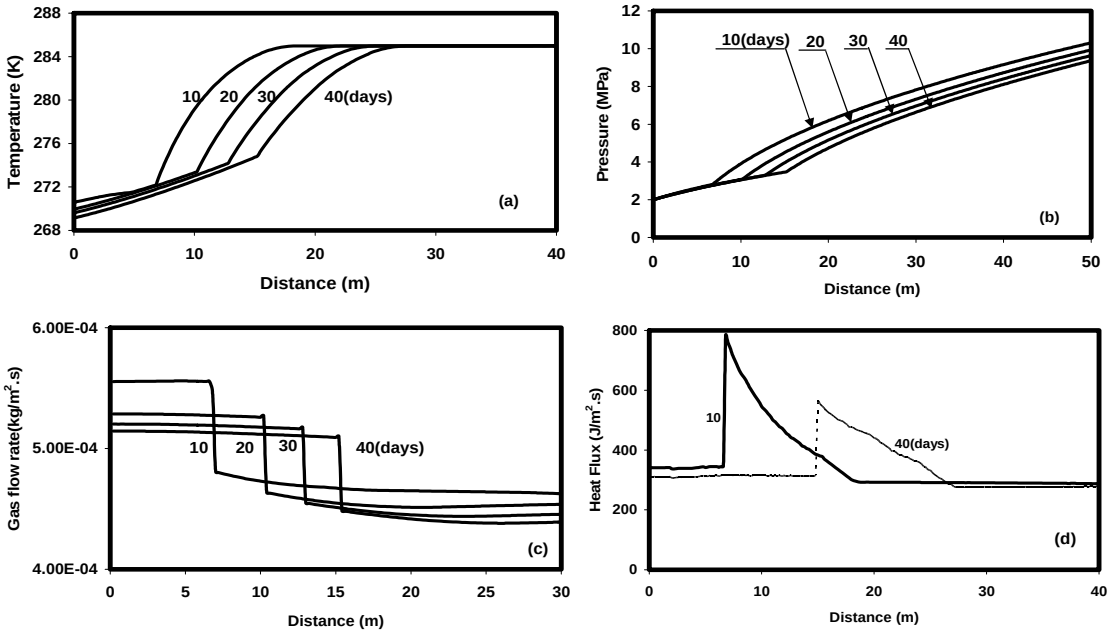

Figure 19. Time variations of temperature, pressure, mass and heat flux profiles in a reservoir for a well pressure of 2MPa and a reservoir temperature of 285K.

Fig. 19d shows the time variation of total heat flux (sum of the conductive and convective heat fluxes). In the gas zone, the heat flux is nearly the same. In the hydrate zone far from the dissociation front, the heat flux which is primarily convective heat flux is roughly constant or increases slightly toward the dissociation front. In the region near-front, as the temperature decreases sharply to the dissociation temperature at the front, the conductive heat flux becomes quite large and the total heat flux increases sharply to the maximum value at the dissociation front. There is a jump of heat flux at the dissociation front, which supplies the heat needed for hydrate dissociation. Fig. 19d also shows that the total heat flux decreases with time.

When the reservoir temperature is 283K and all other conditions are identical, the temperature, pressure, mass and heat flux profiles are presented in Fig. 20. Figs. 20a and 20b show that the temperature and pressure profiles are similar to those shown in Figs. 29a and 29b; except that the dissociation front moves slightly slower and the dissociation temperature and pressure are lower. The mass flux profiles shown in Fig. 6c are nearly the same as those shown in Fig. 29c, which again indicates that mass flux profile is not sensitive to small variation in the reservoir temperature. Fig. 20d shows the total heat flux at different times. Comparing Figs. 20d and 29d, shows that for a lower reservoir temperature, heat flux in the region near the dissociation front in the hydrate zone is smaller. This implies that reservoir temperature affects the temperature gradient in the region near the front.

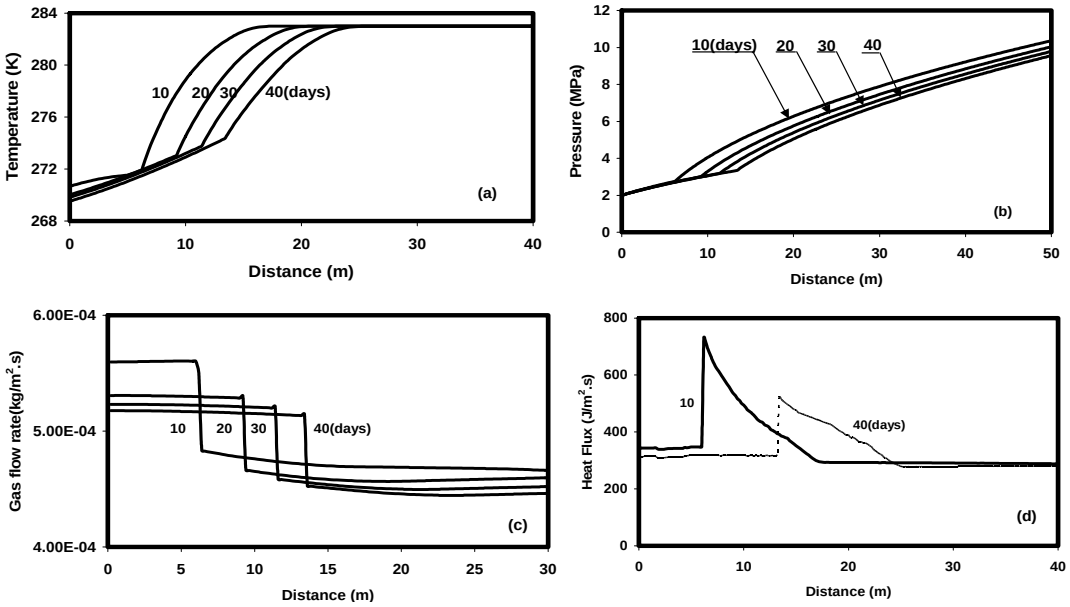

Figure 20. Time variations of temperature, pressure, mass and heat flux profiles in a reservoir for a well pressure of 2MPa and a reservoir temperature of 283K.

For numerical and linearization methods, time variations of movement of dissociation front, natural gas output and dissociation temperature for different well pressures are compared in Fig. 21. The reservoir conditions are assumed to be fixed at 15MPa and 287K. The gas permeabilities in the gas and the hydrate zones are, respectively, 2.4 md and 0.6 md. Numerical solutions are shown by solid lines, while the linearized solutions are shown by dashed lines. Fig. 21a shows the outward movement of the dissociation front with time. This figure indicates that as the well pressure decreases, the motion of the front speeds up. For a well pressure of 3MPa, the movement of the dissociation front as predicted by the linearization method is comparable to that of the numerical method. For the linearization method, however, the motion of the dissociation front is more sensitive to well pressure when compared with that of the numerical method. When the well pressure decreases to 1MPa, the

lineaerization method predicts that the dissociation front moves twice as fast, while the numerical method predicts only a 30% increase.

Time evolutions of the natural gas output are plotted in Fig. 21b. The natural gas output decreases with time, and also decreases as the well pressure increases. The natural gas output as predicted by the numerical method appears to level–off or decreases very slightly after the initial transient. For a fixed well pressure, the gas output as evaluated by the linearization method is lower than that of the numerical method and continues to decrease with time.

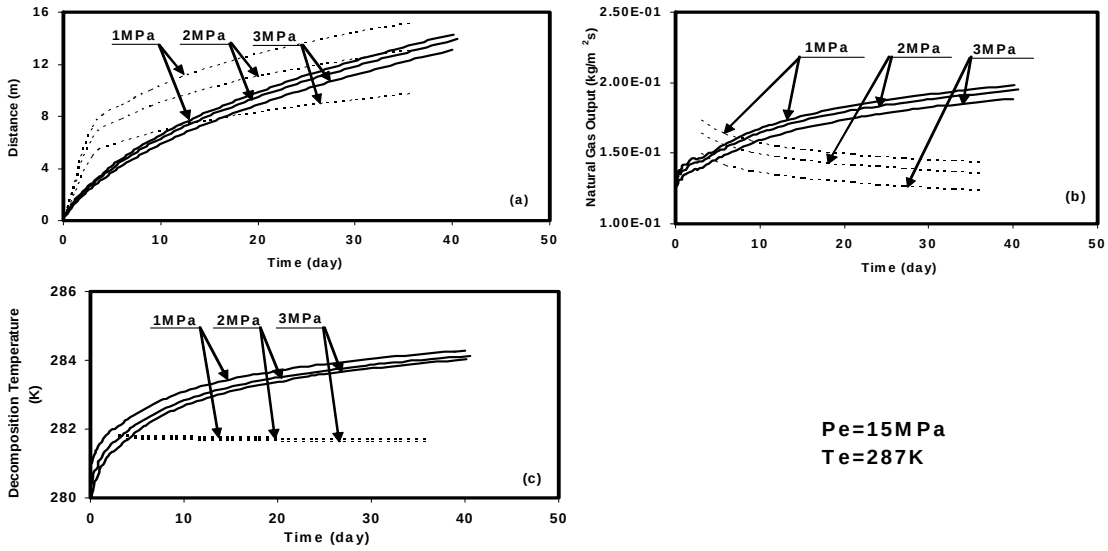

Figure 21. Comparison of present time variations of the position of dissociation for different well pressures. Solid lines: numerical solutions; Dashed lines: linearized solutions suggested by Makogon (Ji et al., 2001).

Fig. 21c shows time variations of the dissociation temperature for different well pressures. For a fixed well pressure, the dissociation temperature as predicted by the numerical method increases with time. The slight fluctuation of the dissociation temperature at the beginning is related to the assumed initial start up conditions in the reservoir. The dissociation temperature of the numerical method also varies with the well pressure, and increases as the well pressure increases. The linearization method, however, leads to the dissociation temperature that is independent of time (Makogon, 1997; Ji et al., 2001), and is not as sensitive to well pressure.

For different reservoir temperatures, Fig. 22 compares time variations of the movement of the dissociation front, natural gas output and the dissociation temperature as predicted by the numerical method with those of the linearization method. Here the reservoir and well pressures of 15MPa and 2MPa are assumed and the values of all other parameters

are kept the same as those used in Fig. 21. Fig. 22a shows the movement of the dissociation front. It is seen that the dissociation front moves faster when the reservoir temperature increases. The linearization method, however, predicts a sharp variation of the dissociation front motion when compared with the numerical method.

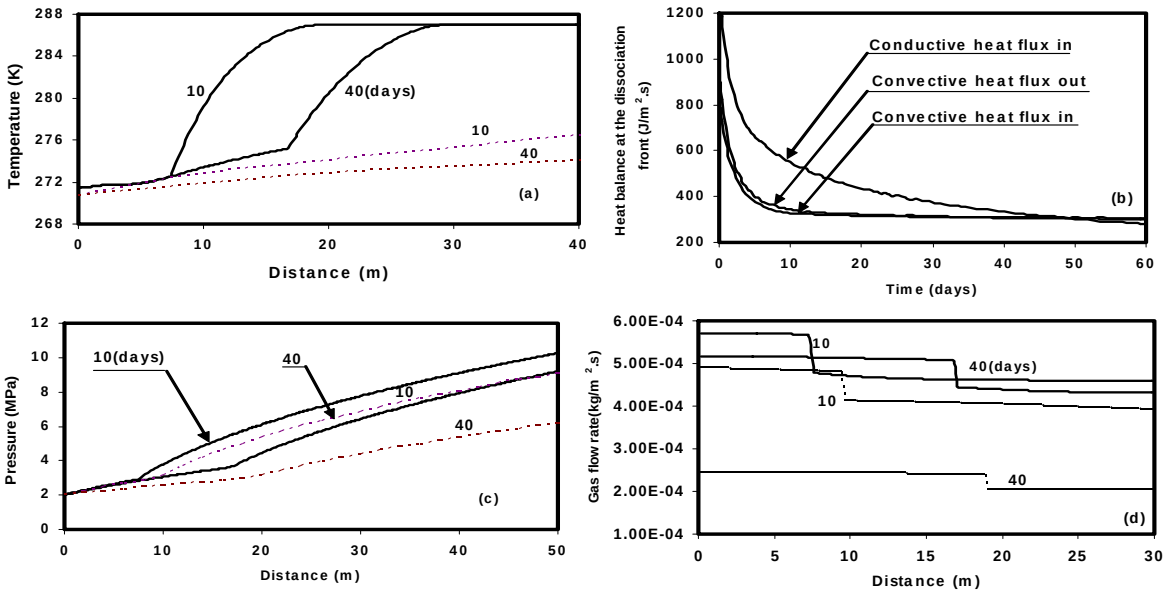

Figure 22. Comparison of the present time variations of the position of dissociation front, natural gas output and dissociation temperature with linearized solutions for different reservoir temperatures. Solid lines: numerical solutions; Dashed lines: linearized solutions suggested by Makogon (Ji et al., 2001).

In Fig. 22b time variations of the natural gas output for different reservoir temperatures are presented. The numerical method predicts that the natural gas output increases slightly with time and is not very sensitive to the reservoir temperature. The linearization solution, however, leads to a slightly decreasing trend. The reason is that the natural gas production depends on the pressure gradient near the well, which is not significantly affected by reservoir temperature. It also observed that the natural gas output predicted by the linearization method is smaller than that of the numerical method for a fixed reservoir temperature.

Fig. 22c shows time variations of the dissociation temperature with the reservoir temperature. The numerical method predicts that the dissociation temperature increases with time and the reservoir temperature. The linearization method, however, leads to a time-independent dissociation temperature that varies significantly with the reservoir temperature.

Summary

A one-dimensional model for natural gas production form hydrate dissociation by depressurization is presented. The equations governing the pressure and temperature fields in the reservoir, and balance of energy and mass flux at the dissociation front, are solved using a finite difference method. Time evolutions of temperature, pressure, gas mass flow and heat flux profiles across the reservoir, as well the movements of dissociation front and the natural gas output are evaluated. The results are compared with those of the linearized solutions suggested by Makogon (1997) and Ji et al. (2001). On the basis of the presented results, the following conclusions may be drawn:

1. The presented one-dimension model suggests that, under favorable hydrate reservoir conditions, depressurization (by drilling well) is a viable method producing natural gas from hydrate reservoirs.

2. For a fixed reservoir condition, well pressure controls the rate of natural gas output and the motion of the dissociation front. A lower well pressure leads to a higher natural gas output rate and a faster movement of the dissociation front.

3. Reservoir temperature affects the motion of dissociation front; however, the natural gas output is not sensitive to small variation in the reservoir temperature.

4. The dissociation temperature and pressure are slowly varying functions of time.

5. The dissociation temperature and pressure increase with the well pressure and the reservoir temperature.

6. Compared to the linearization method used in Makogon's model, the numerical method introduced in this paper provides a more accurate description for the process of hydrate dissociation.

7. The linearization method neglects the balance of energy at the dissociation front, which is included the presented numerical model.

8. The finite difference approach is advantageous in that it does not require linearization of the governing equations and also includes balance of energy at the dissociation front.

Due to the difficulty associated with the semi-analytical linearization model, its extension to multi-dimensions may not be meaningful, and should be critically evaluated.

3. NATURAL GAS PRODUCTION FROM HYDRATE DISSOCIATION: AN AXISYMMETRIC MODEL

The computation model of section 2 was extended and an axisymmetric model for natural gas production from the dissociation of methane hydrate in a confined reservoir by a depressurizing well was studied. During the hydrate dissociation, heat and mass transfer in the reservoir were analyzed. The system of governing equations was solved by a finite difference scheme. For different well pressures and reservoir temperatures, distributions of temperature and pressure in the reservoir, as well as the natural gas production from the well were evaluated. It was shown that the gas production rate was a sensitive function of well pressure. The simulation results were compared with the linearization approach and the shortcomings of the earlier approach was discussed. A manuscript was prepared that was tentatively accepted for publication in the Journal of Petroleum Science and Engineering.

4. MULTIDIMENSIONAL COMPUTATIONAL MODELING OF METHANE HYDRATE DISSOCIATION IN A SANDSTONE CORE

Hydrate dissociation in a porous sandstone core was studied using a computer modeling approach. It was assumed that the hydrate is dispersed the pores of the core. Using Fluent™ code, an axisymmetric model of the core was developed and solved for multiphase flows during the hydrate dissociation. The core model contained three separate phases, Methane hydrate, methane gas, and liquid water. At the start of simulation, the valve at one end of the core was opened exposing the core to low pressure; hydrate began to dissociate and methane gas and water began to flow. The depressurization was controlled by adjusting the pressure of the outlet valve.

A comprehensive Users' Defined Function (UDF) for analysis of hydrate dissociation process into the FLUENT code was developed. The new UDF used the kinetic model introduced by Kim et al. (1986), and can model multiple zones dissociation and multiphase flows. Variations of relative permeability of the core were included using Corey's model. The new model allows for variation of the porosity with hydrate saturation.

For different core temperatures and various outlet valve pressures, the spatial and temporal variations of temperature, pressure and flow fields in the core were simulated. The time evolutions of methane gas and water flow rate at the outlet were also evaluated. It is shown that the rate of hydrate dissociation in a core is a sensitive function of surrounding environment temperature, outlet pressure condition, and sample permeability.

Model Formulation

The governing equations used to solve for the multiphase flow conditions during the hydrate dissociation process are outlined in this section. The continuity equations for different species are given by

$$-\nabla\cdot\rho_k\mathbf{u}_k+\dot{m}_k=\frac{\partial}{\partial t}\left(\phi_o\rho_k S_k\right),\qquad (k=H,g,w),\qquad (4\text{-}1)$$

where $\dot{m}_k$ is the rate of generation/dissociation of species k, ϕ_o is the porosity of the core, S_k is the saturation of phase k, ρ_k is the phase density, t is time, and $\mathbf{u}_k$ is fluid velocity vector (with $\mathbf{u}_H=0$ since hydrate is stationary). Here H, g and w stands for hydrate, gas and water phases.

For saturations of various phases, the following equality holds

$$S_g + S_w + S_H = 1, \tag{4-2}$$

where $S_g, S_w,$ and S_H are, respectively, saturation of gas, water and hydrate phases. The effective porosity of the medium is given as,

$$\phi_{eff} = \phi_o(1 - S_H). \tag{4-3}$$

The Darcy's law for flow in porous media is given by

$$u_k = -\frac{K_D K_{rk}}{\mu_k}\nabla p, \qquad (k = g, w), \tag{4-4}$$

where K_{rk} is relative permeability of phase k and μ_k is the phase viscosity. Here, K_D is the absolute permeability of the media and is modeled as,

$$K_D = K_{Do}(1 - S_H)^N, \tag{4-5}$$

where K_{Do} is the absolute permeability at zero hydrate saturation, and N is the permeability reduction index which depends on the pore structure of the medium.

The relative permeability of water and gas are evaluated by Corey's (1954) formula given as,

$$K_{rw} = \bar{S}^4, \tag{4-6}$$

and

$$K_{rg} = (1 - \bar{S})^2(1 - \bar{S}^2), \tag{4-7}$$

where

$$\bar{S} = \frac{S_w - S_{wr}}{1 - S_{gr} - S_{wr}}. \tag{4-8}$$

In Equations (4-6) to (4-8), K_{rw} and K_{rg} are, respectively, the relative permeability of water and gas, and S_{wr} and S_{gr} are the irreducable saturations of water and gas.

The equation of energy balance for the effective medium may be written as

$$\frac{\partial}{\partial t}\left[(1-\phi o)\rho_R C_R T + \phi_o S_H \rho_H C_H T + \phi_o S_w \rho_w U_w + \phi_o S_g \rho_g U_g\right] = \nabla\cdot(K_o \nabla T) - \nabla\cdot\left(\rho_w h_w \mathbf{u}_{D,w} + \rho_g h_g \mathbf{u}_{D,g}\right) - \dot{Q}_H, \tag{4-9}$$

where T is the temperature, C is the heat capacity, U is the internal energy, and h is the enthalpy. Subscripts R, H, w and g, respectively, indicate rock, hydrate, water and gas. Here, K_o is the effective thermal conductivity and is defined as

$$K_o = (1-\phi_o)K_R + \phi_o(S_H K_H + S_g K_g + S_w K_w), \tag{4-10}$$

where $K_R, K_H, K_g,$ and K_w, are respectively, thermal conductivity of rock, hydrate, gas and water. In Equation (4-9), $\dot{Q}_H$ is heat-sink/source rate due to hydrate dissociation. The model for latent heat of dissociation is presented in the next section.

Hydrate Dissociation by Depressurization

As hydrate dissociates into gas and water, a dissociation front forms that divides the core into two regions, one containing solid hydrate, and the other containing dissociated gas and water. Kim et al. (1986) developed a model for the molar generation rate of methane gas due to hydrate dissociation, $\dot{n}_{gp}$. Accordingly,

$$\dot{n}_{gp} = k_B A_p [P_e(T) - P] \tag{4-11}$$

$$k_B = k_d^o \exp\left(-\frac{\Delta E}{RT}\right) \tag{4-12}$$

where A_p is the surface area of hydrate per unit volume, P_e is the equilibrium pressure, and P is the local pressure in the core. The dissociation rate constant, k_B, is given by Equation (4-12), where ΔE is the activation energy, R is the gas constant, and T is the temperature. The constant k_d^o is an intrinsic dissociation constant and is independent of pressure and temperature. In practice, these parameters are evaluated by curve fit to the experimental kinetic data. Values of ΔE=78151 J/kmol and k_d^o=124 kmol/Pa/s/m^2 were suggested by Kim et al. (1986) and Masuda et al. (1999).

The mass generation rate of gas and water per unit volume of the porous medium by hydrate dissociation are given by

$$\dot{m}_g = k_B M_g A_p \phi_o S_H [P_e(T) - P], \qquad P \le P_e \tag{4-13}$$

The heat of hydrate dissociation affects hydrate dissociation behavior because of changes in equilibrium pressure. Masuda et al. (1999) has suggested the following expression for the dissociation heat-sink rate,

$$\dot{Q}_H = \frac{-\dot{m}_H(c + dT)}{M_H}, \tag{4-14}$$

where c = 56,599 J/mol, d = -16.744 J/mol.K.

The relation between equilibrium temperature T_e and pressure P_e is given as (Makagon, 1997, Ji et al., 2001)

$$\log_{10}(P_e) = A\,(T - T_o) + B\,(T - T_o)^2 + C\ , \qquad (4\text{-}15)$$

where T_o is 273.15K and A, B, and C are empirical constants that depend on hydrate composition. Values of A, B, and C are obtained using the least squares error fit to the equilibrium pressure-temperature data for methane hydrate (Makogon, 1997, , Ji et al., 2001), i.e.,

$A = 0.0342\ K^{-1}$, $B = 0.0005\ K^{-2}$, $C = 6.4804$.

In Equation (4-18), P_e is in Pascal and T is in Kelvin.

Computational Grid

A computational mesh with 800 cells as shown in Figure 23 was used. The core is assumed porous with variable porosity. The local relative permeabilities of water and gas were also allowed to vary with time as hydrate dissociates. An ideal gas model for the gas phase was assumed and the Volume of Fluid (VOF) model was used for simulation of water and gas flows.

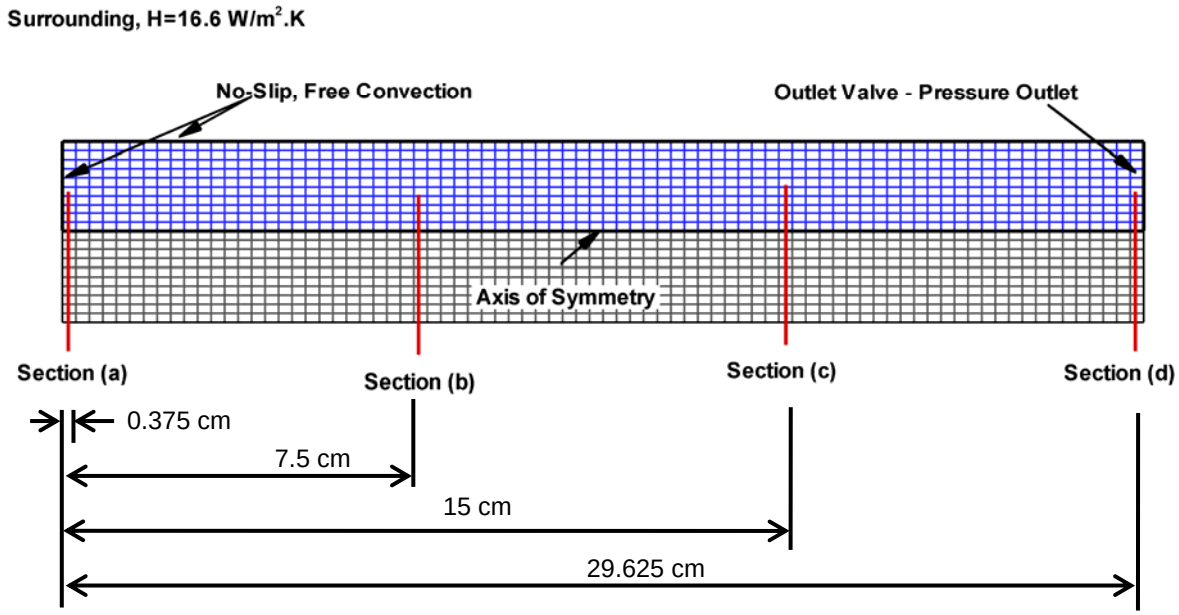

Figure 23. Schematic of hydrate core sample, the computational grid, locations of different sections, and the boundary conditions.

Simulation Results

Figure 24 shows the time evolution of the static pressure contours in the core sample at different times after the outlet valve opens. This figure shows that the pressure in the core gradually decreases from an initial value of 3.75 MPa to the outlet pressure of 2.84 MPa. Hydrate dissociation is initiated as soon as the pressure in the core sample becomes less than

the equilibrium pressure. Then the generated gas and water begin to move toward the outlet valve. The low-pressure front continues to move from the outlet valve into the core sample causing the hydrate to dissociate along the core. After 600 minutes, Figure 24d shows that the pressure in the core reaches to the surrounding pressure.

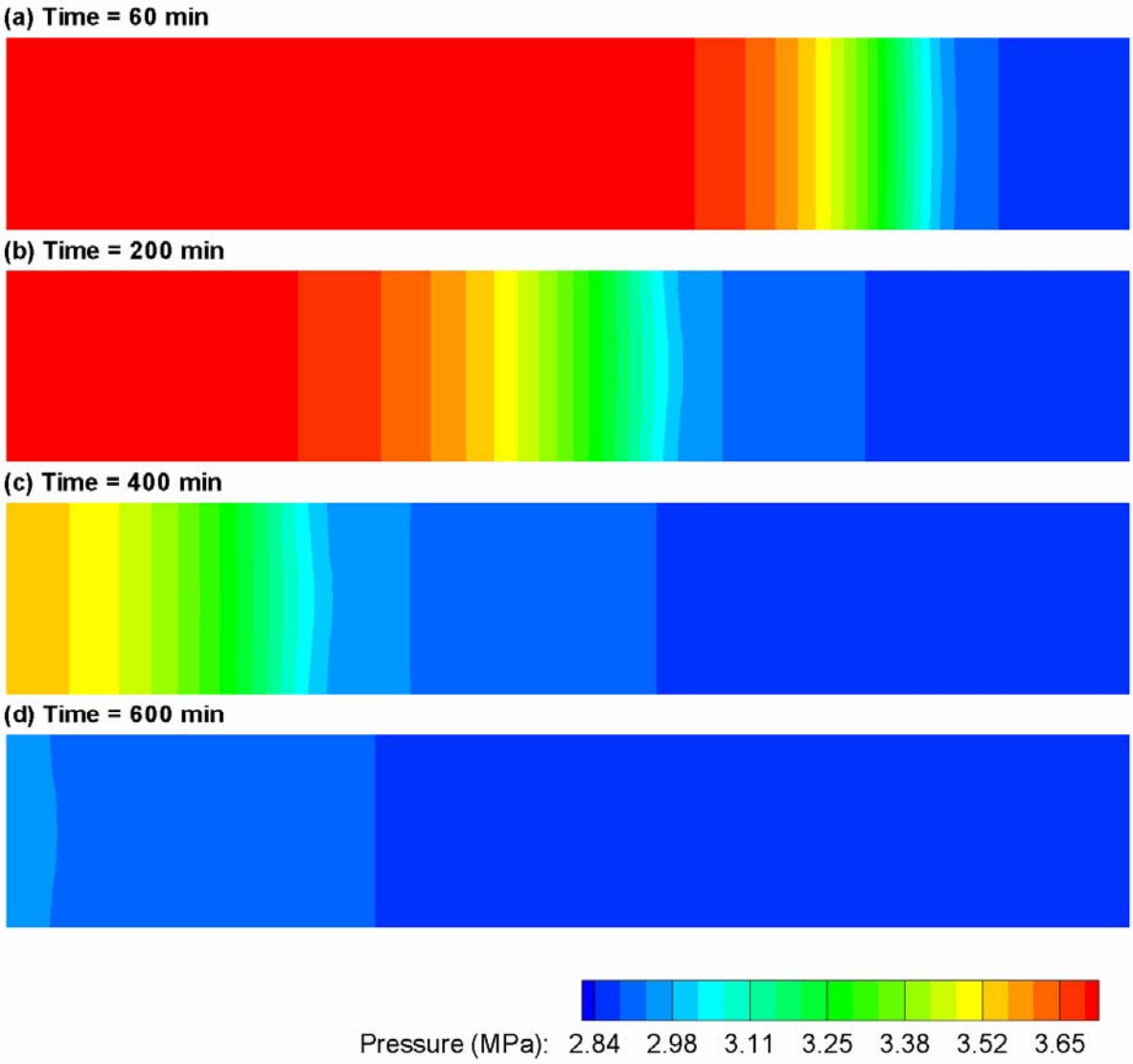

Figure 24. Sample pressure contours in the core sample at different times.

Figure 25 displays the contours of temperature in the core sample at four different times. The core sample is assumed to be in air with constant temperature. The temperature at the outlet valve is the same as the surrounding air temperature. Free convection heat transfer between the core walls and the surrounding is included in the model. As noted before, hydrate dissociation is an endothermic process, which results in absorption of heat. Figure 25 shows that as hydrate in the core sample dissociates, heat is absorbed from the

surrounding, which results in decreasing the local temperature in the core. The low temperature regions in Figure 25 represent the areas that hydrate is dissociating. As noted before, hydrate dissociation generates natural gas and liquid water that flow toward the outlet valve. Natural convection heat transfer increases the temperature of the core sample on the right hand side of the dissociation region (toward the outlet valve). Figure 25d shows that the core temperature approaches the surrounding air temperature with time.

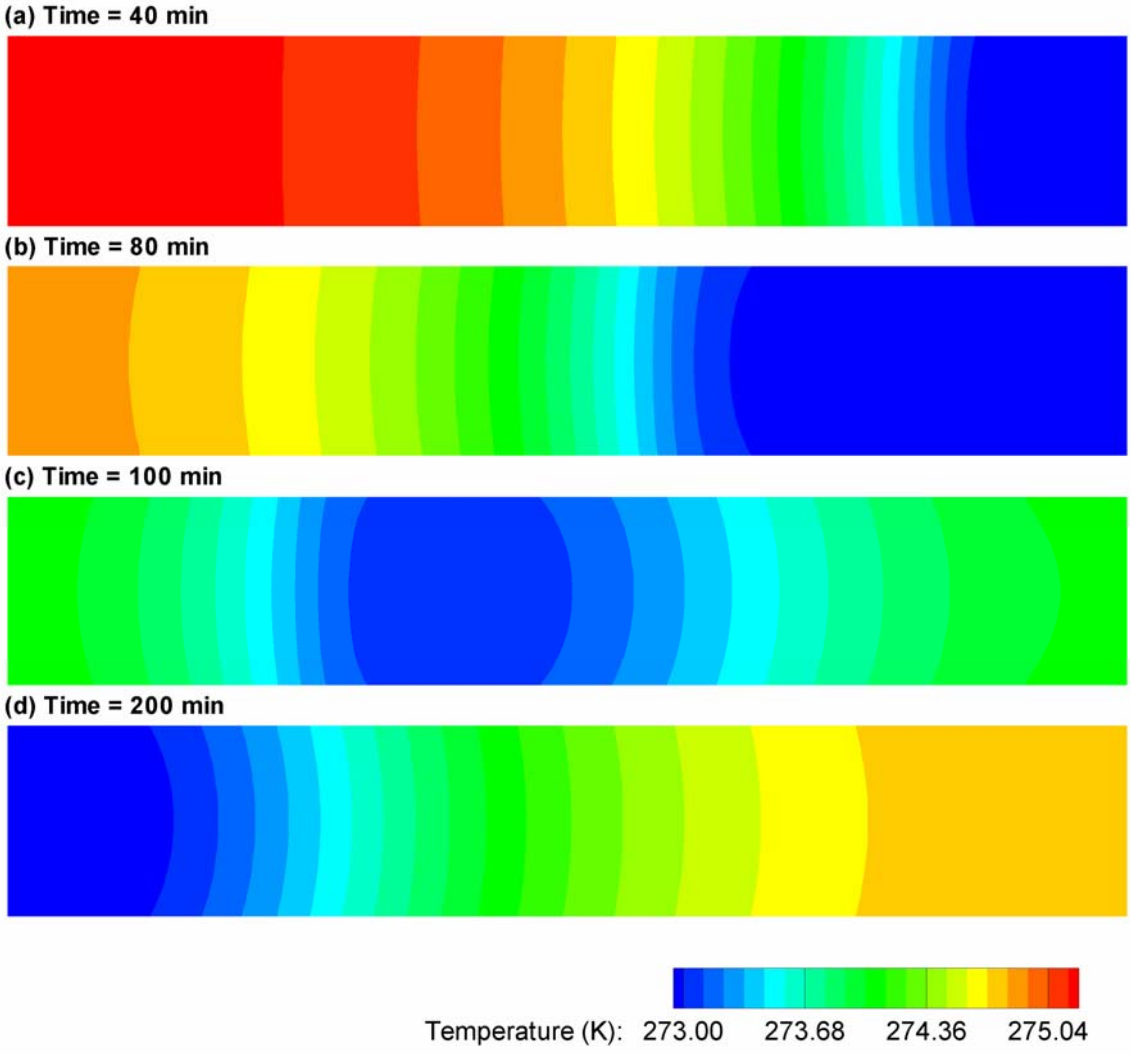

Figure 25. Temperature contours in the core sample at different times.

Figures 26, 27 and 28, respectively, display the saturation contours of hydrate, gas, and water, in the core sample at different times. Figure 26 shows that hydrate dissociation starts from the outlet valve where the pressure is lower than the equilibrium pressure. The dissociation front is roughly planar at the initiation of the dissociation process. As the front moves away from the outlet region, it develops a curvature due to the non-uniformity of the temperature field. Figure 26d shows that the majority of hydrate is dissociated after 200

minutes. As hydrate dissociates, methane and water are generated. From Figures 27 and 28 it is seen that the saturations of methane and water increase as the saturation of hydrate in the core sample decreases due to dissociation.

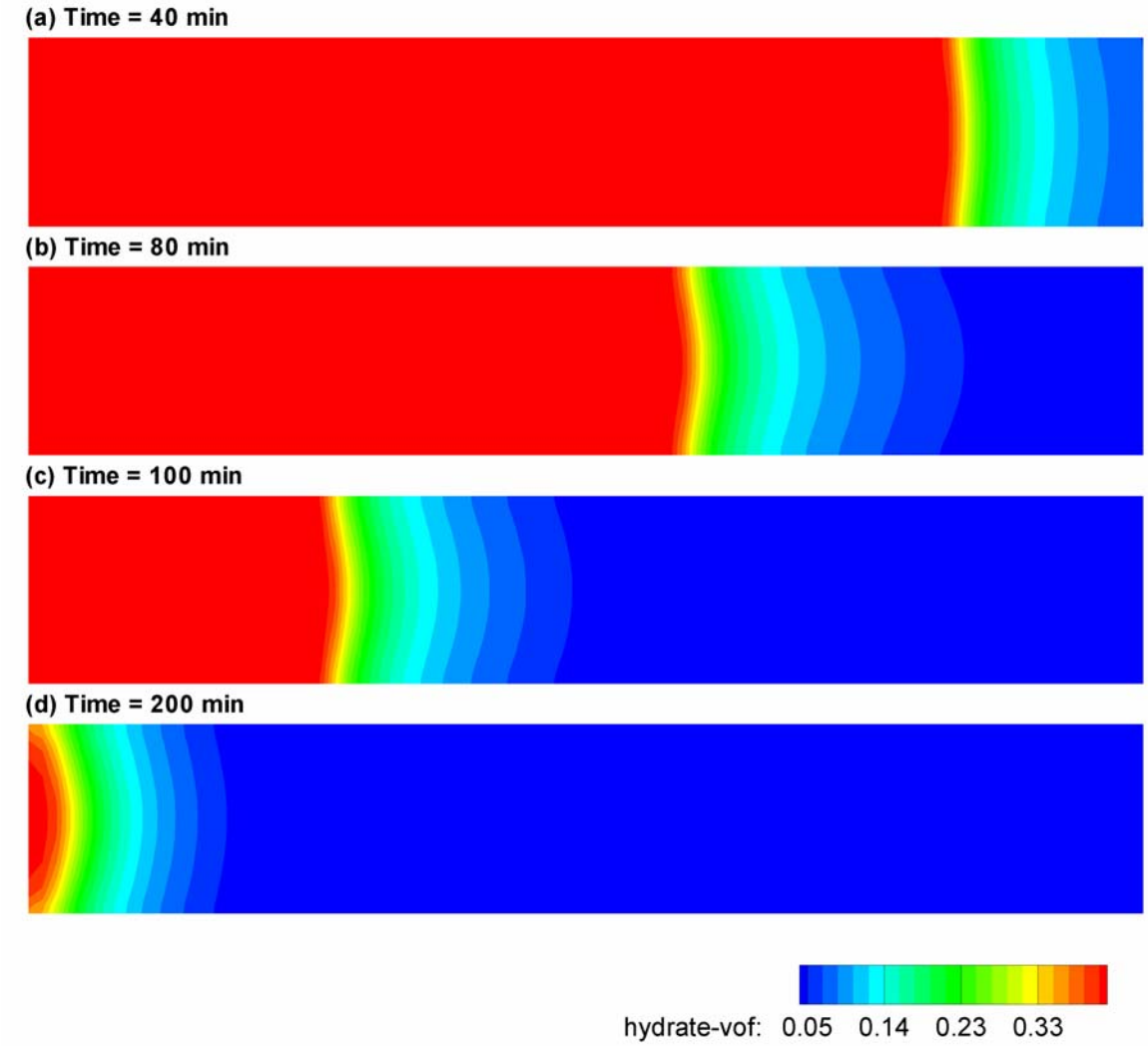

Figure 26. Hydrate saturation contours at different times.

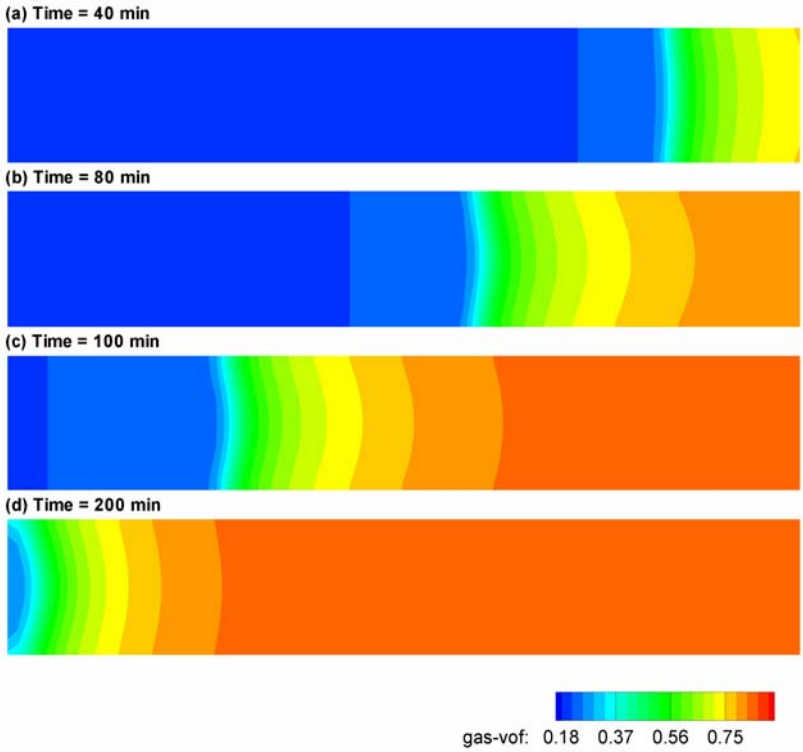

Figure 27. Methane gas saturation contours at different times.

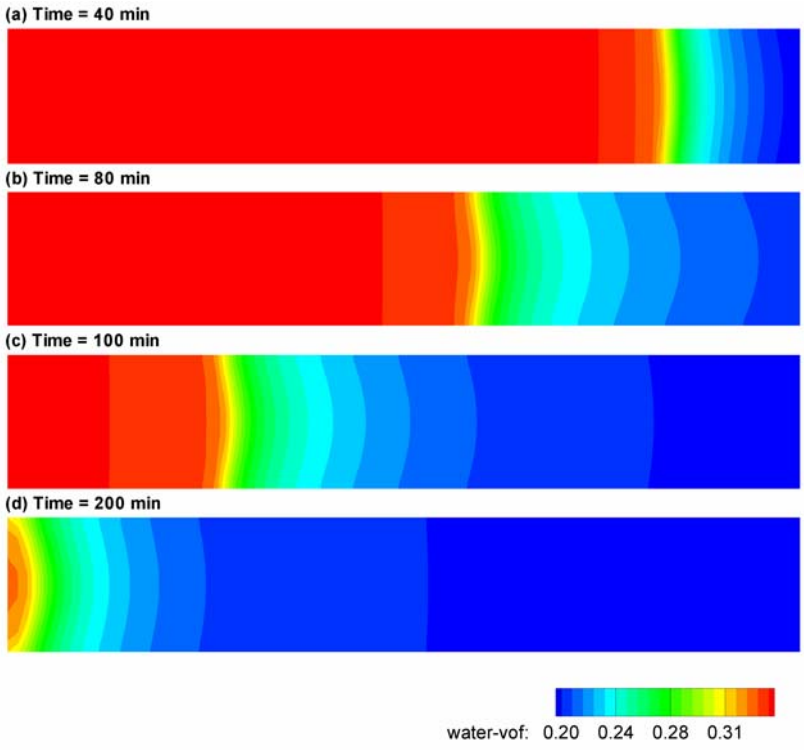

Figure 28. Water saturation contours at different times.

Comparison with Experimental Data

Masuda et al. (1999) have reported several numerical as well as experiments on dissociation of hydrate in a vessel that is similar to the present core sample. Here the present simulation results are compared with the experimental data of Masuda et al. (1999). Figure 29 show the simulated time variations of the temperature at sections (b)-(d) of the core sample. Here the simulated temperatures are averaged across the respective sections. The experimental data for time variation of temperature as reported by Masuda et al. (1999) are shown in this figure for comparison. It is seen that the simulation results follow the general pattern of the experimental data. The temperatures in all sections of the core sample for both simulation and experimental data decreases to a minimum as hydrate dissociates and then increases and approaches the surrounding temperature. As noted before, hydrate dissociation is an endothermic process and absorbs heat that causing the drop in the temperature. The free convection heat transfer then causes the core temperature to approach the surrounding air temperature.

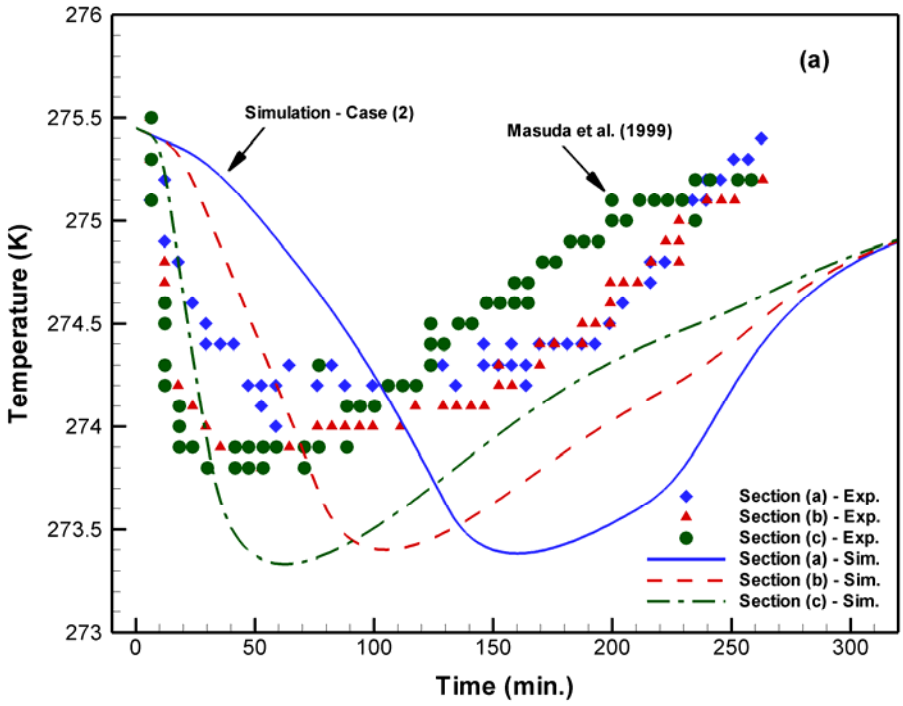

Figure 29. Comparison of simulated temperature variations with the experimental data of Masuda et al. (1999).

5. THERMODYNAMICALLY CONSISTENT MODEL FOR MULTIPHASE FLOWS IN POROUS MEDIA

A thermodynamically consistent continuum model for multiphase fluid mixture (including gas-liquid such as natural gas-water) flows through poro-elastic media is developed. The basic conservation laws developed via a volume averaging technique are considered. Effects of phasic equilibrated forces are included in the model. Based on the thermodynamics of the multiphase mixture flows, appropriate constitutive equations are formulated. The entropy inequality is exploited, and the method of Lagrangian multiplier is used along with the phasic conservation laws to derive the constitutive equations for the phasic stress tensors, equilibrated stress vectors and the interactions terms. The special cases of wave propagation in poro-elastic media saturated with multiphase fluids, and multiphase flows through porous media are studied. It is shown that the present theory leads to the extended Darcy's law and contains, as its special case, Biot's theory of saturated poro-elastic media.

Balance Laws

Consider a dispersed mixture of m distinct fluid phases in a deformable porous media. In the absence of chemical reaction and interfacial mass transfer, starting from the global conservation laws for each phase and using an spatial averaging method, the local forms of the laws for different constituents were developed by Whitaker (1986), Ahmadi (1987), Hassanizadeh and Gray (1993), and Kaviany (1995), among others. Accordingly, the differential forms of the equations of conservation of mass for each of phases becomes,

$$\frac{\partial \rho^s}{\partial t} + \frac{\partial}{\partial x_j}(\rho^s \, \tilde{v}_j^s) = 0 \tag{5-1}$$

$$\frac{\partial \rho^f}{\partial t} + \frac{\partial}{\partial x_j}(\rho^f \, \tilde{v}_j^f) = 0 \tag{5-2}$$

Here ρ is the mass density, and $\tilde{v}_i$ is the volume averaged mean velocity vector. The superscripts f refers to the f^{th} fluid phase and superscript s identifies the solid (porous) media. When the particulate and fluid phases are incompressible, it follows that

$$\rho^s = \rho_0^s \nu^s, \qquad \rho^f = \rho_0^f \nu^f \tag{5-3}$$

where ν is the mean volume fraction, and ρ_0 is the density of the material of a constituent.

Note that throughout this paper the concept of interpenetrating continua are used and it is

assumed that the equivalent phasic continua simultaneously occupy the same volume elements. If the density of the material of a constituent, ρ_0, is constant, Equations (5-1) and (5-2) can be restated as

$$\frac{\partial \nu^s}{\partial t} + \frac{\partial}{\partial x_j}(\nu^s \tilde{v}^s{}_j) = 0 \tag{5-4}$$

$$\frac{\partial \nu^f}{\partial t} + \frac{\partial}{\partial x_j}(\nu^f \tilde{v}^f{}_j) = 0 \tag{5-5}$$

The following constraint for fully saturated mixtures is imposed,

$$\sum_{f=1}^{m} \nu^f + \nu^s = 1 \tag{5-6}$$

Based on the Equation (5-2), the conversation of mass for the fluid mixture flow may be restated as

$$\frac{\partial \rho}{\partial t} + \frac{\partial}{\partial x_j}(\rho\, \tilde{v}_j) = 0 \tag{5-7}$$

where the density of the fluid mixture is

$$\rho = \sum_{f=1}^{m} \rho^f \tag{5-8}$$

The velocity of the mixture is also defined as

$$\rho\, \tilde{v}_j = \sum_{f=1}^{m} \rho^f\, \tilde{v}^f_j \tag{5-9}$$

The local forms of balance of linear momentum for each phase are given as,

$$\rho^s \frac{d\tilde{v}^s_i}{dt} = \rho^s\, f^s_i + \frac{\partial t^s_{ji}}{\partial x_j} + \bar{P}^s_i \tag{5-10}$$

$$\rho^f \frac{d\tilde{v}^f_i}{dt} = \rho^f\, f^f_i + \frac{\partial t^f_{ji}}{\partial x_j} + \bar{P}^f_i \tag{5-11}$$

where f_i is the body force per unit mass, t_{ij} is the average stress tensor, and $\overline{P}_i$ is the interaction momentum supply. The net interaction momentum supply for multiphase mixtures must be zero, i.e.;

$$\sum_{f=1}^{m} \overline{P}_i^f + \overline{P}_i^s = 0 \tag{5-12}$$

Equations governing the balance of equilibrated force are given by

$$\rho^s k^s \left\{ \frac{d\dot{v}^s}{dt} + (\dot{v}^s)^2 \right\} = \frac{\partial h_i^s}{\partial x_i} + \rho^s \ell^s + g^s \tag{5-13}$$

$$\rho^f k^f \left\{ \frac{d\dot{v}^f}{dt} + (\dot{v}^f)^2 \right\} = \frac{\partial h_i^f}{\partial x_i} + \rho^f \ell^f + g^f \tag{5-14}$$

where k is the equilibrated inertia, h_i is the equilibrated stress vector, ℓ is the equilibrated force per unit mass and g is the interaction equilibrated force supply (internal equilibrated force). Note that $\sum_{f=1}^{m} g^f + g^s \neq 0$, since g includes the inherent internal equilibrated force of each constituent.

The equation of conservation of equilibrated inertia are given as,

$$\frac{dk^s}{dt} - 2\dot{v}^s k^s = 0 \tag{5-15}$$

$$\frac{dk^f}{dt} - 2\dot{v}^f k^f = 0 \tag{5-16}$$

Equations governing the balance of equilibrated force and conservation of equilibrated inertia are the traces of the general stress-moment and micro-inertia equations developed by Twiss and Eringen (1971) and Ahmadi (1987).

The equation of conservation of energy for porous media and the fluid phase are given as

$$\rho^s \frac{de^s}{dt} = q^s_{j,j} + t^s_{ji} \tilde{v}^s_{j,i} + h^s_j \dot{v}^s_{,j} - g^s \dot{v}^s - \overline{P}^s_j \tilde{v}^s_j + r^s + e^{s+} \tag{5-17}$$

$$\rho^f \frac{de^f}{dt} = q^f_{j,j} + t^f_{ji} \tilde{v}^f_{j,i} + h^f_j \dot{v}^f_{,j} - g^f \dot{v}^f - \overline{P}^f_j \tilde{v}^f_j + r^f + e^{f+} \tag{5-18}$$

where e is mean internal energy per unit mass, q_j is the mean heat flux vector pointing outward of an enclosed volume, r is the internal heat source per unit volume and e^+ is the interaction energy supply. Note that,

$$\sum_{f=1}^{m} e^{f+} + e^{s+} = 0 \tag{5-19}$$

The entropy inequality for the mixture is given as,

$$\sum_{f=1}^{m} \left[\rho^f \dot{\eta}^f - (q_j^f / \theta^f)_{,j} - \frac{r^f}{\theta^f} \right] + \rho^s \dot{\eta}^s - (q_j^s / \theta^s)_{,j} - \frac{r^s}{\theta^s} \geq 0 \tag{5-20}$$

Here η is the mean entropy per unit mass and θ is the mean temperature.

Throughout this work the regular Cartesian tensor notation with Latin subscripts is used. Indices after a comma denote partial derivatives and d/dt stands for the substantial (total) time derivative.

The Helmholtz free energy function for the fluid phases and porous body are defined as,

$$\psi^s = e^s - \eta^s \theta^s \tag{5-21}$$

$$\psi^f = e^f - \eta^f \theta^f \tag{5-22}$$

By eliminating the internal heat source, r, between Equations (5-17), (5-18), and (5-20) and using Equations (5-21) and (5-22) the Clausius-Duhem inequality may be restated as,

$$\begin{aligned} &\sum_{f=1}^{m} \frac{1}{\theta^f} [-\rho^f (\dot{\psi}^f + \eta^f \dot{\theta}^f) + t_{ji}^f \tilde{v}_{j,i}^f + \frac{1}{\theta^f} q_j^f \theta_{,j}^f + h_j^f \dot{\nu}_{,j}^f - g^f \dot{\nu}^f - \tilde{v}_j^f \overline{P}_j^f + e^{f+}] \\ &+ \frac{1}{\theta^s} [-\rho^s (\dot{\psi}^s + \eta^s \dot{\theta}^s) + t_{ji}^s \tilde{v}_{j,i}^s + \frac{1}{\theta^s} q_j^s \theta_{,j}^s + h_j^s \dot{\nu}_{,j}^s - g^s \dot{\nu}^s - \tilde{v}_j^s \overline{P}_j^s + e^{s+}] \geq 0 \end{aligned} \tag{5-23}$$

Taking the time derivative of the Equation (5-6), we find

$$\dot{v}^s - \tilde{v}^s_j v^s_{,j} + \sum_{f=l}^{m} [\dot{v}^f - \tilde{v}^f_j v^f_{,j}] = 0 \tag{5-24}$$

The method of Lagrangian multipliers developed by Truesdell and Noll (1965) is used here to include the effect of constraints on the constitutive equations. Accordingly, multiplying Equations (5-24), (5-4) and (5-5), respectively, by Lagrangian multiplier functions, $\Lambda(x,t)$, $\frac{\Lambda^f(x,t)}{\theta^f}$, and $\frac{\Lambda^s(x,t)}{\theta^s}$, and adding the result to the entropy inequality given by Equation (5-23), it follows that

$$\begin{aligned}
&\sum_{f=l}^{m} \frac{1}{\theta^f}[-\rho^f(\dot{\psi}^f + \eta^f\dot{\theta}^f) + t^f_{ji}\tilde{v}^f_{j,i} + \frac{1}{\theta^f}q^f_j\theta^f_{,j} + h^f_j\dot{v}^f_{,j} + \Lambda^f v^f \tilde{v}^f_{j,j} \\
&\qquad -(g^f - \Lambda\theta^f - \Lambda^f)\dot{v}^f - (\bar{P}^f_j + \Lambda\theta^f v^f_{,j})\tilde{v}^f_j + e^{f+}] \\
&+\frac{1}{\theta^s}[-\bar{\rho}^s(\dot{\psi}^s + \eta^s\dot{\theta}^s) + t^s_{ji}\tilde{v}^s_{j,i} + \frac{1}{\theta^s}q^s_j\theta^s_{,j} + h^s_j\dot{v}^s_{,j} + \Lambda^s v^s \tilde{v}^s_{j,j} \\
&\qquad -(g^s - \Lambda\theta^s - \Lambda^s)\dot{v}^s - (\bar{P}^s_j + \Lambda\theta^s v^s_{,j})\tilde{v}^s_j + e^{s+}] \geq 0
\end{aligned} \tag{5-25}$$

For the fully saturated multiphase fluid flows (with incompressible constituents) through poro-elastic media, inequality (5-25) is the appropriate expression of the second law of thermodynamics.

Constitutive Equations

In this section, based on the averaged entropy inequality given by Equation (5-25), formulation of constitutive equations for multiphase flows in poro-elastic media is described. The following set of constitutive independent variables are postulated

$$\{S^s\} = \{k^s, v^s, v^s_{,i}, \dot{v}^s, \dot{v}^s_{,i}, \theta^s, \theta^s_{,i}, d^s_{ij}, e^s_{ii}\} \tag{5-26}$$

$$\{S^f\} = \{k^f, v^f, v^f_{,i}, \dot{v}^f, \dot{v}^f_{,i}, \theta^f, \theta^f_{,i}, d^f_{ij}, e^f_{ii}, e^s_{ii}\} \tag{5-27}$$

$$\{S^{fs}\} = \tilde{v}^{fs}_i \tag{5-28}$$

where d_{ij} is the deformation rate tensor defined as

$$d^s_{ij} = \frac{1}{2}(\tilde{v}^s_{i,j} + \tilde{v}^s_{j,i}), \; d^f_{ij} = \frac{1}{2}(\tilde{v}^f_{i,j} + \tilde{v}^f_{j,i}) \tag{5-29}$$

and, e^s_{ij} and e^f_{ij} are the solid and fluid strain tensors given by

$$e^s_{ij} = \frac{1}{2}(\tilde{u}^s_{i,j} + \tilde{u}^s_{j,i}) \tag{5-30}$$

$$e^f_{ij} = \frac{1}{2}(\tilde{u}^f_{i,j} + \tilde{u}^f_{j,i}) \tag{5-31}$$

Here $\tilde{u}^s_i$ and $\tilde{u}^f_i$ are the displacement vector of the porous matrix and f^{th} fluid constituents. In Equation (5-28) the relative velocity of the f^{th} fluid phase with respect to the porous medium, $\tilde{v}^{fs}_i$, is defined as

$$\tilde{v}^{fs}_i = \tilde{v}^f_i - \tilde{v}^s_i \tag{5-32}$$

It should be noted here that the mass densities are not included in the set of constitutive independent variables given by Equations (5-26), (5-27), and (5-28). This is because, for mixtures with incompressible constituents, the phasic mass densities are given in terms of phasic volume fractions in accordance to Equation (5-3). The dilatational strains of the fluid and solid constituents, however, are included in Equations (5-26) and (5-27).

We now propose the following set of frame-indifferent constitutive equations:

$$\begin{gathered}
\psi^s = \psi^s(k^s, \nu^s, \nu^s_{,i}, \dot{\nu}^s, \dot{\nu}^s_{,i}, \theta^s, \theta^s_{,i}, d^s_{ij}, e^s_{ii}, e^f_{ii}) \quad \psi^f = \psi^f(k^f, \nu^f, \nu^f_{,i}, \dot{\nu}^f, \dot{\nu}^f_{,i}, \theta^f, \theta^f_{,i}, d^f_{ij}, e^f_{ii}, e^s_{ii}) \\
t^s_{ij} = t^s_{ij}(k^s, \nu^s, \nu^s_{,i}, \dot{\nu}^s, \dot{\nu}^s_{,i}, \theta^s, \theta^s_{,i}, d^s_{ij}, e^s_{ij}, e^f_{ii}) \quad t^f_{ij} = t^f_{ij}(k^f, \nu^f, \nu^f_{,i}, \dot{\nu}^f, \dot{\nu}^f_{,i}, \theta^f, \theta^f_{,i}, d^f_{ij}, e^f_{ii}, e^s_{ii}) \\
h^s_i = h^s_i(k^s, \nu^s, \nu^s_{,i}, \dot{\nu}^s, \dot{\nu}^s_{,i}, \theta^s, \theta^s_{,i}, d^s_{ij}, e^s_{ij}, e^f_{ii}) \quad h^f_i = h^f_i(k^f, \nu^f, \nu^f_{,i}, \dot{\nu}^f, \dot{\nu}^f_{,i}, \theta^f, \theta^f_{,i}, d^f_{ij}, e^f_{ii}, e^s_{ii}) \\
q^s = q^s(k^s, \nu^s, \nu^s_{,i}, \dot{\nu}^s, \dot{\nu}^s_{,i}, \theta^s, \theta^s_{,i}, d^s_{ij}, e^s_{ij}, e^f_{ii}), \quad q^f = q^f(k^f, \nu^f, \nu^f_{,i}, \dot{\nu}^f, \dot{\nu}^f_{,i}, \theta^f, \theta^f_{,i}, d^f_{ij}, e^f_{ii}, e^s_{ii}) \\
\eta^s = \eta^s(k^s, \nu^s, \nu^s_{,i}, \dot{\nu}^s, \dot{\nu}^s_{,i}, \theta^s, \theta^s_{,i}, d^s_{ij}, e^s_{ij}, e^f_{ii}) \\
\eta^f = \eta^f(k^f, \nu^f, \nu^f_{,i}, \dot{\nu}^f, \dot{\nu}^f_{,i}, \theta^f, \theta^f_{,i}, d^f_{ij}, e^f_{ii}, e^s_{ii}) \\
P^s_j = P^s_j(k^s, \nu^s, \nu^s_{,i}, \dot{\nu}^s, \dot{\nu}^s_{,i}, \theta^s, \theta^s_{,i}, d^s_{ij}, \tilde{v}^{fs}_i, e^s_{ij}, e^f_{ii}) \\
P^f_j = P^f_j(k^f, \nu^f, \nu^f_{,i}, \dot{\nu}^f, \dot{\nu}^f_{,i}, \theta^f, \theta^f_{,i}, d^f_{ij}, \tilde{v}^{fs}_i, e^f_{ii}, e^s_{ii}) \\
g^s = g^s(k^s, \nu^s, \nu^s_{,i}, \dot{\nu}^s, \dot{\nu}^s_{,i}, \theta^s, \theta^s_{,i}, d^s_{ij}, \tilde{v}^{fs}_i, e^s_{ij}, e^f_{ii}) \\
g^f = g^f(k^f, \nu^f, \nu^f_{,i}, \dot{\nu}^f, \dot{\nu}^f_{,i}, \theta^f, \theta^f_{,i}, d^f_{ij}, \tilde{v}^{fs}_i, e^f_{ii}, e^s_{ii}) \\
e^{s+} = e^{s+}(k^s, \nu^s, \nu^s_{,i}, \dot{\nu}^s, \dot{\nu}^s_{,i}, \theta^s, \theta^s_{,i}, d^s_{ij}, \tilde{v}^{fs}_{ij}, e^s_{ij}, e^f_{ii}) \\
e^{f+} = e^{f+}(k^f, \nu^f, \nu^f_{,i}, \dot{\nu}^f, \dot{\nu}^f_{,i}, \theta^f, \theta^f_{,i}, d^f_{ij}, \tilde{v}^{fs}_{ij}, e^f_{ii}, e^s_{ii})
\end{gathered} \tag{5-33}$$

It should be noted here that, according to the principle of equipresence of continuum mechanics, in general, all the constitutive dependent variables must be functions of all the independent constitutive variables. However, for simplicity of analysis, this principle was not fully utilized in constitutive equations given by (5-33). Furthermore, it is also assumed that, the porous medium free energy function is also a function of strain rate tensor.

Evaluating $\dot{\psi}^s$ and $\dot{\psi}^f$ from Equations (5-33), and substituting the results into the inequality (5-25), it follows that

$$\begin{aligned}
&\sum_{f=1}^{m}\frac{1}{\theta^f}[-\rho^f(\frac{\partial\psi^f}{\partial\theta^f}+\eta^f)\dot{\theta}^f-\rho^f(\frac{\partial\psi^f}{\partial\dot{v}^f}\ddot{v}^f+\frac{\partial\psi^f}{\partial\dot{v}^f_{,j}}\dot{\ddot{v}}^f_{,j}+\frac{\partial\psi^f}{\partial\theta^f_{,j}}\dot{\bar{\theta}}^f_{,j}+\frac{\partial\psi^f}{\partial d^f_{ij}}\dot{d}^f_{ij})\\
&+(t^f_{ji}+(-\rho^f\frac{\partial\psi^f}{\partial e^f_{kk}}-\frac{\nu^f\theta^f}{(1-\nu^s)\theta^s}\frac{\partial\psi^s}{\partial e^f_{kk}}+\Lambda^f\nu^f)\delta_{ij}+\rho^f\frac{\partial\psi^f}{\partial\nu^f_{,j}}\nu^f_{,i})d^f_{ij}\\
&+(\rho^f\frac{\partial\psi^f}{\partial\nu^f_{,j}}\nu^f_{,i})\tilde{v}^f_{[i,j]}+(h^f_j-\rho^f\frac{\partial\psi^f}{\partial\nu^f_{,j}})\dot{\nu}^f_{,j}-(-\pi^f+\rho^f\frac{\partial\psi^f}{\partial\nu^f}+g^f-\Lambda\theta^f-\Lambda^f)\dot{\nu}^f\\
&-(\bar{P}^f_j+\Lambda\theta^f\nu^f_{,j})\tilde{v}^f_j+q^f_j(\ln\theta^f)_{,j}+e^{f+}]\\
&+\frac{1}{\theta^s}[-\rho^s(\frac{\partial\psi^s}{\partial\theta^s}+\eta^s)\dot{\theta}^s-\rho^s(\frac{\partial\psi^s}{\partial\dot{v}^s}\ddot{v}^s+\frac{\partial\psi^s}{\partial\dot{v}^s_{,j}}\dot{\ddot{v}}^s_{,j}+\frac{\partial\psi^f}{\partial\theta^s_{,j}}\dot{\bar{\theta}}^s_{,j}+\frac{\partial\psi^s}{\partial d^s_{ij}}\dot{d}^s_{ij})\\
&+(t^s_{ji}+\Lambda^s\nu^s\delta_{ji}+\rho^s\frac{\partial\psi^s}{\partial\nu^s_j}\nu^s_{,i}-\rho^s\frac{\partial\psi^s}{\partial e^s_{ij}}-\theta^s\sum_{f=1}^{m}\frac{\rho^f}{\theta^f}\frac{\partial\psi^f}{\partial e^s_{kk}}\delta_{ij})d^s_{ij}+(\rho^s\frac{\partial\psi^s}{\partial\nu^s_{,j}}\nu^s_{,i})\tilde{v}^s_{[i,j]}\\
&+(h^s_j-\rho^s\frac{\partial\psi^s}{\partial\nu^s_{,j}})\dot{\nu}^s_{,j}-(-\pi^s+\rho^s\frac{\partial\psi^s}{\partial\nu^s}+g^s-\Lambda\theta^s-\Lambda^s)\dot{\nu}^s\\
&-(\bar{P}^s_j+\Lambda\theta^s\nu^s_{,j})\tilde{v}^s_j+q^s_j(\ln\theta^s)_{,j}+e^{s+}]\geq 0
\end{aligned} \tag{5-34}$$

where, $\tilde{v}_{[i,j]}$ is the anti-symmetric part of the velocity gradient tensor. The micro pressures in the distributed solid and fluid bodies, π^s and π^f, are defined as

$$\pi^s=-2\rho^f\frac{\partial\psi^s}{\partial k^s}k^s \tag{5-35}$$

$$\pi^f=-2\rho^f\frac{\partial\psi^f}{\partial k^f}k^f \tag{5-36}$$

Demanding that the entropy inequality (5-34) holds for all independent variations of

$\dot{\theta}^f, \dot{\theta}^f_{,i}, \dot{\theta}^s, \dot{\theta}^s_{,i}, \ddot{\nu}^f, \dot{\tilde{\nu}}^f_{,i}, \ddot{\nu}^s, \dot{\tilde{\nu}}^s_{,i}, \dot{d}^s_{ij}, \dot{d}^f_{ij}$ and $\tilde{v}^f_{[j,i]}, \tilde{v}^s_{[j,i]}$, it follows that

$$\eta^s = -\frac{\partial \psi^s}{\partial \theta^s}, \ \eta^f = -\frac{\partial \psi^f}{\partial \theta^f} \tag{5-37}$$

$$\frac{\partial \psi^f}{\partial \dot{\nu}^f} = \frac{\partial \psi^f}{\partial \dot{\nu}^f_{,i}} = \frac{\partial \psi^s}{\partial \dot{\nu}^s} = \frac{\partial \psi^s}{\partial \dot{\nu}^s_{,i}} = 0 \tag{5-38}$$

$$\rho^f \varepsilon_{ikj} \frac{\partial \psi^f}{\partial \nu^f_{,k}} \nu^f_{,j} = \rho^s \varepsilon_{ikj} \frac{\partial \psi^s}{\partial \nu^s_{,k}} \nu^s_{,j} = 0 \tag{5-39}$$

$$\frac{\partial \psi^f}{\partial \theta^f_{,i}} = \frac{\partial \psi^f}{\partial d^f_{ij}} = \frac{\partial \psi^s}{\partial \theta^s_{,i}} = \frac{\partial \psi^s}{\partial d^s_{ij}} = 0 \tag{5-40}$$

Introducing the elastic and dissipative parts of the stress tensor and equilibrated stress vector as

$$t^s_{ij} = {}_E t^s_{ij} + {}_D t^s_{ij}, \quad t^f_{ij} = {}_E t^f_{ij} + {}_D t^f_{ij} \tag{5-41}$$

$$h^s_i = {}_E h^s_i + {}_D h^s_i, \quad h^f_i = {}_E h^f_i + {}_D h^f_i \tag{5-42}$$

where the elastic parts of the stresses as obtained from entropy inequality (5-34), are given by

$${}_E t^s_{ij} = -\Lambda^s \nu^s \delta_{ij} - \rho^s \frac{\partial \psi^s}{\partial \nu^s_{,i}} \nu^s_{,j} + \rho^s \frac{\partial \psi^s}{\partial e^s_{ij}} + \theta^s \sum_{f=1}^{m} \frac{\rho^f}{\theta^f} \frac{\partial \psi^f}{\partial e^s_{kk}} \delta_{ij} \tag{5-43}$$

$${}_E t^f_{ij} = (\rho^f \frac{\partial \psi^f}{\partial e^f_{mm}} + \frac{\nu^f \theta^f}{(1-\nu^s)\theta^s} \rho^s \frac{\partial \psi^s}{\partial e^f_{mm}} - \Lambda^f \nu^f) \delta_{ij} - \rho^f \frac{\partial \psi^f}{\partial \nu^f_{,i}} \nu^f_{,j} \tag{5-44}$$

$${}_E h^s_i = \rho^s \frac{\partial \psi^s}{\partial \nu^s_{,i}}, \quad {}_E h^f_i = \rho^f \frac{\partial \psi^f}{\partial \nu^f_{,i}} \tag{5-45}$$

Using Equations (5-37)-(5-40), and (5-43)-(5-45), inequality (5-34) reduces to

$$\sum_{f=1}^{m}\frac{1}{\theta^f}[{}_D t^f_{ji} d^f_{ij} + {}_D h^f_j \dot{v}^f_{,j} - (-\pi^f + \rho^f \frac{\partial \psi^f}{\partial \nu^f} + g^f - \Lambda\theta^f - \Lambda^f)\dot{v}^f - (\bar{P}^f_j + \Lambda\theta^f \nu^f_{,j})\tilde{v}^f_j$$
$$+ q^f_j (\ln\theta^f)_{,j} + e^{f+}]$$
$$+ \frac{1}{\theta^s}[{}_D t^s_{ji} d^s_{ij} + {}_D h^s_j \dot{v}^s_{,j} - (-\pi^s + \rho^s \frac{\partial \psi^s}{\partial \nu^s} + g^s - \Lambda\theta^s - \Lambda^s)\dot{v}^s - (\bar{P}^s_j + \Lambda\theta^s \nu^s_{,j})\tilde{v}^s_j$$
$$+ q^s_j (\ln\theta^s)_{,j} + e^{s+}] \geq 0 \tag{5-46}$$

For the dissipative parts of stresses of an isotropic mixture the following set of constitutive equations is then proposed,

$${}_D t^s_{ij} = 0 \tag{5-47}$$
$${}_D t^f_{ij} = \lambda^f d^f_{mm}\delta_{ij} + 2\mu^f d^f_{ij} \tag{5-48}$$
$${}_D h^s_k = 0 \tag{5-49}$$
$${}_D h^f_k = H^f \dot{v}^f_{,k} \tag{5-50}$$

The entropy inequality (5-46) imposes the following restrictions on the viscosity coefficients

$$3\lambda^f + 2\mu^f \geq 0, \quad \mu^f \geq 0 \tag{5-51}$$

From inequality (5-46) the constitutive equations for the internal equilibrated forces are proposed as

$$g^s = \pi^s - \rho^s \frac{\partial \psi^s}{\partial \nu^s} + \Lambda\theta^s + \Lambda^s - G^s \dot{v}^s \tag{5-52}$$
$$g^f = \pi^f - \rho^f \frac{\partial \psi^f}{\partial \nu^f} + \Lambda\theta^f + \Lambda^f - G^f \dot{v}^f \tag{5-53}$$

where

$$G^s \geq 0, \quad G^f \geq 0 \tag{5-54}$$

Isothermal Mixture

We now assume an isothermal mixture for deriving the additional required constitutive equations. For an isothermal mixture, $\theta^f = \theta^s = \theta$, the interaction momentum supply terms of entropy inequality must satisfy the following inequality,

$$-(\bar{P}_j^s + \Lambda\theta v_{,j}^s)\tilde{v}_j^s + \sum_{f=1}^{m} -(\bar{P}_j^f + \Lambda\theta v_{,j}^f)\tilde{v}_j^f \geq 0 \tag{5-55}$$

Using the Equations (5-6) and (5-12), Equation (5-55) may be restated as:

$$\sum_{f=1}^{m} (\bar{P}_j^f + \Lambda\theta v_{,j}^f)(\tilde{v}_j^s - \tilde{v}_j^f) \geq 0 \tag{5-56}$$

The mean interaction momentum supply for the fluid phases satisfying Equation (5-56) are given as

$$\bar{P}_j^f = \sum_{f'=1}^{m} D^{ff'}(\tilde{v}_j^s - \tilde{v}_j^{f'}) + p v_{,j}^f \tag{5-57}$$

where the drag coefficient $D^{ff'}$ is a positive definite $(m \times m)$ matrix, and $p = -\Lambda\theta$ is the hydrostatic pressure. The corresponding momentum supply for the porous matrix is given by

$$\bar{P}_j^s = \sum_{f=1}^{m} \sum_{f'=1}^{m} D^{ff'}(\tilde{v}_j^{f'} - \tilde{v}_j^s) + p v_{,j}^s \tag{5-58}$$

The Helmholtz free energy function for the porous matrix and the phasic fluid phases are assumed to be given as

$$\begin{aligned} \rho^s \psi^s &= \alpha^s v_{,j}^s v_{,j}^s \\ &\quad + \nu^s \left[\frac{1}{2} a_0^s (\nu^s)^2 + \frac{1}{2} \lambda^s e_{kk}^s e_{mm}^s + \mu^s e_{ij}^s e_{ij}^s + b_0^s \nu^s e_{kk}^s + \sum_{f=1}^{m} c_0^{sf} \nu^s e_{kk}^f \right. \\ &\qquad \left. + \frac{1}{2} \sum_{f=1}^{m} d_0^{sf} e_{kk}^f e_{mm}^f + \sum_{f=1}^{m} e_0^{sf} e_{kk}^f e_{mm}^s \right] \end{aligned} \tag{5-59}$$

$$\begin{aligned} \rho^f \psi^f &= \alpha^f v_{,j}^f v_{,j}^f \\ &\quad + \nu^f \left[\frac{1}{2} \alpha_0^f (\nu^f)^2 + b_0^f \nu^f e_{kk}^s + c_0^f \nu^f e_{kk}^f + \frac{1}{2} d_0^f e_{kk}^f e_{mm}^f + e_0^f e_{kk}^f e_{mm}^s + \frac{1}{2} f_0^f e_{kk}^s e_{mm}^s \right] \end{aligned} \tag{5-60}$$

where α^s and α^f are positive functions of corresponding volume fractions. For the strain free energy functions given by Equation (5-59) and (5-60) to positive, the following restriction on the material properties are imposed

$$\mu^s \geq 0\,, \quad \lambda^s \geq 0$$

$$\alpha^s \geq 0,\ a_0^s \geq 0,\ (b_0^s)^2 \leq a_0^s \lambda^s$$
$$d_0^{sf} \geq 0,\ e_0^{sf} \geq 0,\ (c_0^{sf})^2 \leq d_0^{sf} e_0^{sf}$$
$$\alpha^f \geq 0,\ \ a_0^f \geq 0,\ \ f_0^f \geq 0,$$
$$(b_0^f)^2 \leq a_0^f f_0^f,\ \ d_0^f \geq 0, (e_0^f)^2 \leq d_0^f f_0^f \tag{5-61}$$

Equations (5-35) and (5-36) for the free energy functions given (5-59) and (5-60), imply that the micro pressures vanish identically, i.e.,

$$\pi^s = \pi^f = 0 \tag{5-62}$$

The elastic part of the constitutive equations for poro-elastic matrix and the fluid phases given by (5-43)-(5-45) now become

$$\begin{aligned} {}_E t_{ij}^s = &-\Lambda^s \nu^s \delta_{ij} - 2\alpha^s \nu_{,i}^s \nu_{,j}^s + \lambda^s e_{kk}^s \delta_{ij} + 2\mu^s e_{ij}^s \\ &+ \nu^s [b_0^s \nu^s + \sum_{f=1}^{m} b_0^f \nu^f + \sum_{f=1}^{m} (e_0^f + e_0^{sf}) e_{mm}^f + \sum_{f=1}^{m} f_0^f e_{mm}^s] \delta_{ij} \end{aligned} \tag{5-63}$$

$$\begin{aligned} {}_E t_{ij}^f = &-\Lambda^f \nu^f \delta_{ij} - 2\alpha^f \nu_{,i}^f \nu_{,j}^f \\ &+ \nu^f [c_0^f \nu^f + \frac{\nu^f}{1-\nu^s} c_0^{sf} \nu^s + (d_0^f + \frac{\nu^f}{1-\nu^s} d_0^{sf}) e_{kk}^f \\ &\qquad + (e_0^f + \frac{\nu^f}{1-\nu^s} e_0^{sf}) e_{kk}^s] \delta_{ij} \end{aligned} \tag{5-64}$$

$${}_E h_i^s = 2\alpha^s \nu_{,j}^s \tag{5-65}$$

$${}_E h_i^f = 2\alpha^f \nu_{,j}^f \tag{5-66}$$

Similarly, the constitutive equations for the internal equilibrated forces given by (5-52) and (5-53) now become

$$g^s = -a_0^s (\nu^s)^2 - \nu^s \nu_{,j}^s \nu_{,j}^s \frac{d}{d\nu^s}(\frac{\alpha^s}{\nu^s}) - \nu^s (b_0^s e_{kk}^s + \sum_{f=1}^{m} c_0^{sf} e_{kk}^f) - p + \Lambda^s - G^s \dot{\nu}^s \tag{5-67}$$

$$g^f = -a_0^f(\nu^f)^2 - \nu^f \nu^f_{,j} \nu^f_{,j} \frac{d}{d\nu^f}\left(\frac{\alpha^f}{\nu^f}\right) - \nu^f (b_0^f e^s_{kk} + c_0^f e^f_{kk}) - p + \Lambda^f - G^f \dot{\nu}^f \tag{5-68}$$

The constitutive relationships for the multiphase flows given by the Equations (5-57), (5-58), (5-62)-(5-68) are consistent with the average Clausius-Duhem inequality.

Equations of Motion

Direct substitution of the constitutive equations into the equations of balance of linear momentum and balance of equilibrated force given by Equations (5-10), (5-11), (5-13) and (5-14) yield the basic equation of motion of multiphase flow through poro-elastic media. These equations for porous media and fluid phase are:

Linear momentum of porous media and fluid phases

$$\begin{aligned}\rho_0^s \nu^s \frac{d\tilde{v}_i^s}{dt} &= \rho^s f_i^s - (\Lambda^s \nu^s)_{,i} - 2(\alpha^s \nu^s_{,j} \nu^s_{,i})_{,j} + [\nu^s \mu^s (\tilde{u}^s_{i,j} + \tilde{u}^s_{j,i})]_{,j} \\ &\quad + [\nu^s \lambda^s \tilde{u}^s_{k,k} + \nu^s [b_0^s \nu^s + \sum_{f=1}^{m} b_0^f \nu^f + \sum_{f=1}^{m} (e_0^f + e_0^{sf}) \tilde{u}^f_{m,m} + \sum_{f=1}^{m} f_0^f \tilde{u}^s_{m,m}]]_{,i} \\ &\quad + \sum_{f=1}^{m} \sum_{f'=1}^{m} D^{ff'} (\tilde{v}_i^{f'} - \tilde{v}_i^s) + p\nu^s_{,i}\end{aligned} \tag{5-69}$$

$$\begin{aligned}\rho_0^f \nu^f \frac{d\tilde{v}_i^f}{dt} &= \rho^f f_i^f - (\Lambda^f \nu^f)_{,i} - 2(\alpha^f \nu^f_{,j} \nu^f_{,i})_{,j} + [\mu^f (\tilde{v}^f_{j,i} + \tilde{v}^f_{i,j})]_{,j} \\ &\quad + \sum_{f'=1}^{m} D^{ff'} (\tilde{v}_i^s - \tilde{v}_i^{f'}) + p\nu^f_{,i} \\ &\quad + [\lambda^f \tilde{v}^f_{j,j} + \nu^f [c_0^f \nu^f + \frac{\nu^f}{1-\nu^s} c_0^{sf} \nu^s + (d_0^f + \frac{\nu^f}{1-\nu^s} d_0^{sf}) \tilde{u}^f_{k,k} \\ &\qquad + (e_0^f + \frac{\nu^f}{1-\nu^s} e_0^{sf}) \tilde{u}^s_{k,k}]]_{,i}\end{aligned} \tag{5-70}$$

Equilibrated force of porous media and fluid phase

$$\rho_0^s \nu^s k^s \left(\frac{d\dot{\nu}^s}{dt} + (\dot{\nu}^s)^2\right) = 2(\alpha^s \nu^s_{,j})_{,j} - a_0^s (\nu^s)^2 - \nu^s \frac{d}{d\nu^s}\left(\frac{\alpha^s}{\nu^s}\right)\nu^s_{,j}\nu^s_{,j}$$
$$- \nu^s (b_0^s e^s_{kk} + \sum_{f=1}^{m} c_0^{sf} e^f_{kk}) - p + \Lambda^s - G^s \dot{\nu}^s + \rho^s \ell^s \tag{5-71}$$

$$\rho_0^f \nu^f k^f \left(\frac{d\dot{\nu}^f}{dt} + (\dot{\nu}^f)^2\right) = 2(\alpha^f \nu^f_{,j})_{,j} + (H^f \dot{\nu}^f_{,j})_{,j} - a_0^f (\nu^f)^2 - \nu^f \frac{d}{d\nu^f}\left(\frac{\alpha^f}{\nu^f}\right)\nu^f_{,j}\nu^f_{,j}$$
$$- \nu^f (b_0^f e^s_{kk} + c_0^f e^f_{kk}) - p + \Lambda^f - G^f \dot{\nu}^f + \rho^f \ell^f \tag{5-72}$$

Equations (5-69)-(5-72) together with equations of conservation of mass for porous media and fluid phase given by Equations (5-4), (5-5), the saturation condition (5-6), and the equilibrated inertia given by Equations (5-15) and (5-16) form a complete set of $8(m+1)+1$ equations for determining $8(m+1)+1$ unknowns, $\tilde{v}_i^s, \tilde{v}_i^f, \nu^s, \nu^f, \dot{\nu}^s, \dot{\nu}^f, k^s, k^f, \Lambda^s, \Lambda^f$ and p.

Simplified Equations of Motions

In the absence of equilibrated inertia and equilibrated body force and when the dissipative parts of the equilibrated force are also negligible, i.e.

$$k^s = 0,\ k^f = 0,\ \ell^f = 0,\ \ell^s = 0,\ H^f = 0 \tag{5-73}$$

Equations (5-71) and (5-72) can be solved for the Lagrangian multiplier Λ^s and Λ^f,

$$\Lambda^s = -2\alpha^s \nu^s_{,jj} - \left(\frac{d\alpha^s}{d\nu^s} + \frac{\alpha^s}{\nu^s}\right)\nu^s_{,j}\nu^s_{,j} + a_0^s (\nu^s)^2 + \nu^s (b_0^s e^s_{kk} + \sum_{f=1}^{m} c_0^{sf} e^f_{kk}) \tag{5-74}$$
$$+ p + G^s \dot{\nu}^s$$

$$\Lambda^f = -2\alpha^f \nu^f_{,jj} - \left(\frac{d\alpha^f}{d\nu^f} + \frac{\alpha^f}{\nu^f}\right)\nu^f_{,j}\nu^f_{,j} + a_0^f (\nu^f)^2 + \nu^f (b_0^f e^s_{kk} + c_0^f e^f_{kk}) \tag{5-75}$$
$$+ p + G^f \dot{\nu}^f$$

Employing Equations (5-74) and (5-75), Equations (5-69) and (5-70) may be restated as

$$\rho_0^s \nu^s \frac{d\tilde{v}_i^s}{dt} = \rho_0^s \nu^s f_i^s + 2\alpha^s \nu^s \nu^s_{,jji} + 2\nu^s \frac{d\alpha^s}{d\nu^s}(\nu^s_{,i}\nu^s_{,jj} + \nu^s_{,ji}\nu^s_{,j})$$
$$+ \nu^s \frac{d^2\alpha^s}{d(\nu^s)^2}\nu^s_{,j}\nu^s_{,j}\nu^s_{,i} - 3a_0^s(\nu^s)^2\nu^s_{,i} - 2\nu^s\nu^s_{,i}(b_0^s e_{kk}^s + \sum_{f=1}^{m} c_0^{sf} e_{kk}^f)$$
$$+ [\nu^s\mu^s(\tilde{u}^s_{i,j} + \tilde{u}^s_{j,i})]_{,j} + \sum_{f=1}^{m}\sum_{f'=1}^{m} D^{ff'}(\tilde{v}_i^{f'} - \tilde{v}_i^s) - \nu^s p_{,i} - (G^s\nu^s\dot{\nu}^s)_{,i}$$
$$+ \{\nu^s\lambda^s\tilde{u}^s_{k,k} + \nu^s[b_0^s\nu^s + \sum_{f=1}^{m} b_0^f\nu^f + \sum_{f=1}^{m}(e_0^f + e_0^{sf})\tilde{u}^f_{m,m} + \sum_{f=1}^{m} f_0^f\tilde{u}^s_{m,m}]\}_{,i} \tag{5-76}$$

$$\rho_0^f \nu^f \frac{d\tilde{v}_i^f}{dt} = \rho_0^f \nu^f f_i^f + 2?^f \nu^f \nu^f_{,jji} + 2\nu^f \frac{d\alpha^f}{d\nu^f}(\nu^f_{,i}\nu^f_{,jj} + \nu^f_{,ji}\nu^f_{,j})$$
$$+ \nu^f \frac{d^2\alpha^f}{d(\nu^f)^2}\nu^f_{,j}\nu^f_{,j}\nu^f_{,i} - 3a_0^f(\nu^f)^2\nu^f_{,i} - 2\nu^f\nu^f_{,i}(b_0^f e_{kk}^s + c_0^f e_{kk}^f)$$
$$+ [\mu^f(\tilde{v}^f_{j,i} + \tilde{v}^f_{i,j})]_{,j} + \sum_{f'=1}^{m} D^{ff'}(\tilde{v}_i^s - \tilde{v}_i^{f'}) - \nu^f p_{,i} - (G^f\nu^f\dot{\nu}^f)_{,i}$$
$$+ \{\lambda^f\tilde{v}^f_{j,j} + \nu^f[c_0^f\nu^f + \frac{\nu^f}{1-\nu^s}c_0^{sf}\nu^s + (d_0^f + \frac{\nu^f}{1-\nu^s}d_0^{sf})\tilde{u}^f_{k,k}$$
$$+ (e_0^f + \frac{\nu^f}{1-\nu^s}e_0^{sf})\tilde{u}^s_{k,k}]\}_{,i} \tag{5-77}$$

Here, Equations (5-76) and (5-77) together with Equations (5-4), (5-5) and (5-6) now form a set of $6(m+1)+1$ for determining $6(m+1)+1$ unknowns, $\tilde{v}_i^s, \tilde{v}_i^f, \nu^s, \nu^f, \dot{\nu}^s, \dot{\nu}^f$ and p.

When the material coefficients $\alpha^s, \alpha^f, \lambda^s, \lambda^f, G^s, G^f, \mu^s$ and μ^f are constants, Equations (5-76) and (5-77) may be restated as

$$\rho_0^s \nu^s \frac{d\tilde{v}_i^s}{dt} = \rho_0^s \nu^s f^s + 2\alpha^s \nu^s \nu^s_{,jji} - 3a_0^s(\nu^s)^2\nu^s_{,i} - 2\nu^s\nu^s_{,i}(b_0^s\tilde{u}^s_{k,k} + \sum_{f=1}^{m} c_0^{sf}\tilde{u}^f_{k,k})$$
$$+ \mu^s[\nu^s(\tilde{u}^s_{i,j} + \tilde{u}^s_{j,i})]_{,j} + \sum_{f=1}^{m}\sum_{f'=1}^{m} D^{ff'}(\tilde{v}_i^{f'} - \tilde{v}_i^s) - \nu^s p_{,i} - G^s(\nu^s\dot{\nu}^s)_{,i}$$
$$+ \lambda^s[\nu^s\tilde{u}^s_{k,k}]_{,i} + \{\nu^s[b_0^s\nu^s + \sum_{f=1}^{m} b_0^f\nu^f + \sum_{f=1}^{m}(e_0^f + e_0^{sf})\tilde{u}^f_{m,m} + \sum_{f=1}^{m} f_0^f\tilde{u}^s_{m,m}]\}_{,i} \tag{5-80}$$

$$\rho_0^f \nu^f \frac{d\tilde{v}_i^f}{dt} = \rho_0^f \nu^f f_i^f + 2\alpha^f \nu^f \nu^f_{,jji} - 3a_0^f (\nu^f)^2 \nu^f_{,i} - 2\nu^f \nu^f_{,i} (b_0^f \tilde{u}^s_{k,k} + c_0^f \tilde{u}^f_{k,k})$$
$$+ \mu^f [(\tilde{v}^f_{j,i} + \tilde{v}^f_{i,j})]_{,j} + \sum_{f'=1}^{m} D^{ff'} (\tilde{v}_i^s - \tilde{v}_i^{f'}) - \nu^f p_{,i} - G^f (\nu^f \dot{\gamma}^f)_{,i} + \lambda^f \tilde{v}^f_{j,ji}$$
$$+ \{\nu^f [c_0^f \nu^f + \frac{\nu^f}{1-\nu^s} c_0^{sf} \nu^s + (d_0^f + \frac{\nu^f}{1-\nu^s} d_0^{sf}) \tilde{u}^f_{k,k} + (e_0^f + \frac{\nu^f}{1-\nu^s} e_0^{sf}) \tilde{u}^s_{k,k}]\}_{,i}$$

(5-81)

Equations (5-80) and (5-81) are the simplified form of the general equations of motion of multiphase flows in poroelastic media.

Special Cases

In this section special limiting cases of the general form of the governing equations are examined.

Saturated Poroelastic Media

Consider a poroelastic media whose pores are saturated with multiphase fluids. For nearly constant solid and fluid volume fractions (nearly constant porosity), the linearized form of Equations (5-80) and (5-81) may be restated as

$$\rho^s \ddot{\tilde{\mathbf{u}}}^s = \rho^s \mathbf{f}^s + \alpha_1^s \nabla\nabla^2 \nu^s - [a_1^s - 2b_0^s \nu^s - \sum_{f=1}^{m} b_0^f \nu^f + 2\nu^s (b_0^s \nabla \cdot \tilde{\mathbf{u}}^s + \sum_{f=1}^{m} c_0^{sf} \nabla \cdot \tilde{\mathbf{u}}^f) + G^s \dot{\nu}^s] \nabla \nu^s$$
$$+ \sum_{f=1}^{m} b_0^f \nu^s \nabla \nu^f + \nu^s (\mu^s + \lambda^s + \sum_{f=1}^{m} f_0^f) \nabla\nabla \cdot \tilde{\mathbf{u}}^s + \nu^s \mu^s \nabla^2 \tilde{\mathbf{u}}^s + \nu^s \sum_{f=1}^{m} (e_0^f + e_0^{sf}) \nabla\nabla \cdot \tilde{\mathbf{u}}^f$$
$$+ D(\dot{\tilde{\mathbf{u}}}^f - \dot{\tilde{\mathbf{u}}}^s) - \nu^s \nabla p - G^s \nu^s \nabla \dot{\nu}^s$$

(5-82)

$$\rho^f \ddot{\tilde{\mathbf{u}}}^{\mathbf{f}} = \rho^f f^f + \alpha_1^f \nabla\nabla^2 \nu^f - [a_1^f - 2c_0^f \nu^f - 2\frac{\nu^f}{1-\nu^s} c_0^{sf} \nu^s + G^f \dot{\nu}^f] \nabla \nu^f$$
$$+ (\frac{\nu^f}{1-\nu^s})^2 c_0^{sf} \nabla \nu^s + \nu^f [(d_0^f + \frac{\nu^f}{1-\nu^s} d_0^{sf}) \nabla\nabla \cdot \tilde{\mathbf{u}}^{\mathbf{f}}$$
$$+ (e_0^f + \frac{\nu^f}{1-\nu^s} e_0^{sf}) \nabla\nabla \cdot \tilde{\mathbf{u}}^{\mathbf{s}}] + (\mu^f + \lambda^f) \nabla\nabla \cdot \dot{\tilde{\mathbf{u}}}^{\mathbf{f}} + \mu^f \nabla^2 \dot{\tilde{\mathbf{u}}}^{\mathbf{f}} + \sum_{f'=1}^{m} D^{ff'} (\dot{\tilde{\mathbf{u}}}^{\mathbf{s}} - \dot{\tilde{\mathbf{u}}}^{\mathbf{f}'})$$
$$- \nu^f \nabla p - G^f \nu^f \nabla \dot{\nu}^f$$

(5-83)

where

$$\alpha_1^s = 2\alpha^s \nu^s, \quad a_1^s = 3a_o^s (\nu^s)^2 \tag{5-84}$$

$$\alpha_1^f = 2\alpha^f \nu^f, \quad a_1^f = 3a_o^f (\nu^f)^2 \tag{5-85}$$

Equations (5-82) and (5-83) are the generalized Biot's equations for multiphase flow through poro-elastic media.

The linearized form of continuity equations given by (5-4) and (5-5) become

$$\nabla \nu^s = -\nu^s \nabla\nabla \cdot \tilde{\mathbf{u}}^s \qquad \nabla \nu^f = -\nu^f \nabla\nabla \cdot \tilde{\mathbf{u}}^f \tag{5-86}$$

In the absence of net fluid flow, for a constant pressure field, using (5-86), the linearized form of the wave propagation for a poro-elastic media saturated with several fluid phases becomes

$$\rho^s \ddot{\tilde{u}}^s = \rho^s f^s + (\lambda_1^s + a_2^s \nu^s)\nabla\nabla.\tilde{u}^s - \alpha_1^s \nabla\nabla^2\nabla.\tilde{u}^s + \mu_1^s \nabla^2 \tilde{u}^s + \sum_{f=1}^{m} e_1^f \nabla\nabla.\tilde{u}^f \tag{5-87}$$

$$\rho^f \ddot{\tilde{\mathbf{u}}}^f = \rho^f \mathbf{f}^f + (a_2^f \nu^f + d_1^f)\nabla\nabla \cdot \tilde{\mathbf{u}}^f + (e_1^s - c_1^f \nu^s)\nabla\nabla \cdot \tilde{\mathbf{u}}^s - \alpha_1^f \nabla\nabla^2\nabla \cdot \tilde{\mathbf{u}}^f \tag{5-88}$$

where

$$a_2^s = a_1^s - 2b_0^s \nu^s - b_0^f \nu^f, \quad a_2^f = a_1^f - 2c_0^f \nu^f - \frac{2\nu^f}{1-\nu^s} c_0^{sf} \nu^f$$

$$c_1^f = \left(\frac{\nu^f}{1-\nu^s}\right)^2 c_0^{sf}, \quad d_1^f = \nu^f \left(d_0^f + \frac{\nu^f}{1-\nu^s} d_0^{sf}\right)$$

$$e_1^s = \nu^f \left(e_0^f + \frac{\nu^f}{1-\nu^s} e_0^{sf}\right), \quad e_1^f = \nu^s \sum_{f=1}^{m} (e_0^f + e_0^{sf})$$

$$\lambda_1^s = \nu^s (\mu^s + \lambda^s + f_0^s), \mu_1^s = \nu^s \mu^s \tag{5-89}$$

Here it is assumed $G^s = G^f = 0,$ and the damping effects are neglected. The higher order derivative terms given by $\nabla\nabla^2\nabla \cdot \tilde{\mathbf{u}}^s$ and $\nabla\nabla^2\nabla \cdot \tilde{\mathbf{u}}^f$ appear in Equations (5-87) and (5-88) due to the dependence of free energy functions on the gradient of phasic volume fractions.

Introducing the Helmhotz resolution of the displacement vectors

$$\mathbf{u}^s = \nabla\phi^s + \nabla \times \mathbf{A}^s, \quad \mathbf{u}^f = \nabla\phi^f \tag{5-90}$$

where ϕ and A are the scalar and vector potentials, Equations (5-87) and (5-88) may be restated as

$$\ddot{\phi}^s = C_D^s \nabla^2 \phi^s - \frac{\alpha_1^s}{\rho^s} \nabla^4 \phi^s + \sum_{f=1}^{m} \frac{e_1^f}{\rho^s} \nabla^2 \phi^f \tag{5-91}$$

$$\ddot{\mathbf{A}}^s = C_S^s \nabla^2 \mathbf{A}^s \tag{5-92}$$

$$\ddot{\phi}^f = C_D^f \nabla^2 \phi^f + \frac{(e_1^s - c_1^f \nu^s)}{\rho^f} \nabla^2 \phi^s - \frac{\alpha_1^f}{\rho^f} \nabla^4 \phi^f \tag{5-93}$$

where the body force is neglected and the speed of dilatational waves, C_D^s, C_D^f, and shear wave C_S^s are defined as

$$C_D^s = \frac{(\lambda_1^s + \mu_1^s + a_2^s \nu^s)}{\rho^s}, \qquad C_S^s = \frac{\mu_1^s}{\rho^s} \tag{5-94}$$

$$C_D^f = \frac{(a_2^f \nu^f + d_1^f)}{\rho^f} \tag{5-95}$$

Equations (5-91) - (5-93) are the wave propagation equations in a poro-elastic media saturated with several fluid phases. It is seen that the dilatational waves in the solid and the fluid bodies are coupled, while the shear wave in solid is not affected by the presence of the fluid phase. When there is only a single fluid phase present, these equations reduce to a generalized form of those developed by Biot (1956, 1957) for wave propagation in saturated porous media. The effect of microstructures of the media appears in Equations (5-91) and (5-93) through the terms $\nabla^4 \phi^s$ and $\nabla^4 \phi^f$, which have no counter parts in Biot's classical model.

In the absence of a fluid phase, Equations (5-91) and (5-92) govern the wave propagation in a dry poro-elastic media. Equation (5-91) shows that the dilatational waves are dispersed by the effect of porous medium microstructure, while the shear wave remain unchanged except for the variation in the magnitude of the wave speed by the effect of porosity.

Multiphase Flows through Porous Media

For the special case of multiphase flows through a rigid porous media, assuming

$$b_0^f = c_0^{sf} = d_0^{sf} = e_0^f = e_0^{sf} = 0 \tag{5-96}$$

Equations (5-5) and (5-81) may then be restated as

$$\frac{\partial \nu^f}{\partial t} + \nabla \cdot (\nu^f \tilde{\mathbf{v}}^f) = 0 \tag{5-97}$$

$$\begin{aligned} \rho_0^f \nu^f \frac{d\tilde{\mathbf{v}}^f}{dt} &= \rho_0^f \nu^f \mathbf{f}^f - \nu^f \nabla p + \alpha_1^f \nabla\nabla^2 \nu^f - \beta_1^f \nabla \nu^f + \mu^f \nabla^2 \tilde{\mathbf{v}}^f \\ &+ (\lambda^f + \mu^f)\nabla\nabla \cdot \tilde{\mathbf{v}}^f - \sum_{f'=1}^{m} \mathbf{D}^{ff'} \cdot \tilde{\mathbf{v}}^{f'} - G^f \nu^f \nabla \dot{\nu}^f \end{aligned} \tag{5-98}$$

where

$$\beta_1^f = \nu^f (3a_0^f \nu^f - 2c_0^f) + G^f \dot{\nu}^f \tag{5-99}$$

Equations (5-97) and (5-98) are the generalized form of Brinkman's equations for multiphase flows through porous media.

Generalized Darcy's Law

For a steady motion and when the spatial variations of fluid velocities are small, Equation (5-98) reduces to

$$D^{ff} \cdot \tilde{\mathbf{v}}^{f'} = \rho_0^f \nu^f f^f - \nu^f \nabla p + \alpha_1^f \nabla\nabla^2 \nu^f - \beta_1^f \nabla \nu^f \nu^f - G^f \nu^f \nabla \dot{\nu}^f \tag{5-100}$$

Equation (5-100) is the generalized Darcy's law for multiphase flows through porous media.

For the case of two-phase flows in porous media, the explicit form of the governing equations are given as

$$D^{11}\tilde{\mathbf{v}}^1 + D^{12}\tilde{\mathbf{v}}^2 = \rho_0^1 \nu^1 \mathbf{f}^1 - \nu^1 \nabla p + \alpha_1^1 \nabla\nabla^2 \nu^1 - \beta_1^1 \nabla \nu^1 - G^1 \nu^1 \nabla \dot{\nu}^1 \tag{5-101}$$

$$D^{21}\tilde{\mathbf{v}}^1 + D^{22}\tilde{\mathbf{v}}^2 = \rho_0^2 \nu^2 \mathbf{f}^2 - \nu^2 \nabla p + \alpha_1^2 \nabla\nabla^2 \nu^2 - \beta_1^2 \nabla \nu^2 - G^2 \nu^2 \nabla \dot{\nu}^2 \tag{5-102}$$

Noting that

$$\nu^1 = s(1-\nu^s), \quad \nu^2 = (1-s)(1-\nu^s) \tag{5-103}$$

where $(1-\nu^s)$ is the porosity and s is the saturation of phase 1, Equations (5-101) and (5-102) may be restated as

$$D^{11}\tilde{\mathbf{v}}^1 + D^{12}\tilde{\mathbf{v}}^2 = (1-\nu^s)s[\rho_0^1\mathbf{f}^1 - \nabla p + \alpha_o^1\nabla\nabla^2 s - \beta_o^1\nabla s - G_0^1\nabla\dot{s}] \tag{5-104}$$

$$D^{21}\tilde{\mathbf{v}}^1 + D^{22}\tilde{\mathbf{v}}^2 = (1-\nu^s)(1-s)[\rho_0^2\mathbf{f}^1 - \nabla p - \alpha_o^2\nabla\nabla^2 s + \beta_o^2\nabla s^f + G_0^2\nabla\dot{s}] \tag{5-105}$$

where the coefficients are

$$\alpha_0^1 = \frac{\alpha_1^1}{s}, \quad \beta_0^1 = \frac{\beta_1^1}{s}, \; G_0^1 = G^1(1-\nu^s)$$
$$\alpha_0^2 = \frac{\alpha_1^2}{(1-s)}, \quad \beta_0^2 = \frac{\beta_1^2}{(1-s)}, \; G_0^2 = G^2(1-\nu^s) \tag{5-106}$$

Equations (5-104) and (5-105) show that the spatial variations of saturation and time rate of change of saturation affects the phasic velocity field. In addition, the phases exert drag on one another. When $\nabla\nabla^2 s$ in Equations (5-104) and (5-105) are neglected, they resemble those proposed by Hasanizadeh and Gray (1993).

When the material parameters given in (5-106) are constants, Equations (5-104) and (5-105) may be restated as

$$D^{11}\tilde{\mathbf{v}}^1 + D^{12}\tilde{\mathbf{v}}^2 = (1-\nu^s)s[\rho_0^1\mathbf{f}^1 - \nabla p^1] \tag{5-107}$$

$$D^{21}\tilde{\mathbf{v}}^1 + D^{22}\tilde{\mathbf{v}}^2 = (1-\nu^s)(1-s)[\rho_0^2\mathbf{f}^2 - \nabla p^2] \tag{5-108}$$

Here the effective pressures, p^1 and p^2, are defined as

$$p^1 = p - \alpha_0^1\nabla^2 s + \beta_0^1 s + G_0^1\dot{s} \tag{5-109}$$

$$p^2 = p + \alpha_0^2\nabla^2 s - \beta_0^2 s - G_0^2\dot{s} \tag{5-110}$$

The effective capillary pressure, p_c, may then be defined as

$$p_c = p^1 - p^2 = -(\alpha_0^1 + \alpha_0^2)\nabla^2 s + (\beta_0^1 + \beta_0^2)s + (G_0^1 + G_0^2)\dot{s} \tag{5-111}$$

That is, the phases will experience an effective pressure difference, which is a function of

saturation and its spatial and time derivatives. Equation (5-111) in the absence of the spatial derivative term reduces to that proposed by Beliaev and Hassanizadeh (2001). Beliaev and Hasssanizadeh have shown that (5-111) is capable of accounting for the hysteresis and dynamic effects in two-phase flows in porous media. Note that when both spatial and temporal variations of saturation are small, Equation (5-111) implies that the effective capillary pressure is a function of saturation, which is in agreement with the commonly assumed procedures, Scheidegger (1974).

The statement of conservation of mass given (5-97) in term of saturation becomes

$$\frac{\partial s}{\partial t} + \nabla \cdot (s\tilde{\mathbf{v}}^1) = 0 \tag{5-112}$$

$$\frac{\partial s}{\partial t} - \nabla \cdot [(1-s)\tilde{\mathbf{v}}^2) = 0 \tag{5-113}$$

Equations (5-107), (5-108), (5-112) and (5-113) form nine equations for finding $\mathbf{v}^1, \mathbf{v}^2, s$, p_1 and p_2.

For each of phases, Equations (5-107) and (5-108) may be solved and restated as

$$\tilde{v}_i^1 = K_{11}(\rho^1 f^1 - \nabla p^1) - K_{12}(\rho^2 f^2 - \nabla p^2) \tag{5-114}$$

$$\tilde{v}_i^2 = K_{22}(\rho^2 f^2 - \nabla p^2) - K_{21}(\rho^1 f^1 - \nabla p^1) \tag{5-115}$$

where

$$K_{11} = \frac{sD^{22}}{D^{11}D^{22} - D^{12}D^{21}}(1-\nu^s) \quad , \quad K_{12} = \frac{(1-s)D^{12}}{D^{11}D^{22} - D^{12}D^{21}}(1-\nu^s) \tag{5-116}$$

$$K_{22} = -\frac{(1-s)D^{11}}{D^{11}D^{22} - D^{12}D^{21}}(1-\nu^s) \quad , \quad K_{22} = -\frac{sD^{21}}{D^{11}D^{22} - D^{12}D^{21}}(1-\nu^s) \tag{5-117}$$

For a single-phase flow through porous media, Equation (5-115) reduces to the Darcy law.

Conclusions

A continuum model for multiphase flows through poro-elastic media is developed. Based

on the thermodynamics of the multiphase mixture flows, appropriate constitutive equations are formulated. The new model included the effects of phasic interaction and the elastic deformation of the media. The special case of wave propagation in poro-elastic media saturated with multiphase fluids is examined. It is shown that the nature of the shear waves is not affected by the presence of the pores saturated with the multiple fluids. The dilatational waves, however, is further dispersed by the microstructure effects of the media. It is also shown that the present theory contains, as its special cases, Biot's theory of poro-elastic media.

The special case of multiphase flows in rigid porous media is treated in detail. It is shown that the model reduces to a generalized form of Darcy's law that includes the effects of phasic drag. In addition, the model naturally leads to an effective capillary pressure that is a function of saturation, and its spatial and temporal derivatives. As a result the model should be capable of accounting for the hysteresis and dynamic effects observed during drainage and imbibitions.

6. TWO-PHASE LIQUID-GAS FLOWS IN FRACTURED MEDIA

We have performed a series of analysis of gas-liquid flows in fractured media with application to the flow process during hydrate dissociation. After the hydrate dissociates, it is expected that the flow of natural gas and water (and possibly solid phases) will be channeled into fractures of the reservoir rather than homogenous matrix. To gain an understanding of the flow process, several simulations were performed and the results are described in this section.

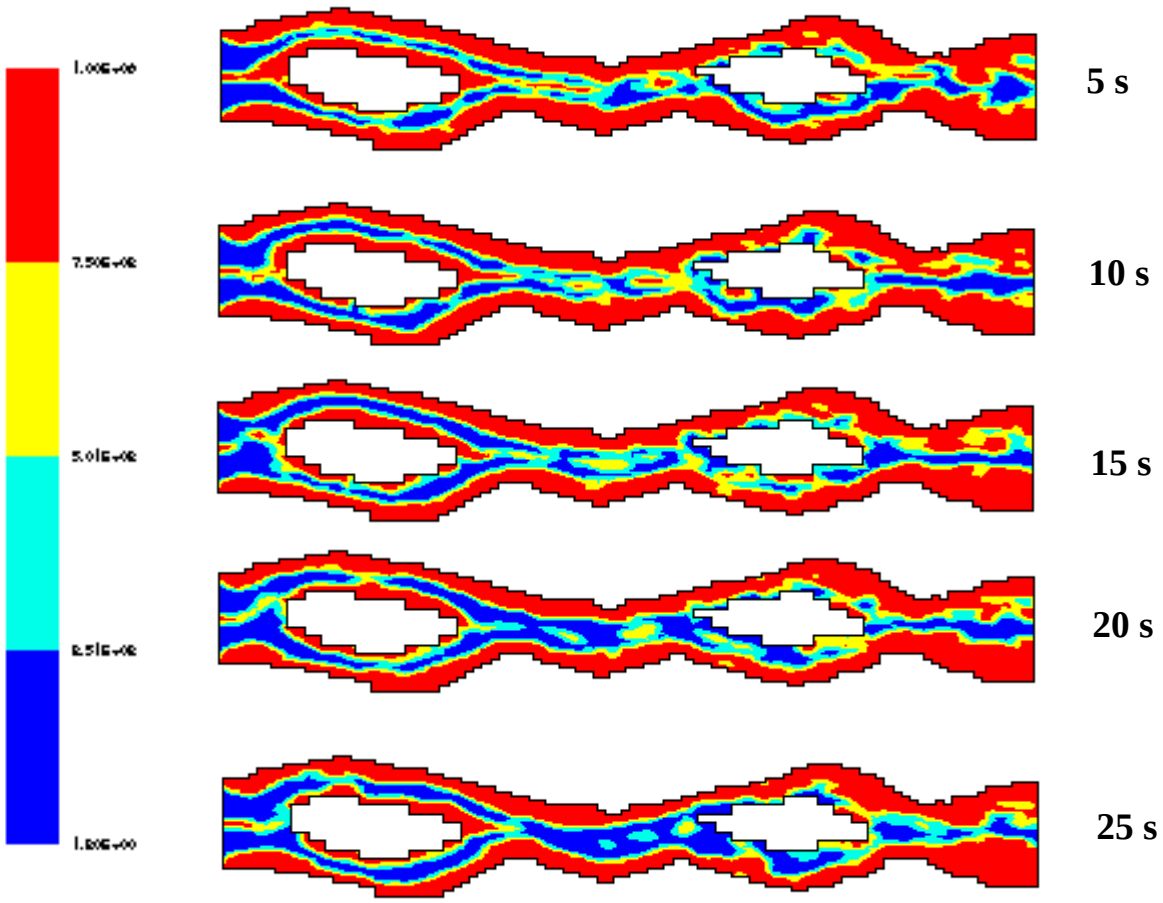

Figure 30. Variations of density for a gas-liquid flow in a fracture.

Gas-liquid mixture flows in a fracture is simulated using a volume-of-fluid model. In this model the density in each computational cell is evaluated based the amount of gas and liquid present in the cell. As a result, the density variation accounts for the level of concentration of different phases. For a two-dimensional section of a fracture, Figure 23 shows a sequence of

simulation results for time evolution of density. It is seen that the density changes from the density of the gas to that of the liquid in certain regions. It also appears that the flow resembles an annulus flow with liquid covering the areas near the walls, while the gas flows in the central areas.

Figure 31 shows the details of the density variation in another model of fracture. Here the surface fracture is more smooth compare to the one shown in Figure 30. It is also assumed that fracture is originally water saturated. Natural gas generated by the hydrate dissociation moves as the invading fluid in the complex flow region in the fracture.

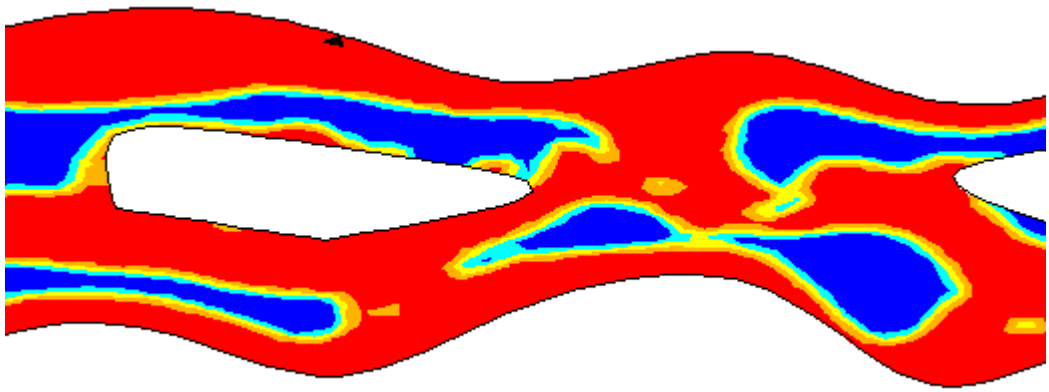

Figure 31. Details of density variation for a gas-liquid flow in a fracture model.

7. EXPERIMENTAL HYDRATE FORMATION AND DISSOCIATION IN UNCONSOLIDATED MEDIA

A series of experiments for providing quantitative data during hydrate formation and dissociation in unconsolidated sediment in the experimental setup were performed. In this section the experimental data for the time evolutions of pressure, temperature and propane mass flow rate during hydrate formation and dissociation are presented. Crushed ice and mixtures of crushed ice and glass bead were used as the media in this experimentation.

Experimental Setup

An experimental setup for studying propane hydrate formation and dissociation was fabricated. The setup was designed to provide for a visual inspection of hydrate formation and dissociation process in non-consolidated sediments. The setup consists of a transparent pressure vessel, data acquisition system, propane supply tank, pressure regulator, cold-water bath, circulating heat pump, and refrigeration unit. A schematic of the experimental setup is shown in Figure 32. Various component of the setup are described in this section.

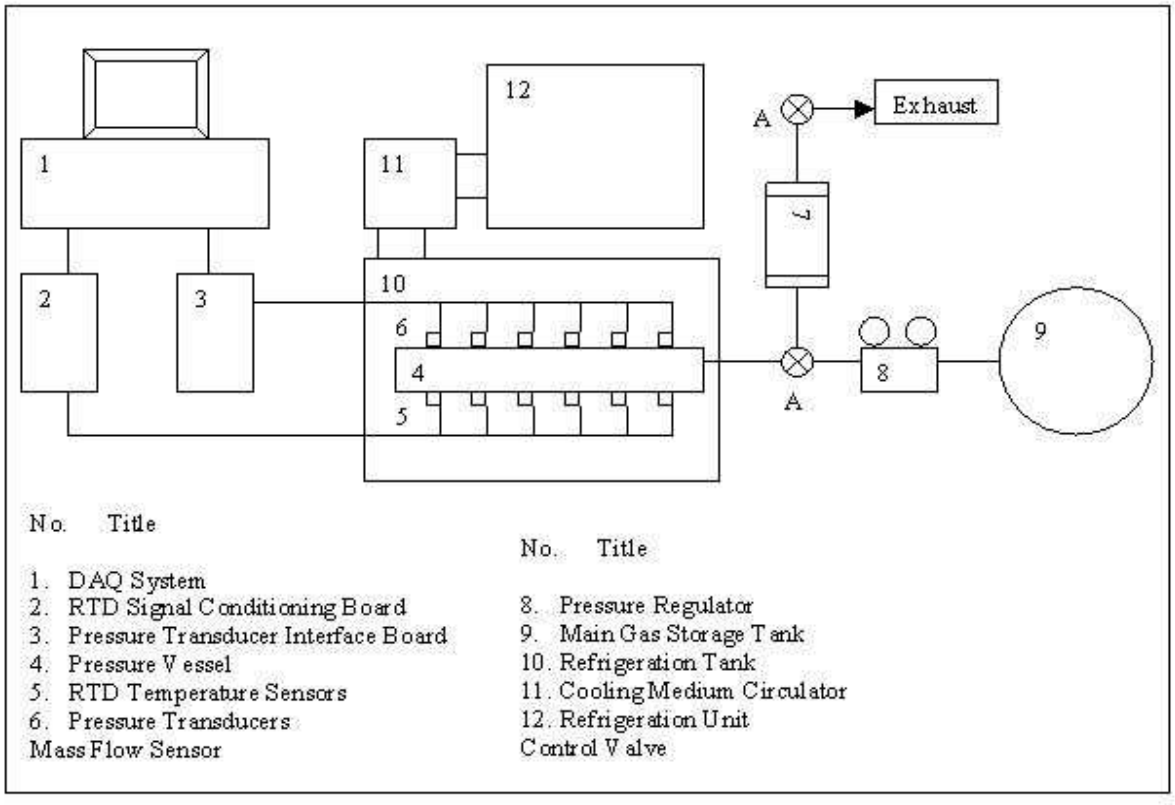

Figure 32. Schematic of the experimental setup.

The propane used for the experiments was chemically pure 99.95% propane. A pressure regulator on the tank outlet was used to maintain system pressure. From the tank and regulator, the propane enters the switching valve system, through a mass flow meter and into the pressure vessel. A switching valve system was incorporated so that the mass flow rate during formation and dissociation can be measured by the flow meter. A vacuum pump was also connected to the valve for evacuating the system before initiating the hydrate formation process. The outlet was routed to a fume hood to allow for exhausting the gas during the dissociation process.

From the valve system, the propane enters the pressure vessel through the inlet/outlet orifice. The pressure vessel is a billet 7075 aluminum unit with a Plexiglas top and bottom to allow for visual inspection of the sample during propane hydrate formation and dissociation. The vessel has internal dimensions of $25.5 \times 7.8 \times 6.5 = 1{,}293\ \text{cm}^3$. The top and bottom surface are constructed of 1.0 cm thick Plexiglas, which is reinforced with 0.4 cm thick aluminum trim rings. A 0.3 cm thick Buna-n (Nitrile) rubber gasket seals the Plexiglas to the aluminum body. Figure 33 shows a schematic of the components of the pressure vessel. A picture of the pressure vessel is shown in Figures 34 and 35.

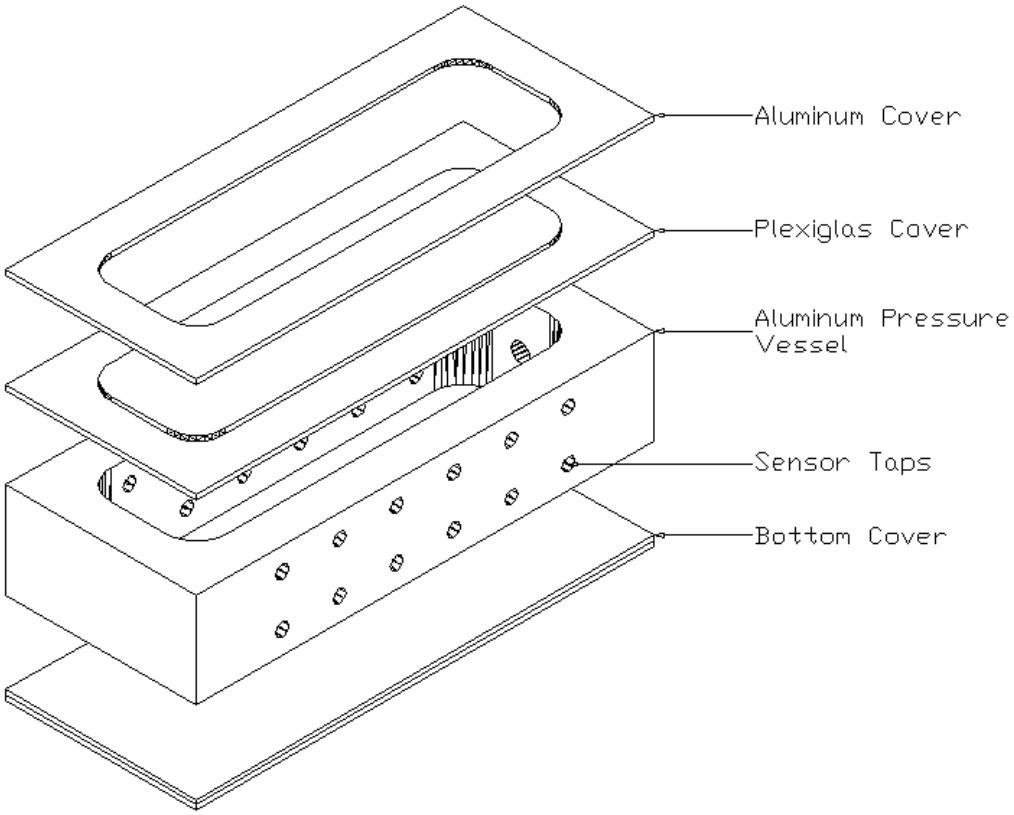

Figure 33. Schematic of the pressure vessel.

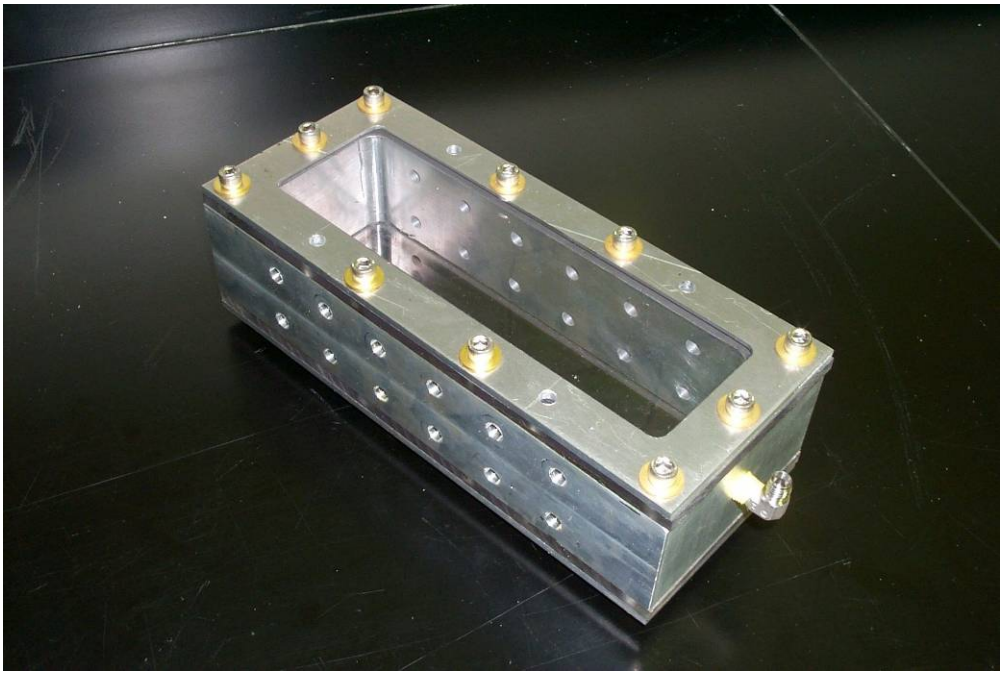

Figure 34. Fabricated hydrate pressure vessel.

Figure 35. Fabricated hydrate pressure vessel with the measuring sensors.

As shown in Figures 35 and 36, the vessel body houses six pressure sensors and six temperature sensors for monitoring the sample conditions at any time during the

experimentation. The pressure sensors are 0-60 psi gauge units (Druck PTX/PMP 1240) with an output from 1 to 5 volts. The pressure sensors are powered by an external, regulated power supply. Pressure taps allow the sensors to be remotely mounted, with pressure lines connecting the taps to the sensors. Swagelok© connectors are used throughout to ensure a leak free system. The temperature sensors are 3-wire, platinum, 100Ω RTD probes. The 3-wire RTD's alleviate the long lead wire resistances from affecting the signal reading. The tips of all sensors are located at the horizontal centerline of the vessel. All pressure and temperature sensors are connected to two National Instruments PCI-6023E DAQ boards, housed within an 800Mhz AMD© Duron computer system. The data acquisition system is controlled by a National Instruments LabView© code that has been developed. The code allows up to a sample rate of 1024 samples per second and can perform statistical evaluation of the data as needed. The data in the course of each experiment was recorded on a computer for compilation and analysis.

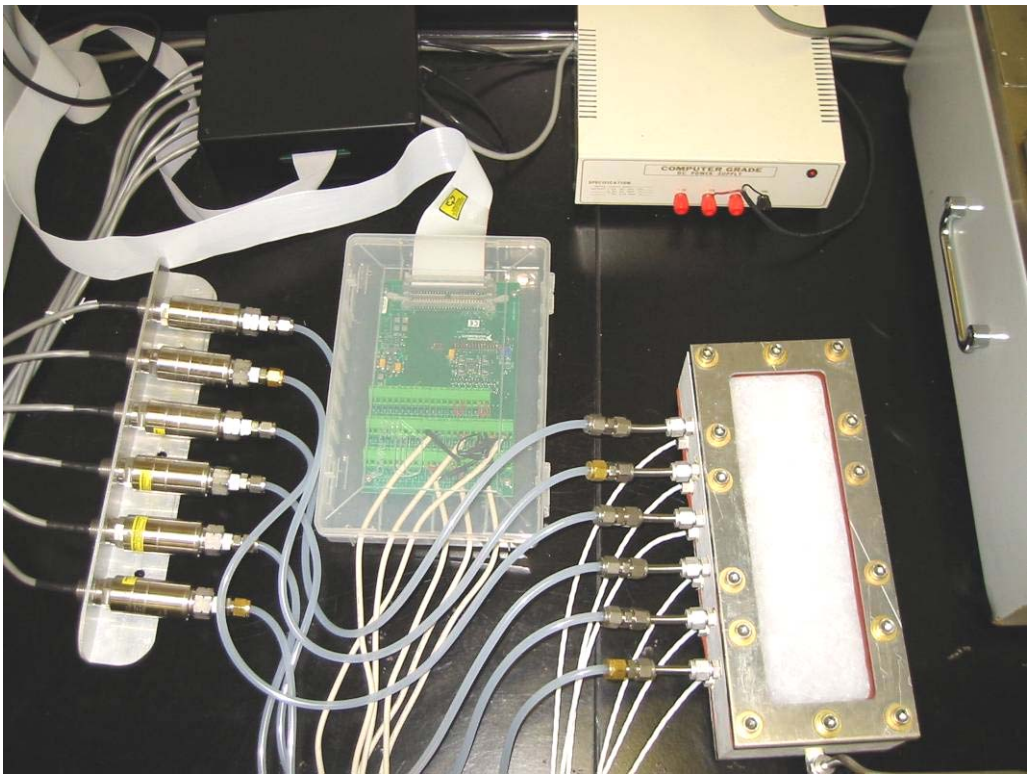

Figure 36. A picture of pressure and temperature sensors.

A mass flow meter recorded the amount of propane entering and exiting the pressure vessel. Since the mass flow meter can only read flow in one direction, a switching valve

system was incorporated into the system to allow for mass flow rate measurements. The mass flow meter had a range of 0 to 50 standard liters per minute (sLPM). The meter is also temperature compensated and is calibrated to the density of propane. A schematic of the switching valve system is shown in Figure 37.

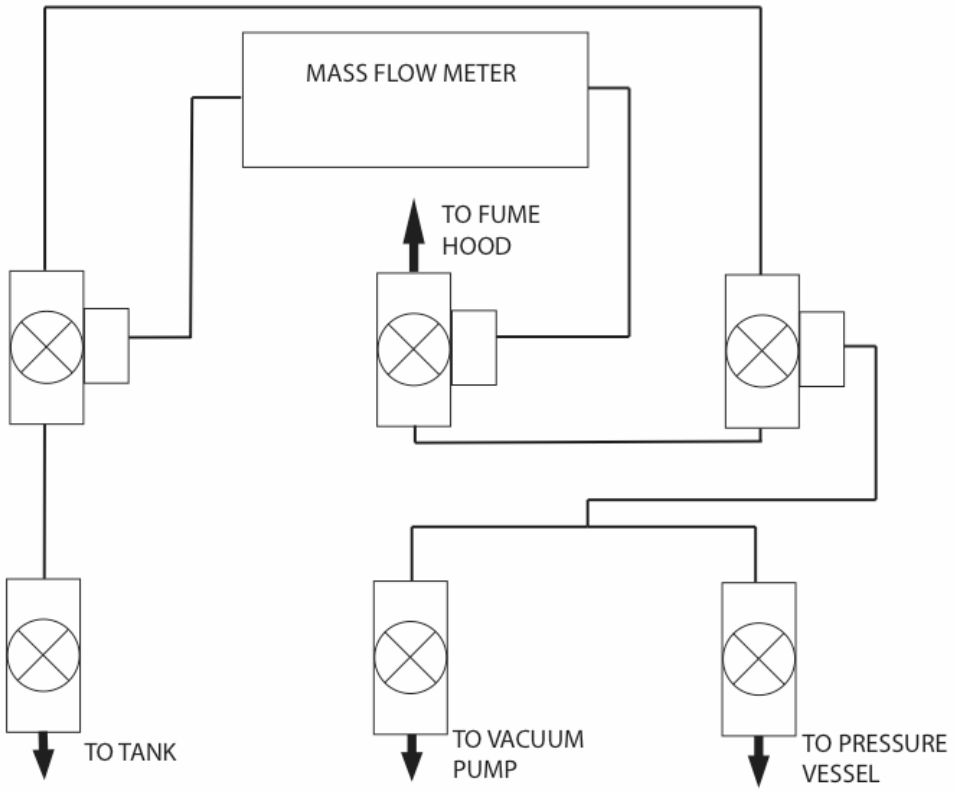

Figure 37. Schematic of valve switching system.

The pressure vessel and the attached sensors was submerged in a cold water/glycol bath and was kept at to -10ºC during the entire formation and dissociation experiment. The 50/50 mixture of water and glycol coolant is contained in a Lauda M30 bath, with a Lauda MS circulator/heater attached. The MS circulator/heater pumps the coolant through a Cole-Parmer chiller, and with the chiller/heater combination, a constant temperature is maintained at all times. The bath circulation ensures a constant bath temperature throughout the experiment. Pictures of the cooling bath system are shown in Figures 38 and 39.

Figure 38. A picture of constant temperature bath system.

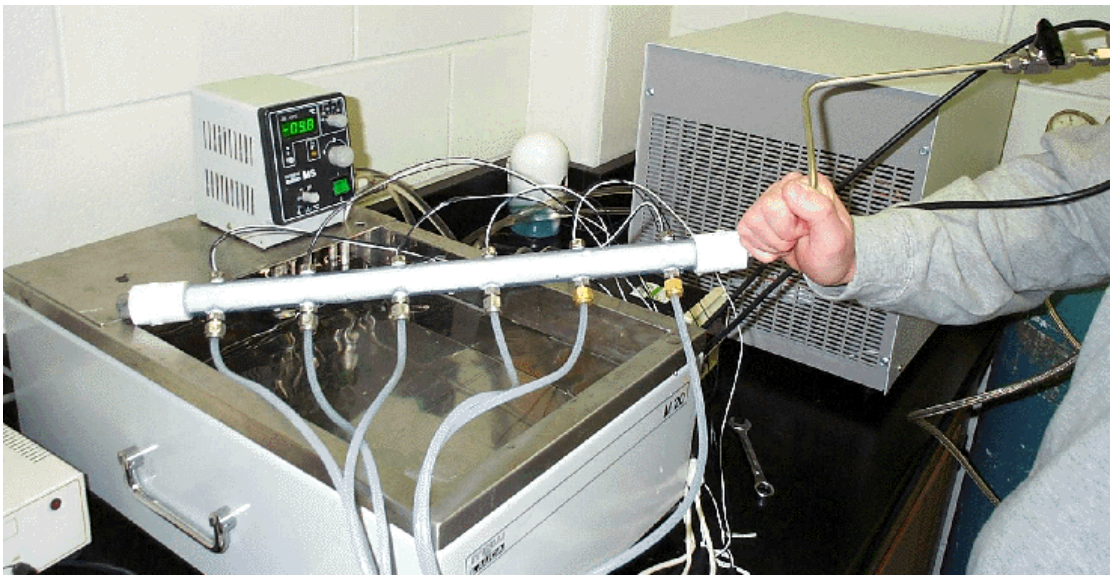

Figure 39. A picture of constant temperature with an earlier pressure vessel.

The following step-by-step procedure was used in the experimentation:

- Chill the bath to -10 ºC with circulator and chiller.

- Place vessel and hardware in -20 ºC environment.
- Shred ice and mix with glass beads as required.
- Place ice-glass beads mixture in -20 ºC environment.
- Pack uniformly the ice-glass beads mixture into the pressure vessel.
- Seal top to vessel and place in -10 ºC constant teperature bath.
- Start the data acquisition system.
- When media in the pressure vessel reaches to a constant temperature, evacuate air from system with the vacuum pump.
- Start propane injection at a constant pressure (40-50 psi).
- Record data as pressure falls during hydrate formation process.
- When pressure reaches to a roughly steady state, inject additional propane at constant pressure.
- When pressure decrease becomes negligible (normally after five days), assume that sufficient hydrate was formed and initiate the dissociation study by depressurization.
- When mass flow meter reading approaches zero, assume that the dissociation experiment is completed.

This procedure was followed for each experiment to ensure consistency.

Simplified Hydrate Formation and Dissociation Model

A simplified model for hydrate formation and dissociation in the pressure vessel is described in this section and is used for interpreting the experimental data. The statement of conservation of mass for propane in the pressure vessel during the hydrate formation or dissociation process is given as

$$\frac{d(\rho V)}{dt} = -k(p - p_{eq})^n + \dot{m} \qquad (7\text{-}1)$$

Here V is the available void space in the vessel, ρ is the mass density of the propane, p is propane pressure, p_{eq} is the propane hydrate equilibrium pressure, k and n are reaction rate constants, and $\dot{m}$ is the rate of mass of propane injected into the vessel during formation or rate exhausted during the hydrate dissociation. ($\dot{m}$ is considered positive for flow flow into the vessel.) The first term on the right hand side of Equation (7-1) is rate of production or dissociation of hydrate in the vessel. Here a simplified version of Kim-Bishnoi rate model is used. Equation (7-1) may be restated as

$$\frac{V}{RT}\frac{dp}{dt} = -k(p - p_{eq})^n + \dot{m} \qquad (7\text{-}2)$$

where a simple perfect gas law is assumed.

Hydrate Formation

At the initial stage when the propane is pumped into the vessel, neglecting the hydrate formation for the short time duration, Equation (7-2) reduces to

$$\frac{dp}{dt} = \frac{RT}{V}\dot{m} \tag{7-3}$$

Integrating (7-3), the pressure at the end of injection, p_1 in the vessel becomes

$$p_1 - p_o = \frac{RT}{V}\Delta m \tag{7-4}$$

where p_o is the initial pressure and T is the sample temperature which is assume to a constant equal to the bath temperature, and Δm is the total amount mass injected into the vessel. Equation (7-4) relates the change in the vessel pressure to the amount mass injected.

During the process of hydrate formation, neglecting the gas injection period, Equation (7-2) may be restated as

$$\frac{dp}{dt} = -k_1(p - p_{eq})^n, \quad k_1 = \frac{kRT}{V} \tag{7-5}$$

Integrating Equation (7-5), for $n \neq 1$, we find the time variation of the pressure in the vessel. That is,

$$\frac{1}{(p - p_{eq})^{n-1}} - \frac{1}{(p_1 - p_{eq})^{n-1}} = (n-1)k_1 t \tag{7-6}$$

where p_1 is the initial pressure after the vessel is pressurized. Similarly for $n = 1$, the expression for pressure becomes

$$\frac{p - p_{eq}}{p_1 - p_{eq}} = e^{-k_1 t} \tag{7-7}$$

Equations (7-6) and (7-7) show the decay of pressure in the vessel during propane hydrate formation. The rate of decay (value of k_1) may be found from the experimental data for different cycles and under different conditions.

Hydrate Dissociation

During the dissociation process, the vessel outlet is opened to the atmosphere. It is assumed that the mass flow rate leaving the vessel is proportional to the pressure difference and is given as

$$\dot{m} = -k_2 (p - p_{atm}) \tag{7-8}$$

Equation (7-2) may then be restated as

$$\frac{dp}{dt} = -\frac{RT}{V}(k + k_2)p + \frac{RT}{V}(kp_{eq} + k_2 p_{atm}) \tag{7-9}$$

Integrating Equation (7-9), the pressure variation during the dissociation is given as

$$p = p_o e^{-k_3 t} + \frac{A}{k_3}(1 - e^{-k_3 t}), \quad p_o = p\big|_{t=0} \tag{7-10}$$

where

$$k_3 = \frac{RT}{V}(k + k_2), \quad A = \frac{RT}{V}(kp_{eq} + k_2 p_{atm}) \tag{7-11}$$

and p_o is the initial vessel pressure just before the dissociation by depressurization begin. Equations (7-10) and (7-11) give the expression for the pressure in the vessel during the propane hydrate dissociation process.

For large time, Equation (7-10) leads to

$$p = \frac{A}{k_3} = \frac{kp_{eq} + k_2 p_{atm}}{k + k_2} \tag{7-12}$$

When all the hydrated in the vessel is depleted, neglecting the term involving the rate of dissociation (i.e., k=0), and the pressure approaches atmospheric condition.

Hydrate Formation Results

A series of experiments were performed for obtaining details of variation of pressure, temperature and mass flow rate data during the formation and dissociation of propane hydrate

in porous media composed of crushed ice, and mixtures of crushed ice and glass beads. The pure crushed ice was used for basic understanding and as a base line. The cases that the mixture contained 25% and 50% glass beads were also studied. The percentage of glass beads to ice were on volumetric basis in these experiments. The glass beads-crushed ice mixtures were used to simulate the natural in-situ hydrate formation and dissociation in the unconsolidated sediments. Glass beads were selected to represent sands in geological formation but with a known particle size, distribution and shape. Having a known particle size and shape is expected to facilitate the interpretation of the data and is important to the model development for hydrate formation and dissociation in geological reservoirs. The crushed ice particles that were generated by shaving ice cubes tent to be flakes of about 2mm wide. The corresponding equivalent diameter sphere radius was 0.45mm.

As described earlier, the top and bottom walls of the pressure vessel were constructed of Plexiglas, which allowed the visual inspection of the hydrate formation and dissociation process. This provided an additional tool for physical interpretation of the experimental data. In addition, any formation irregularities or dissociation patterns could have been visually apparent through the transparent vessel walls.

The computer data acquisition system, described in Experimental Setup section, ensured the reproducibility of the data collection procedure. The duration of an experiment was approximately six days, which would vary somewhat depending on the requirements of the particular experiment. The first five days were typically necessary for hydrate formation, while a 24-hour period was required for the hydrate to dissociate to a point where the gas output dropped to below measurable levels.

The data collected for pressure, temperature and mass flow rate variations, during formation and dissociation phase are described separately in the following sections.

Propane Hydrate Formation in Pure Crushed Ice

The experiments with crushed ice were performed as a baseline study and for providing a fundamental understanding of the process of formation in bulk hydrate systems. Figure 40 shows a representative pressure time evolution for one experiment encompassing the entire formation and dissociation period. As noted before, there were six sensors in the vessel that were arranged at a distance of 5 cm apart with sensor 1 being closest to the inlet/outlet and sensor 6 being the furthest.

Figure 40 shows are all the components of the hydrate formation and dissociation cycle. As outlined in the section on experimental procedure, the hydrate formation in the experimental pressure vessel required several steps. At the time initial time, when the

vacuum pump is connected to the pressure vessel, the pressure drops to –13.5 psig. Then the regulator on the propane tank opens, which raises the pressure sharply to about 50 psi. In the first few hours at the start of the experiment, pressure regulator is opened several times in order to maintain the vessel pressure above the equilibrium hydrate formation pressure.

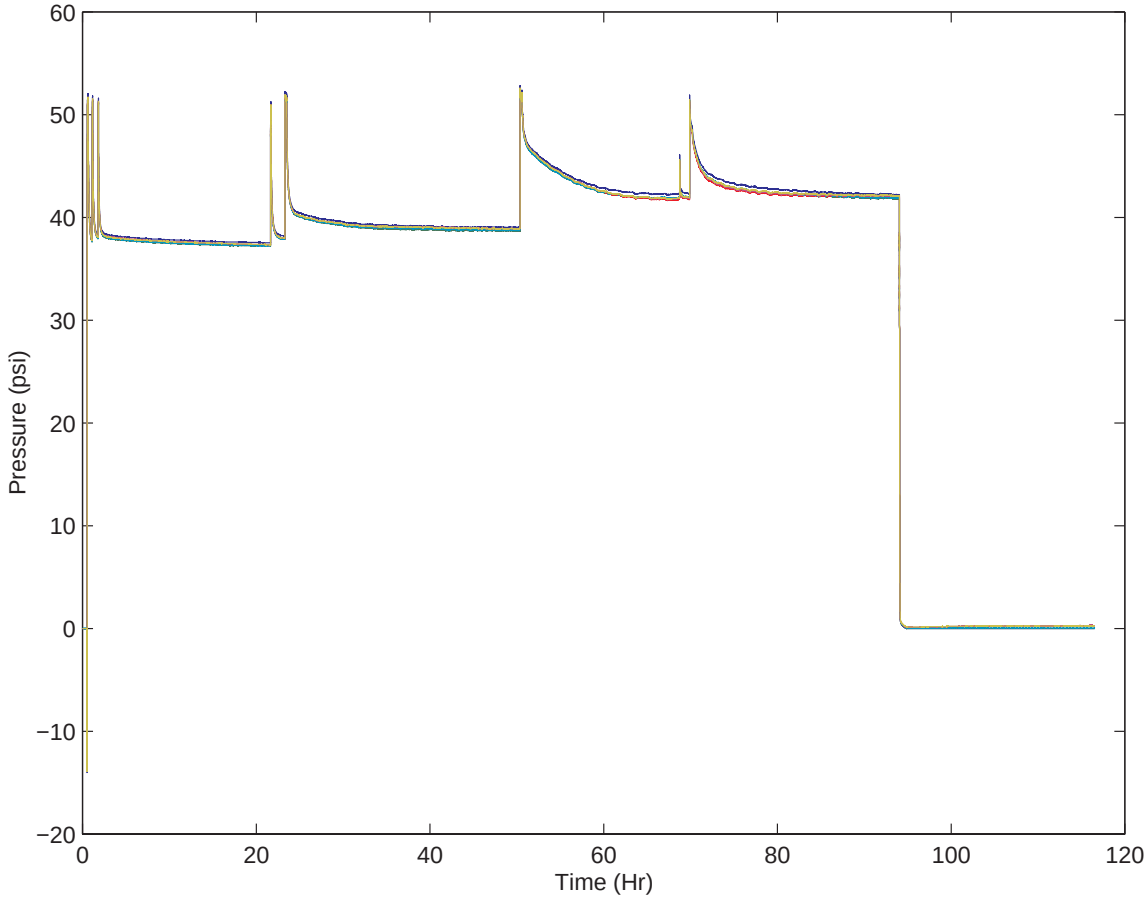

Figure 40. Time evolution of gauge pressure for hydrate formation and dissociation in crushed ice.

Every time after pressurization of the vessel, the pressure decays roughly exponentially approaching the equilibrium pressure. The hydrate formation process decreases as the equilibrium pressure approached. The bath temperature was kept constant at -10 ºC in these experiments. Figure 40 shows that as the hydrate forms, decreasing the available surface of crushed ice particles present in the vessel, the time required to approach the equilibrium condition increases with each pressurization cycle. The equilibrium pressure also increases gradually after every cycle. These behaviors are particularly evident for cycles after 40 hours. After 95 hours, the process of propane hydrates formation is considered to be

roughly complete for the dissociation test to be initiated. The outlet of the vessel is then opened to atmospheric condition to allow hydrate dissociation by the depressurization mechanism.

Details of the pressure variations during the hydrate formation process can be better seen from Figure 41 with the adjusted scale. It is seen that the rapid increase in pressure, follows by a roughly exponential decrease, which is also changing as the number of pressure cycles increases. The time required to approach the equilibrium pressure also increases with each cycle.

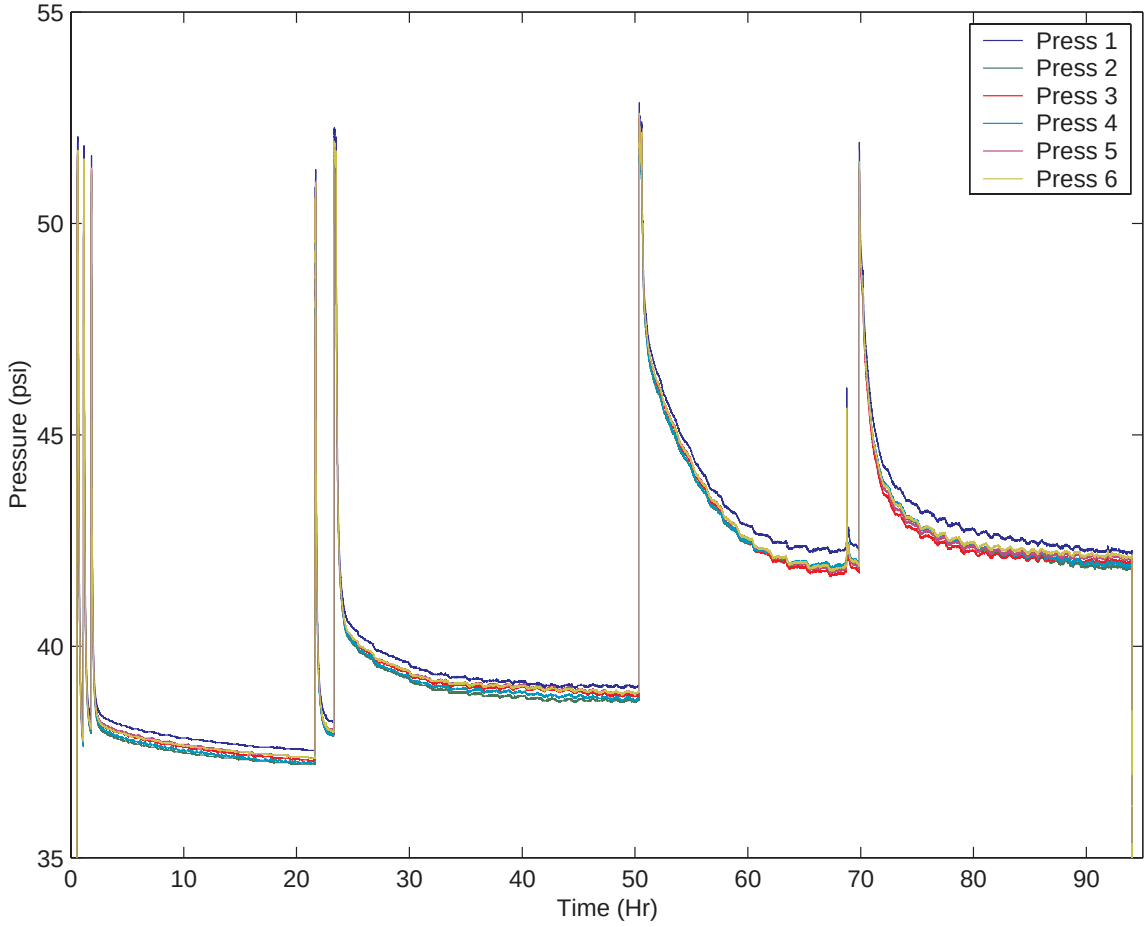

Figure 41. Time evolution of gauge pressure for hydrate formation in crushed ice.

The details of the pressure variation during propane hydrate formation process are shown in Figure 42. This figure shows after the first propane injection, the system pressure approaches the equilibrium pressure in about half an hour and the process of hydrate formation will slow down until the regulator valve is opened up and the pressure is again increased. During the initial stages of propane hydrate formation in crushed ice, the rate at which the pressure approaches equilibrium remains roughly the same. As time increases, however, the time to equilibrium increases also the pressure approaches a larger equilibrium

value, as indicated by Figures 40 and 41. The equilibrium pressure is initially about 38 psi, while after 90 hours it approaches 43 psi. That is a 5 psi increase in equilibrium pressure, while the bath temperature is kept constant at -10 ºC.

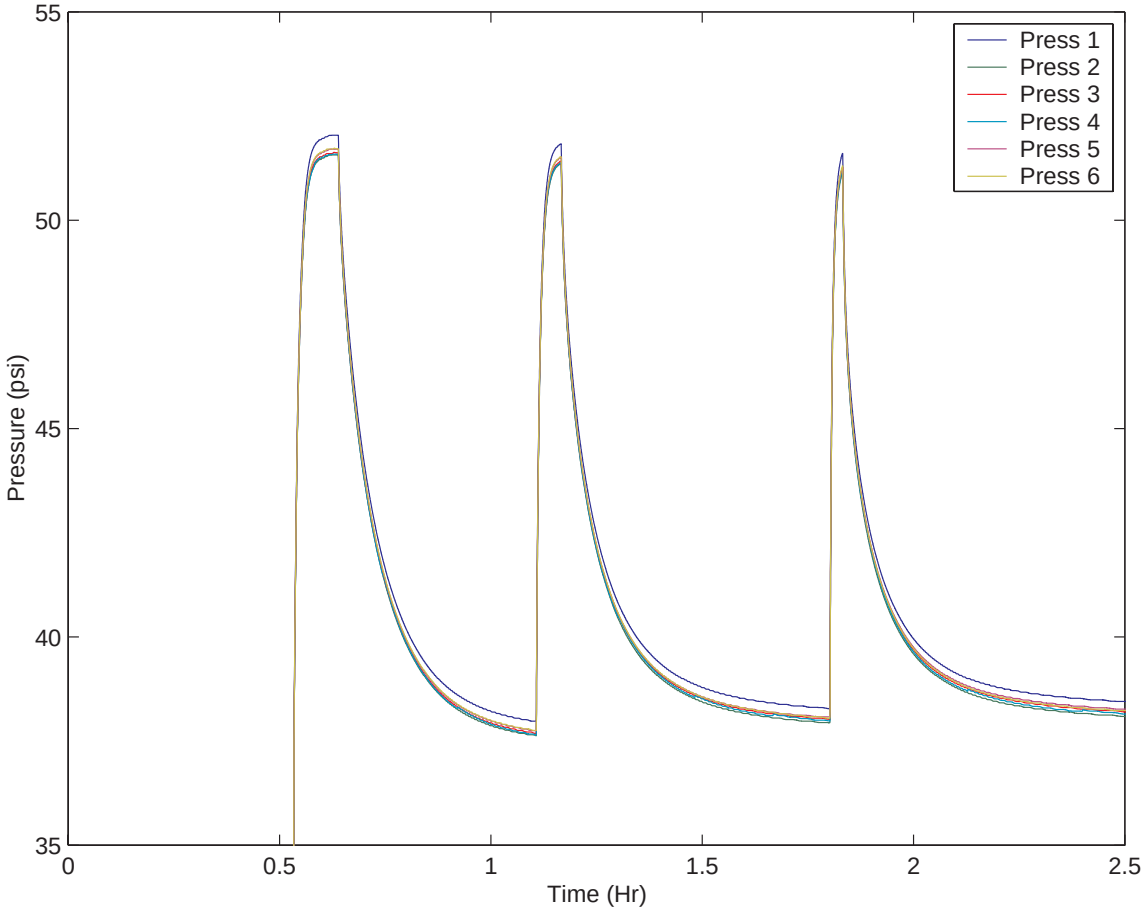

Figure 42. Details of pressure variations in the earlier stages during formation of propane hydrate in crushed ice.

The fitting of the exponential decay as given by Equation (**7-7**) to the decay of the first and third pressurization cycle are shown in Figure 43. Here the average of the six pressure sensors is used for the fitting. The corresponding k-values are also determined and is shown in this figure.

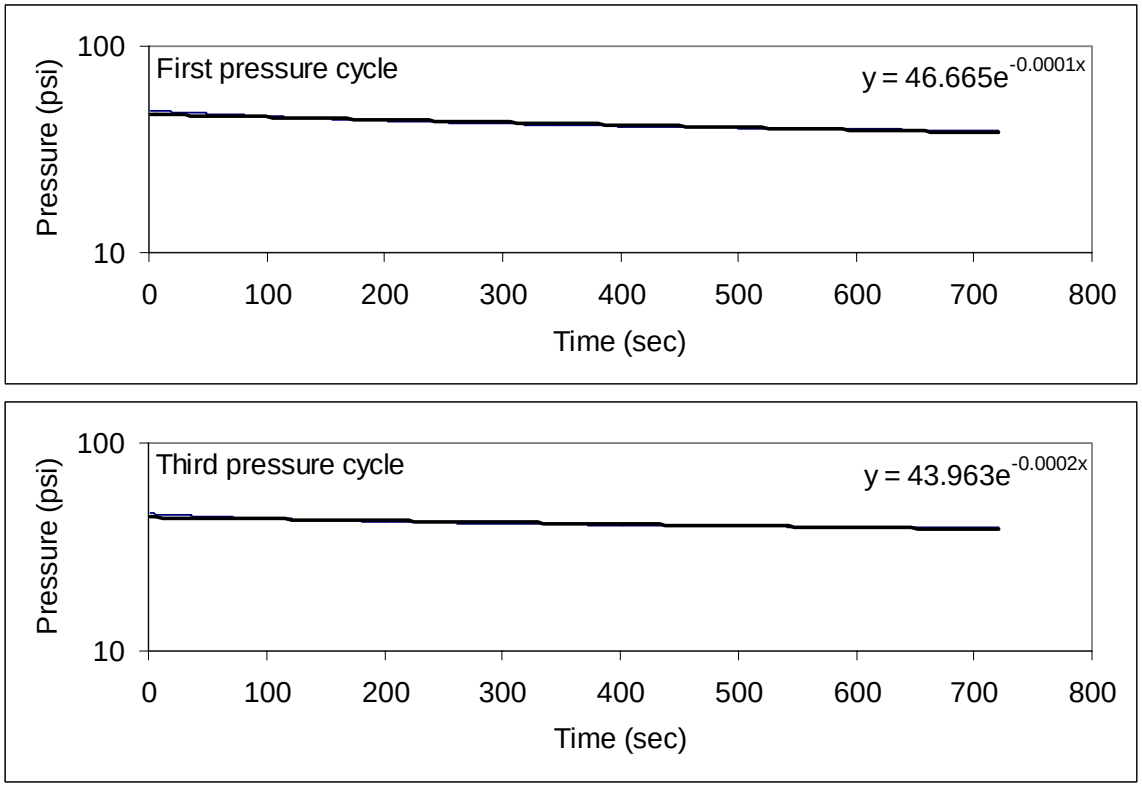

Figure 43. Exponential fit to pressure decay during hydrate formation in cycle 3 in crushed ice.

The details of the fifth pressure cycle are shown in Figure 44. It is seen that the pressure readings of sensor 1, which is closed to the inlet, is the highest. The reading of the other sensors, however, do not show is specific trend. This in part is due to accuracy of the pressure sensors. The exponential fit to the data is shown in Figure 45. The corresponding k-value for this pressure cycle is 0.0002, which is the same as the k-value for the third cycle.

As noted in the section on the experimental setup, six pressure and temperature sensors, distributed spatially along the vessel, record the time evolution of pressure and temperature. This allows for the detection of any spatial variation of pressure and temperature in the vessel during the hydrate formation. Enlarged segments of the pressure distribution for the fifth cycle and at latter stages of hydrate formation are shown in Figures 46 and 47. These figures exhibit a pressure distribution along the length of the vessel with a distinguishable pattern. Pressure sensor 1 shows the highest reading in both figures, the remaining sensor readings, however, do not show a specific trend. However, the trend is the same in both figures.

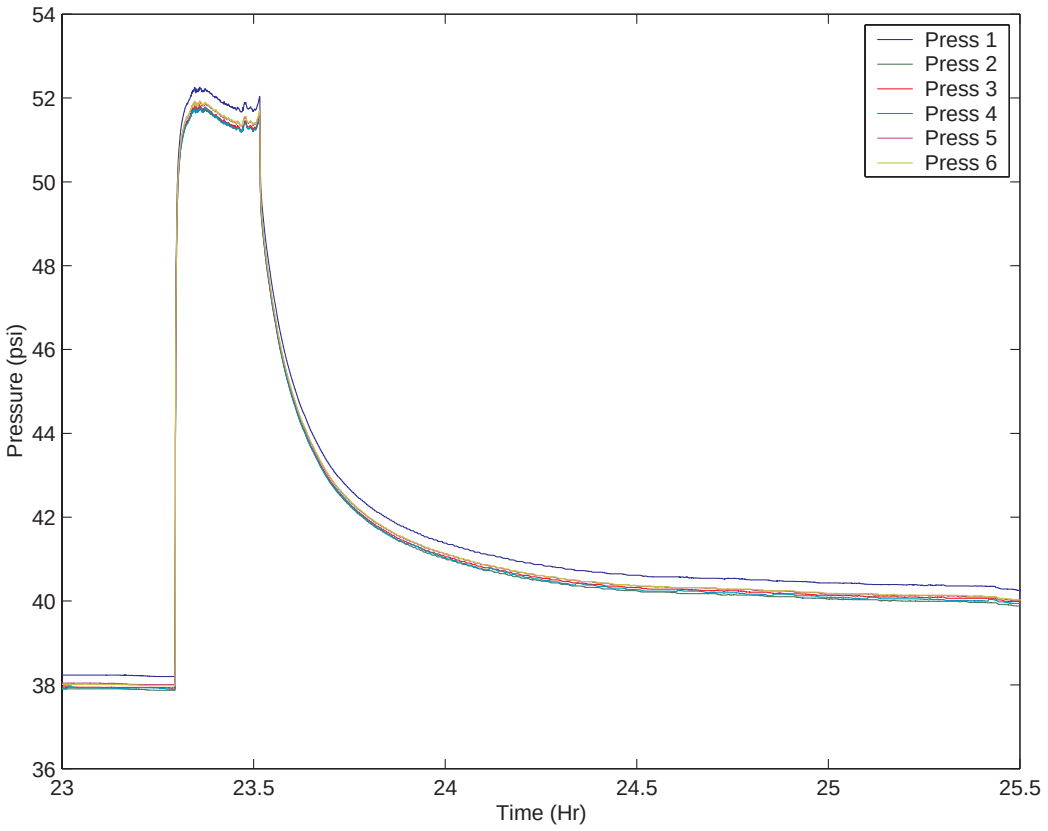

Figure 44. Details of pressure variation during the fifth pressure cycle for hydrate formation in pure crushed ice.

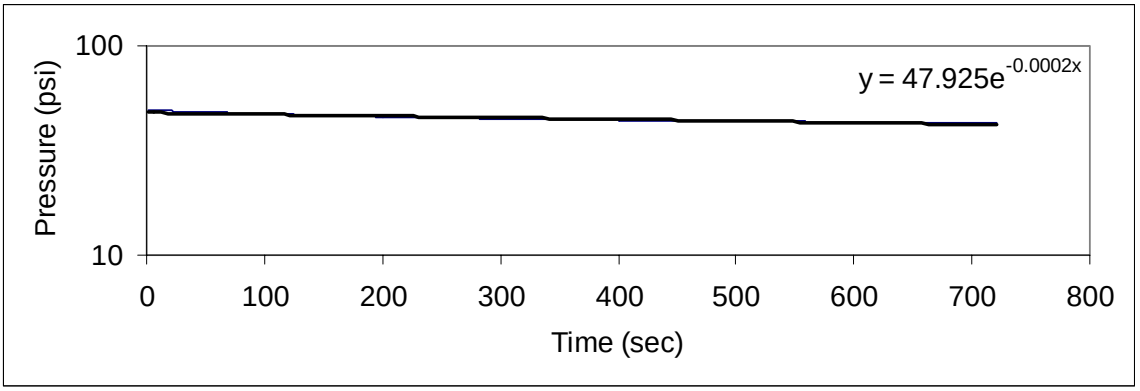

Figure 45. Exponential fit to pressure decay during hydrate formation in cycle 5 in crushed ice.

The reason for the seemingly irregular order of the sensors 2-6 reading is not

obvious. It should be emphasized that the accuracy of the pressure transducers used in these experiments is $\pm 0.25\%$, which results in a pressure error of ± 0.1. The differences in the pressure readings in Figures 46 and 47 are about 0.4 psi. Therefore, part of the observed deviations may be attributed to the error in pressure sensor readings. Nevertheless the persistence of these patterns in both figures suggests that the sample may have formed fractures that generates low pressure drop passages that allow the gas to reach areas near sensors in the back of sample more readily.

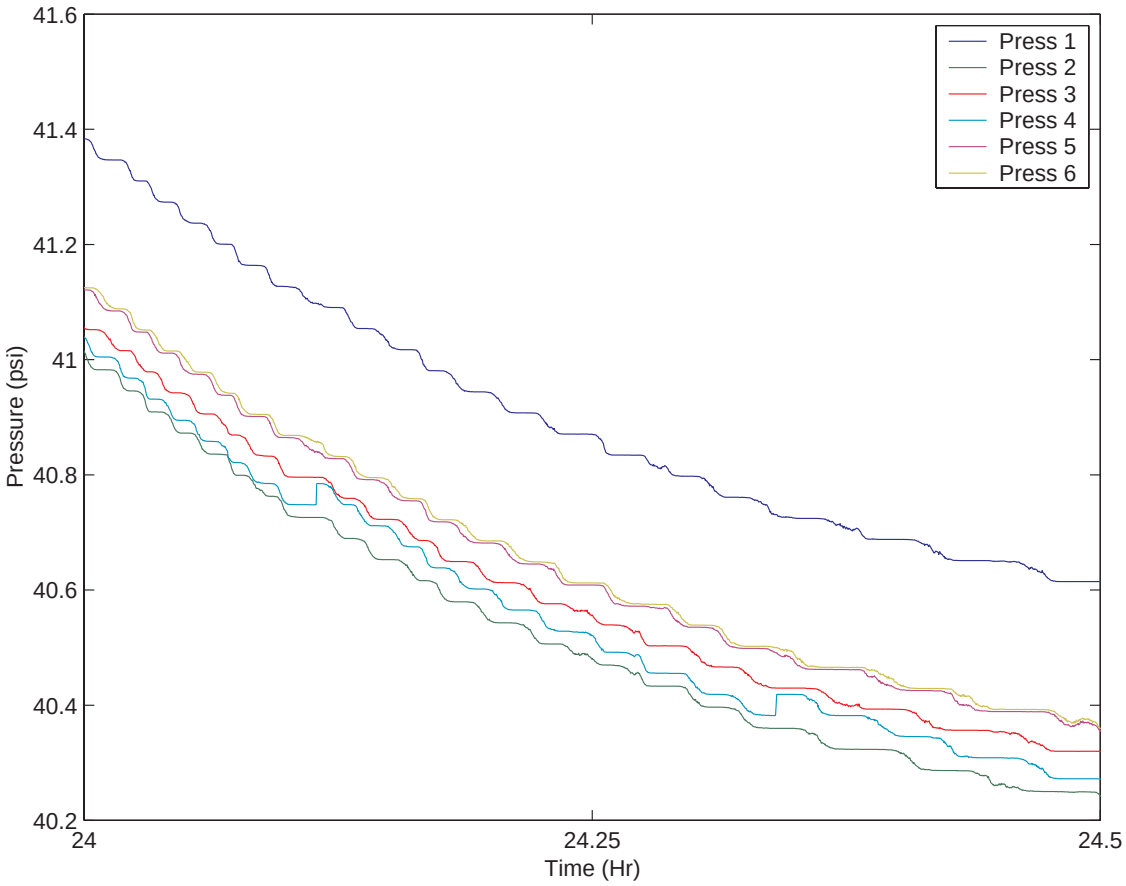

Figure 46. Spatial and temporal variations of pressure in the vessel during the fifth cycle of hydrate formation in crushed ice.

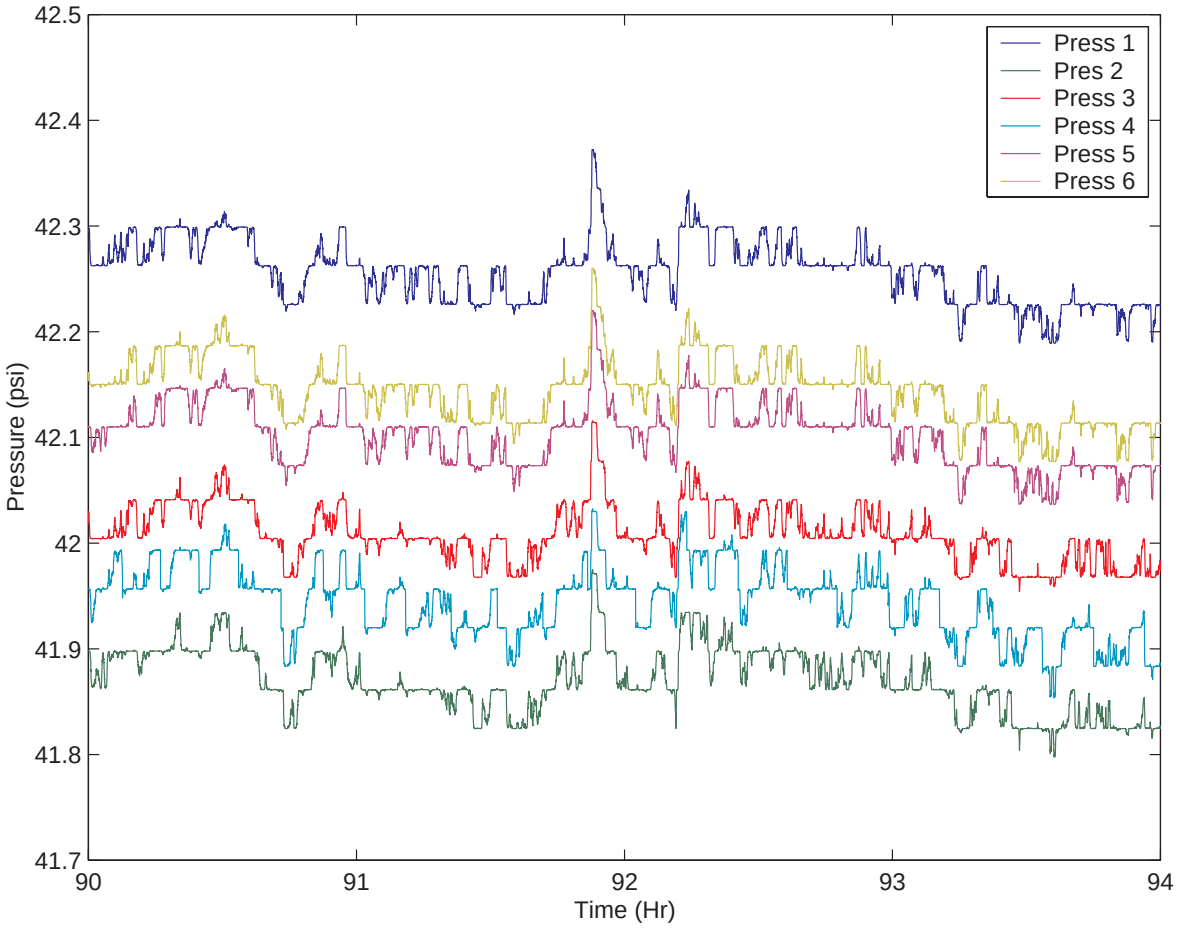

Figure 47. Spatial and temporal variations of pressure in the vessel during the latter stages of hydrate formation in crushed ice.

The time variation of temperature during the propane hydrate formation in the crushed ice is shown in Figure 48. As the propane is injected from the tank into the system, the temperature rises as the gas pressure increases. The temperature then decreases gradually with time. The increase in temperature is partially attributed to the propane gas injected into the vessel from the tank. The propane gas in the tank is at room temperature and when injected into the vessel leads to an increased temperature reading by the sensors. The increase of temperature at the earlier stages of hydrate formation is about 8ºC. At the latter stages of hydrate formation, however, the increase in temperature reduces significantly. This is because the amount of propane that enters the vessel decreases, due to the decrease in available pore volumes for hydrate production.

Figure 49 shows the time histories of temperature at different locations of the vessel during the initial stages of propane hydrate formation process. It is seen that the sharp increase in temperature follows by a gradual roughly exponential decrease. Also

interestingly, spatial variations of temperatures measured by the sensors show a decreasing variation with the distance from the inlet pipe. That is, the temperature is highest at sensor 1 which is closest to the inlet, and decreases with the distance of the sensor from the inlet. There is some discrepancy with temperatures at sensors 5 and 6 in second and third cycles, which may be caused by the non-uniformity in the propane hydrate formation in the pressure vessel. It should also be emphasize that the accuracy of the temperature sensors is rather high.

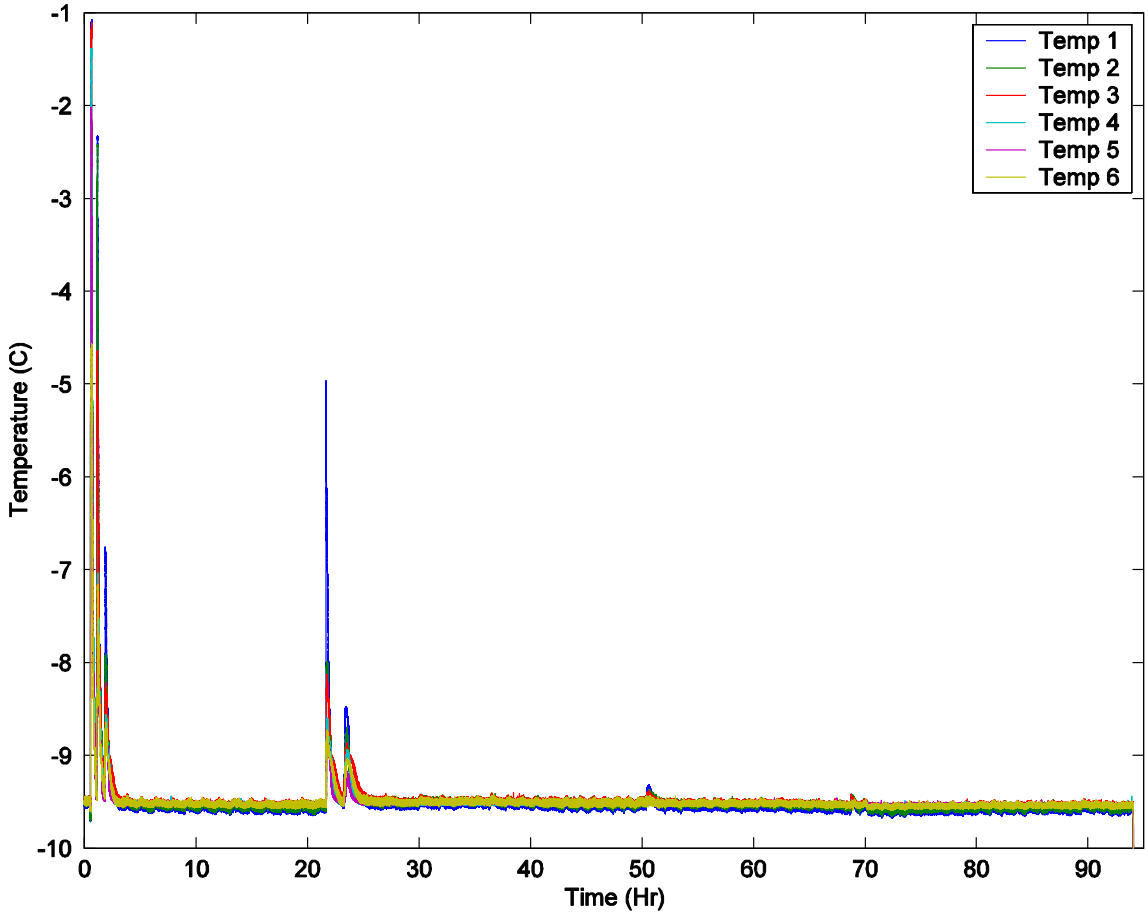

Figure 48. Time evolution of temperature during hydrate formation in crushed ice.

It is also seen from Figures 48 and 49 that the peak temperature in the subsequence pressurization cycle decreases and the decreasing trend continues as the number of cycle increases. This is in contrast with the peak pressure that remains roughly the same for different cycles. The decreasing trend of the pick temperature is mainly due to the decrease in the amount of gas injected into the vessel in the subsequent cycles.

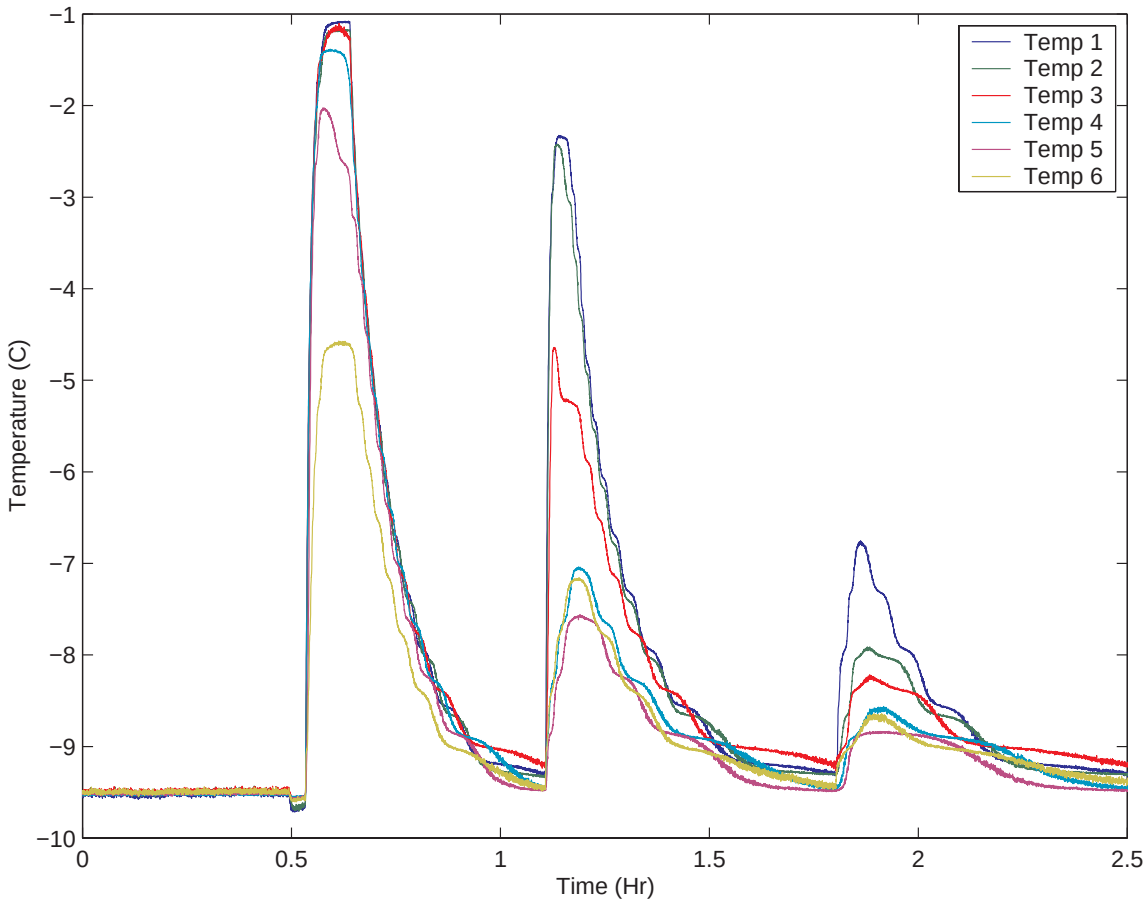

Figure 49. Details of temperature variations in the earlier stages of propane hydrate formation in crushed ice.

The amount of propane gas injected into the vessel was also continuously measured and the results are shown in Figure 50. The unit of the volume flow rate in this figure is standard liters per minute (sLPM). As noted before, the amount of mass entering the pressure vessel typically decreases in volume at the latter stages of hydrate formation process. The total amount of propane that was injected into the pressure vessel for this experiment was 8.4 L of propane.

Figure 51 shows the variations of pressure, temperature and volumetric flow rate during the hydrate formation in one graph. It is seen that the rise of the temperature and pressure coincide with those of injection of propane into the vessel. It is also seen that the peak pressure remains the same, while the peak temperature and mass flow decreasing with the number of pressurization cycle.

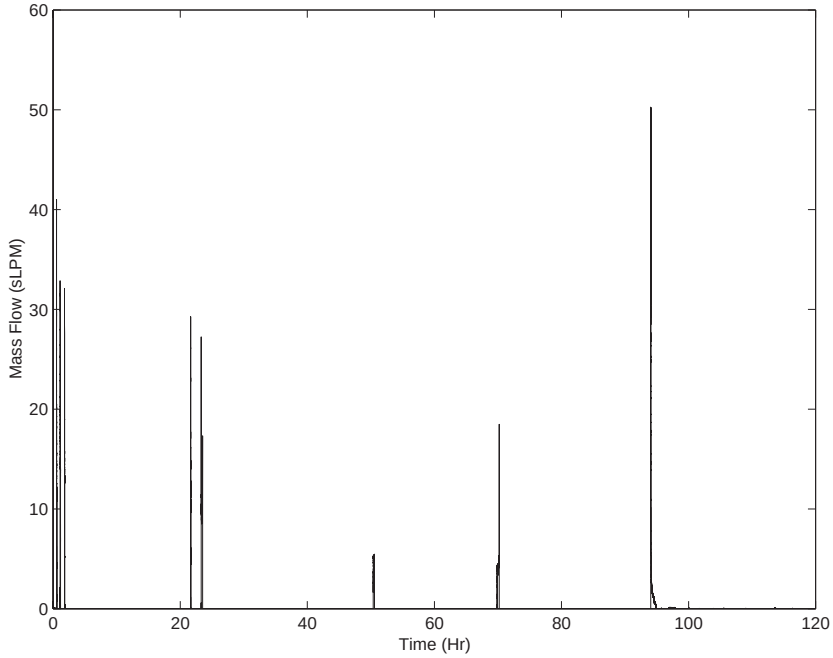

Figure 50. Mass Flow time evolutions for hydrate formation in crushed ice.

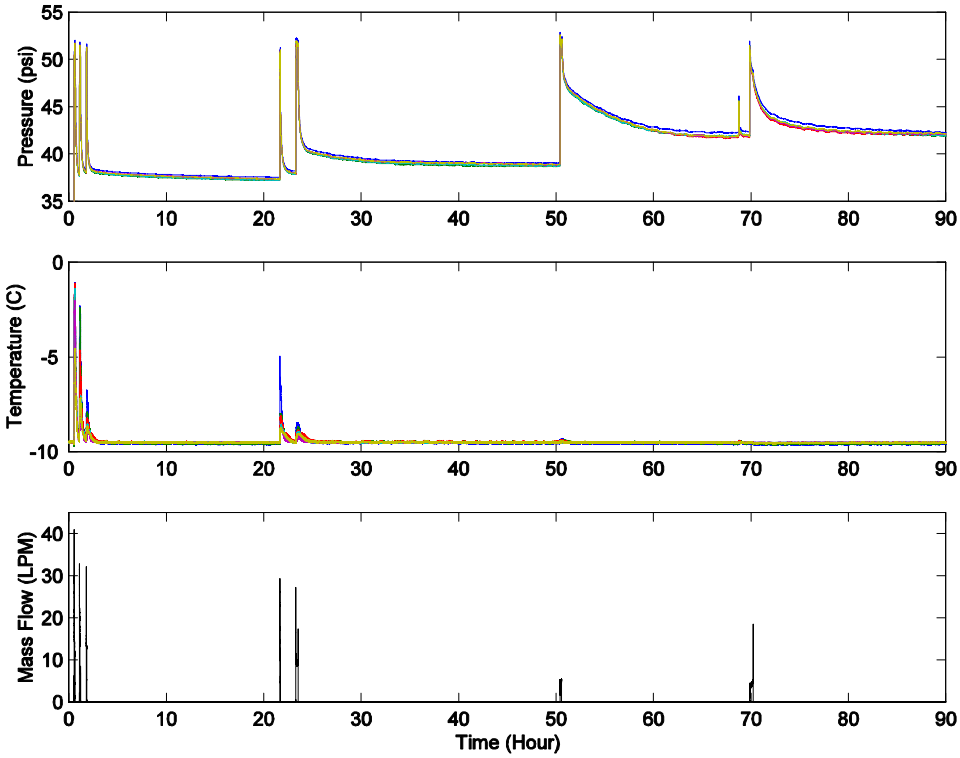

Figure 51. Time evolutions of pressure, temperature and flow rate for propane hydrate formation in crushed ice.

Propane Hydrate Formation in 75% Crushed ice and 25% Glass Bead

Propane hydrate formation and dissociation experiments were performed for a mixture of 75% crushed ice and 25% glass bead. The mixture was used to simulate hydrate formation and dissociation in unconsolidated sediments. The glass beads had a mean diameter of 100 μm and were nearly spherical. The crushed ice was flick like with a width of about 2 mm. The crushed ice and glass beads were mixed thoroughly before being packed uniformly into the vessel. The data was collected following the same procedure for the pure crushed ice outlined previously. The time evolution of the pressure during the hydrate formation is shown in Figure 52.

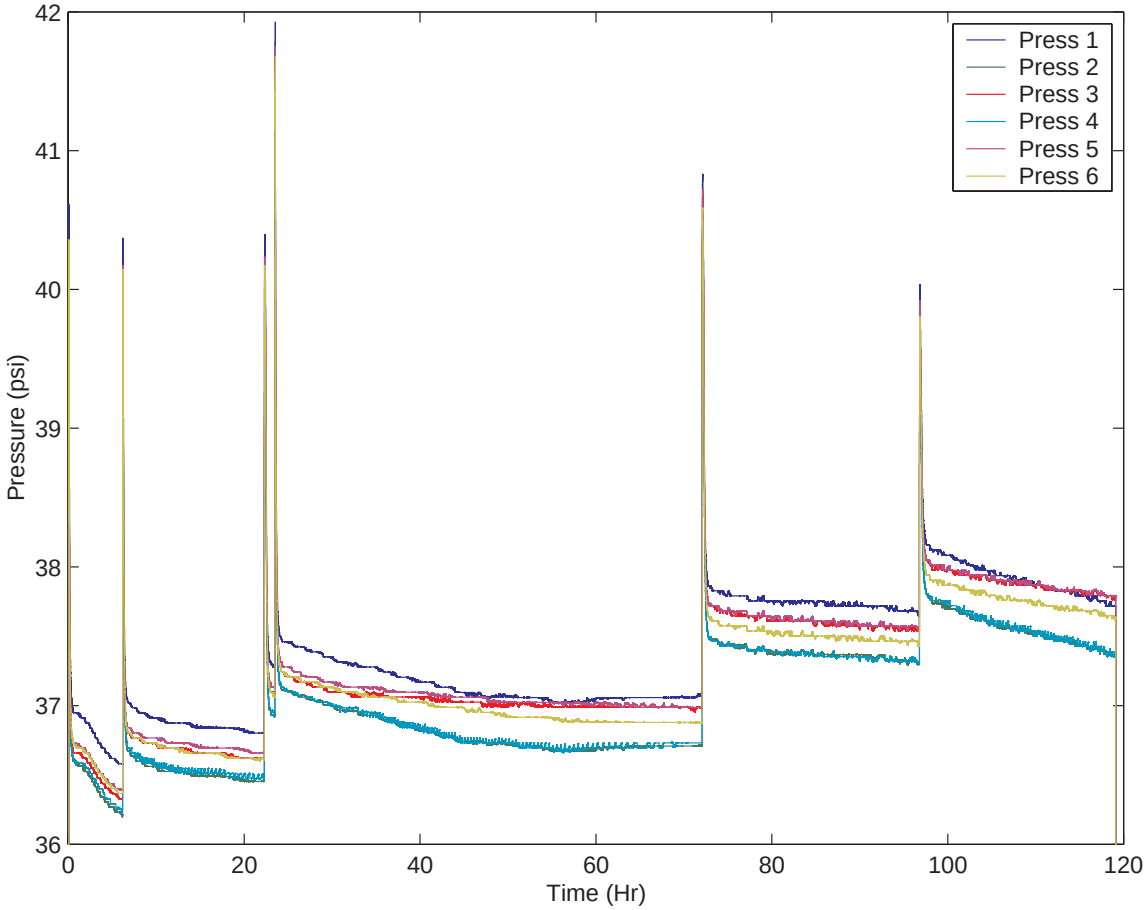

Figure 52. Time evolution of pressure during hydrate formation in the75% crushed ice-25% glass beads mixtures.

The trends of variation of pressure in Figure 52 are similar to those of Figure 40 for the pure crushed ice sample. There is an exponential decay after the sharp increase in the pressure after each injection. A detailed view of the first pressure cycle for the 25% glass beads mixture is shown in Figure 53. When compared to Figure 42, the time for the cycle to approach the equilibrium pressure is approximately the same.

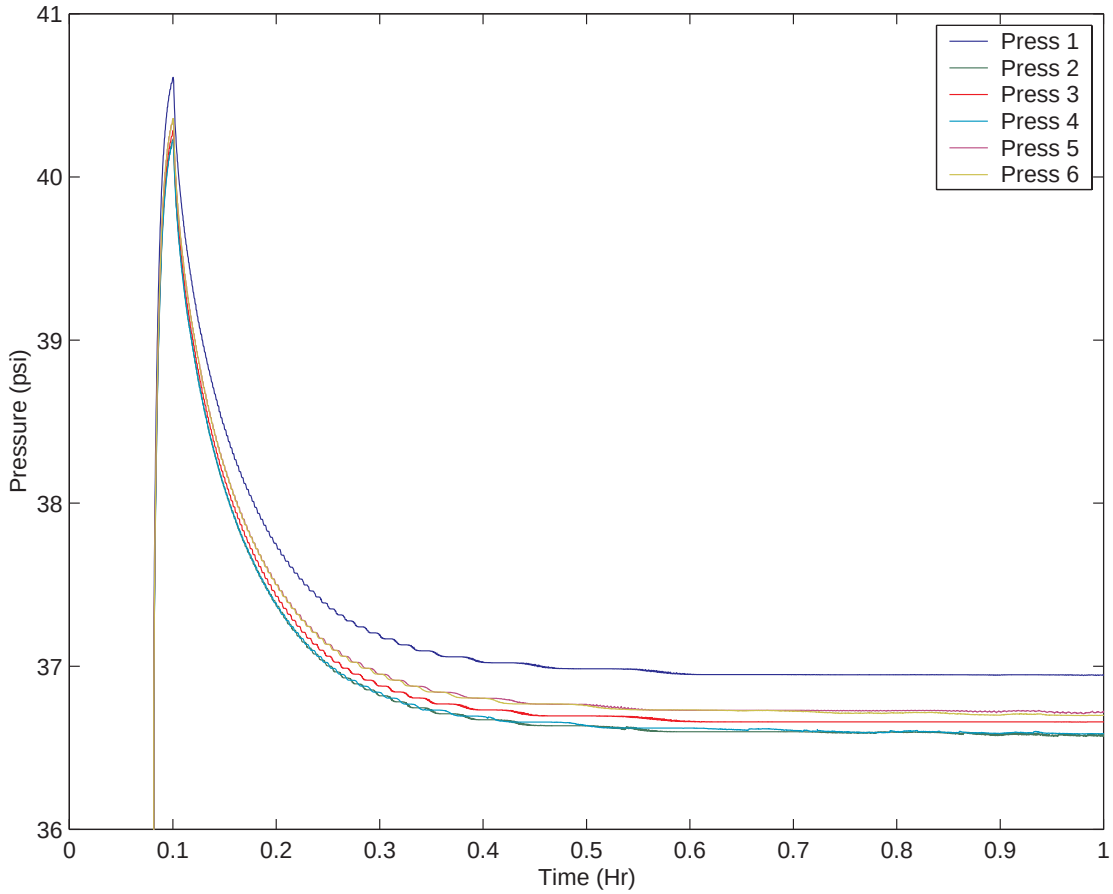

Figure 53. Time evolution of pressure during propane hydrate formation in the first cycle in the75% crushed ice-25% glass beads mixture sample.

The exponential fit to the pressure variation in the first cycle of pressurization for the75% crushed ice-25% glass beads mixture is shown in Figure 54. The corresponding k-value is found to be 9×10^{-5} which is smaller than that of the crushed ice. That is, the mixture with 25% beads will reach equilibrium in a longer time period.

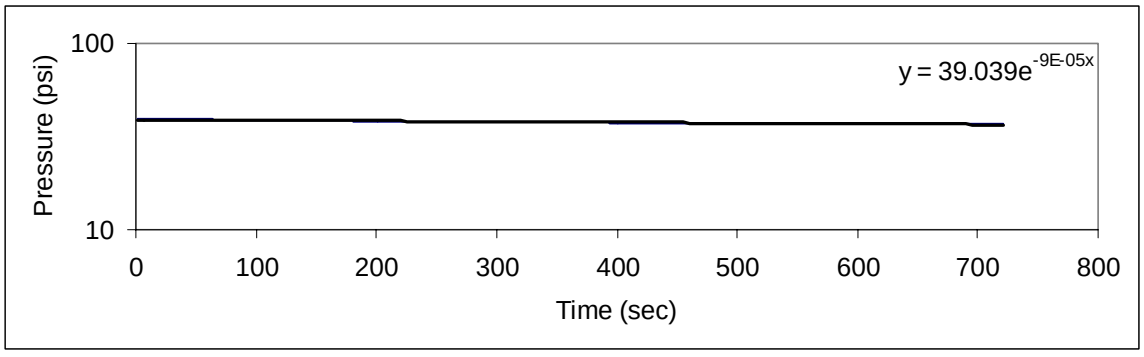

Figure 54. Exponential fit to pressure decay during hydrate formation in cycle 1 in the75% crushed ice-25% glass beads mixture sample.

Time variation of temperature for the mixture of 75% crushed ice and 25% glass beads mixture is shown in Figure 55. The trend of temperature variation is similar to that of Figure 48 for pure crushed ice. The temperature appears to increase as propane is injected into the vessel and that is followed by an exponential decay. In the first cycle, the increase is less that of the crushed ice. This is due to the fact that the mixture was subject to a lower gas pressure and the amount of gas injection was smaller. In contrast the case of pure crushed ice, however, the amount of temperature rise after each subsequent gas injection is relatively large compared to the temperature rise in the first cycle.

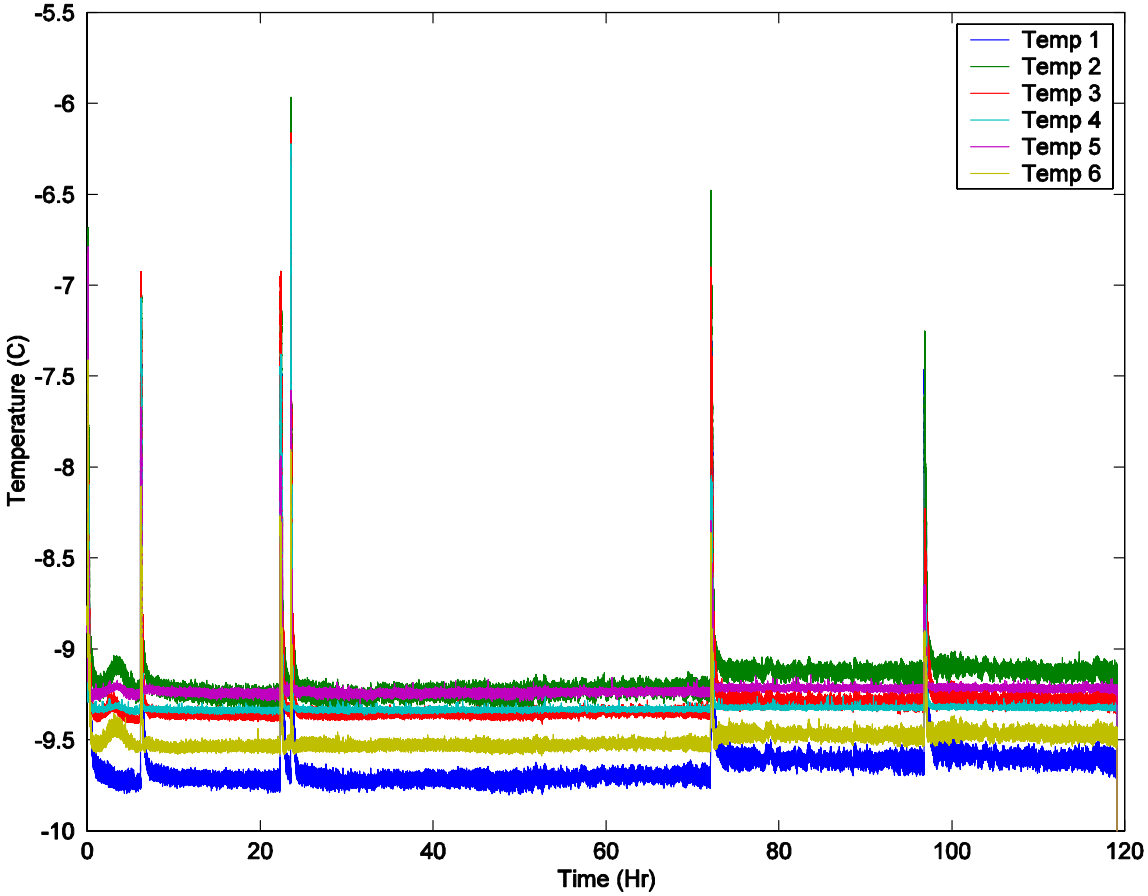

Figure 55. Time evolution of temperature during hydrate formation for the 75% crushed ice-25% glass beads mixture.

The cumulative volumetric amount of propane injected into the system is shown in Figure 56. This figure shows that the times for sharp changes in pressure and temperature coincide with the injection time. In the case of 75% crushed ice-25% glass beads sample, the total amount of propane injected was 3.87L, while for he pure crushed a total 8.37L of propane injected into the vessel.

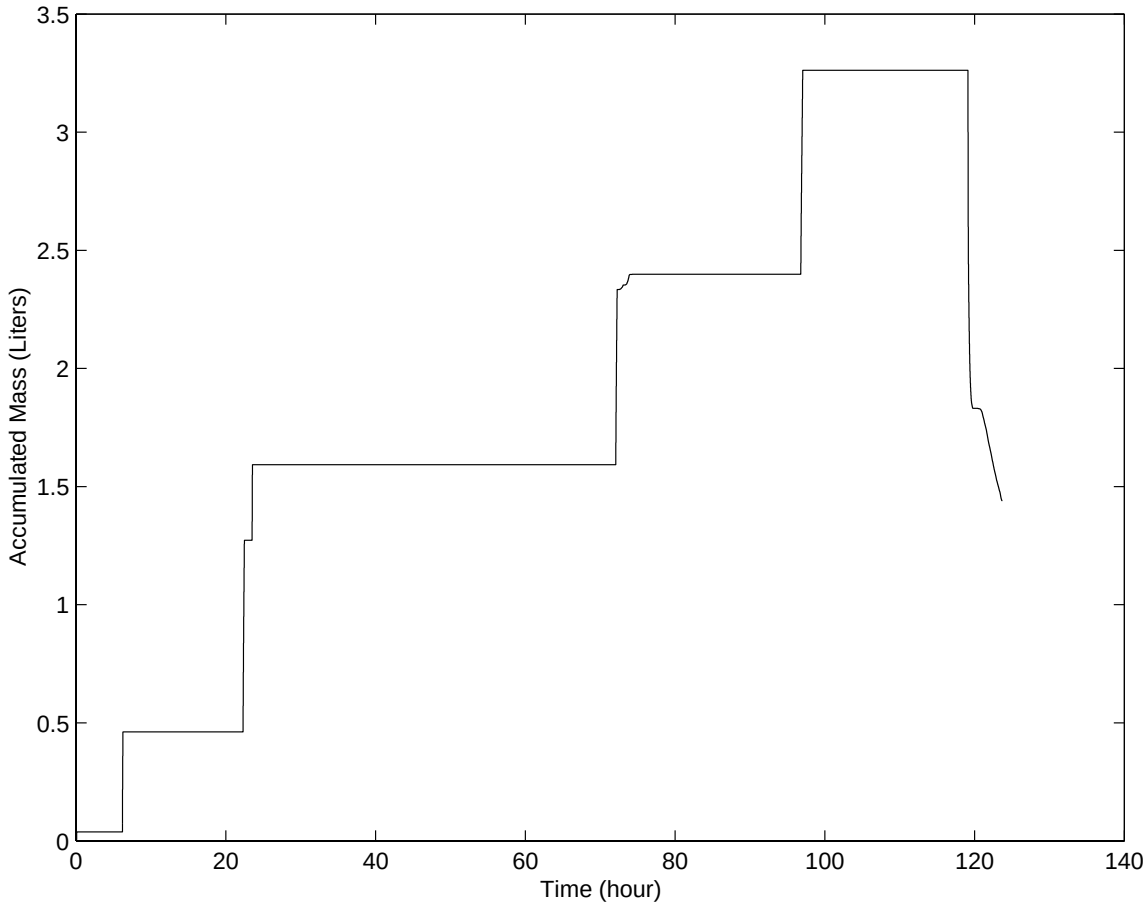

Figure 56. Cumulative volume of propane injection during hydrate formation for the 75% crushed ice-25% glass beads mixture.

Experimental Results for Hydrate Dissociation

The dissociation experiments were performed after the propane hydrate was formed. The dissociation process was initiated by opening the inlet/outlet valve and exposing the vessel to atmospheric pressure. The dissociation pressure and temperature data were obtained at high sampling rates for duration of two minutes after opening of the valve and initiation of depressurization process. The high sampling rate provided greater resolution of the variations for all parameters during dissociation. In this section, pressure, temperature and volumetric flow data are presented and discussed.

Hydrate Dissociation for Pure Crushed Ice Sample

As noted before, the depressurization was initiated after the hydrate formation, which typically took about five days. Figure 57 shows the variations of pressure during the

dissociation process for the pure crushed ice media. As the system is opened to the atmosphere, the propane hydrate dissociates rapidly and the vessel pressure decreases exponentially. This figure shows that approximately 1 hour is required for the vessel pressure to reach atmospheric pressure. At the initial stages of depressurization, Figure 57 shows that there are some small amplitude fluctuations in the pressure field. These fluctuations are attributed to the interaction of high speed gas flow and outlet piping and valve systems.

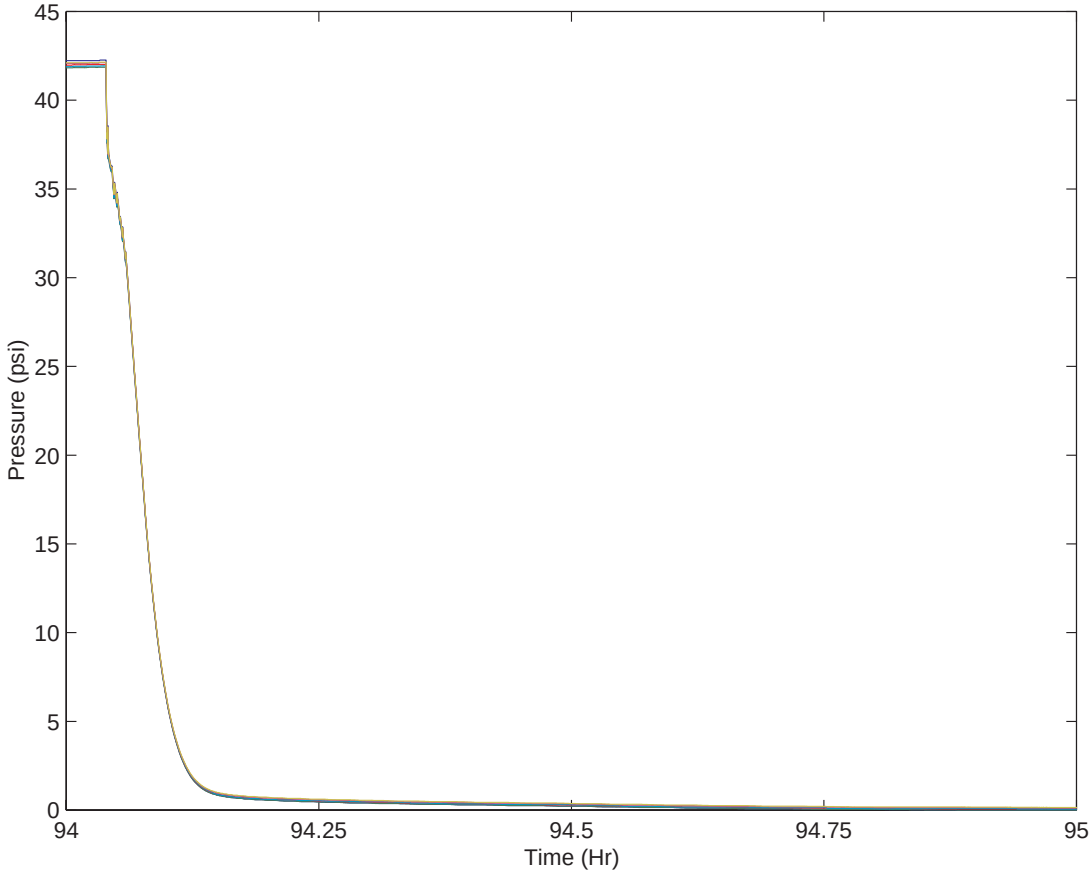

Figure 57. Time evolution of pressure for hydrate dissociation in crushed ice sample.

As described in the modeling section, the rate of hydrate dissociation depends on the pressure difference between the hydrate equilibrium pressure and the local gas pressure. Here the simplified version of Kim-Bishnoi model is used. Accordingly, the pressure decay is given by Equation (7-10). The decay rate for the pure ice sediment has been obtained by averaging the six sensors response during the depressurization. The data is then plotted on a semi log graph, where an exponential curve is fitted to the data and model parameters are evaluated. Figure 58 shows the averaged pressure data during the dissociation, the exponential curve fit, and the corresponding k_3-value. (Note that the second term of Equation (7-10), which is assumed small, is neglect.) The model shows a good agreement

with the experimental data decay rate. Figure 58 also shows a k_3-value of 0.011, which is much larger than the k-values for the hydrate formation.

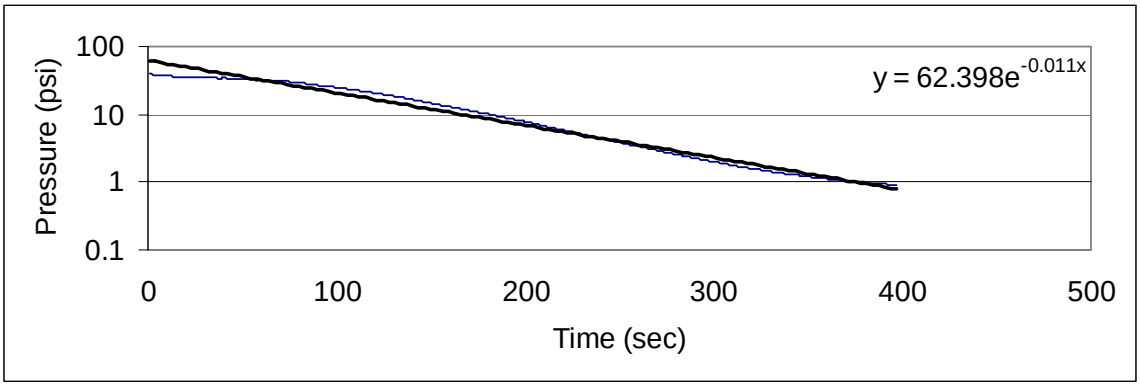

Figure 58. Comparison of the experimental data with an exponential fit for hydrate dissociation in pure crushed ice sample.

Figure 59 shows the first 15 minutes of the dissociation process. The pressure reduces to approximately 1 psi in 6 minutes after the valve is opened. This indicates that the hydrate dissociation is a comparatively a rapid process, compared to the 5 days needed for the formation.

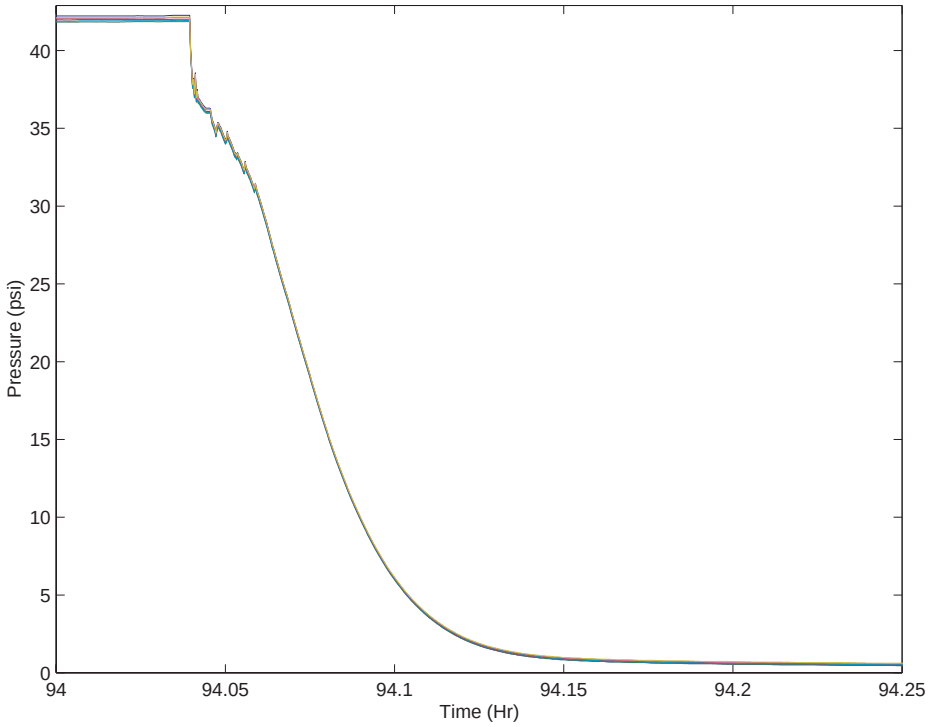

Figure 59. Details of time evolution of pressure for hydrate dissociation in pure crushed ice sample.

The time variation of temperature in the vessel for the propane dissociation in pure crushed ice sample is shown in Figure 60. The temperature drops sharply to -40 ºC when the

dissociation is initiated as heat is absorbed by the process and gas pressure is reduced due to the gas leaving the vessel. The temperature is then gradually increases to the bath temperature. The sample temperature remains below the bath temperature for a long period of time (about 3 hours) compared to the pressure decay time which is about fraction of an hour. Temperature reading of sensor 1 shows that the temperature increases at a higher rate compared to the other sensors. The other sensors, however, do not show a specific order and their order also changes with times until the bath temperature is reached.

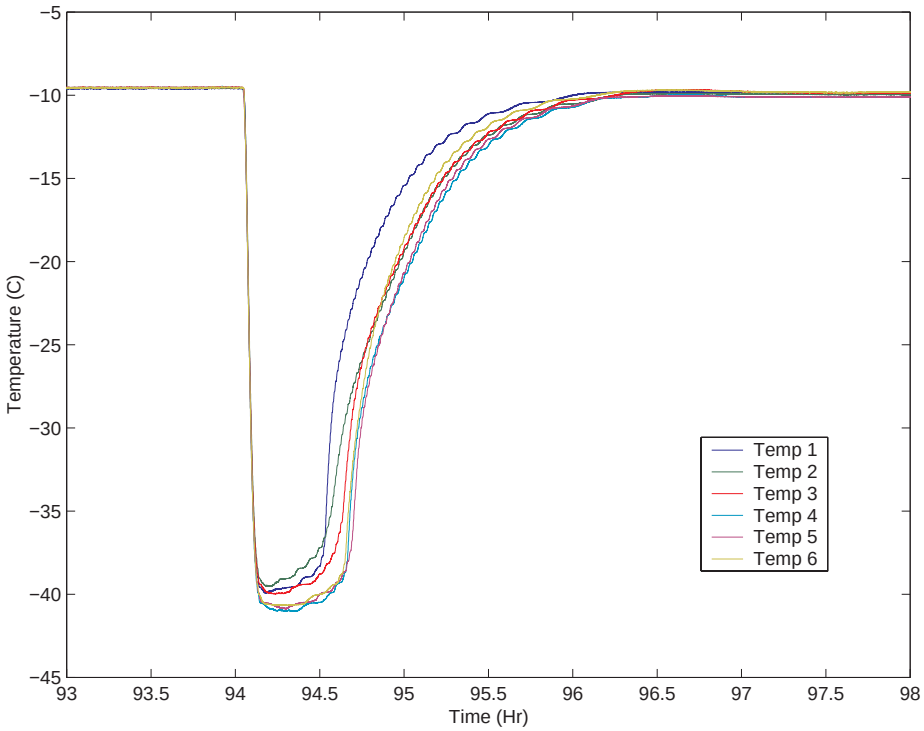

Figure 60. Time evolution of temperature for hydrate dissociation in the crushed ice sample.

The volumetric flow rate exiting the system is shown in Figure 61. The flow rate follows the same trend as the pressure, with 95% of the propane hydrates being dissociated and exited the system in about15 minutes after the initiation of depressurization. Some fluctuations in the flow rate in the first 80 seconds after the depressurization is initiated is noticed in Figure 61. The initial fluctuations in the flow rate are attributed to the system piping.

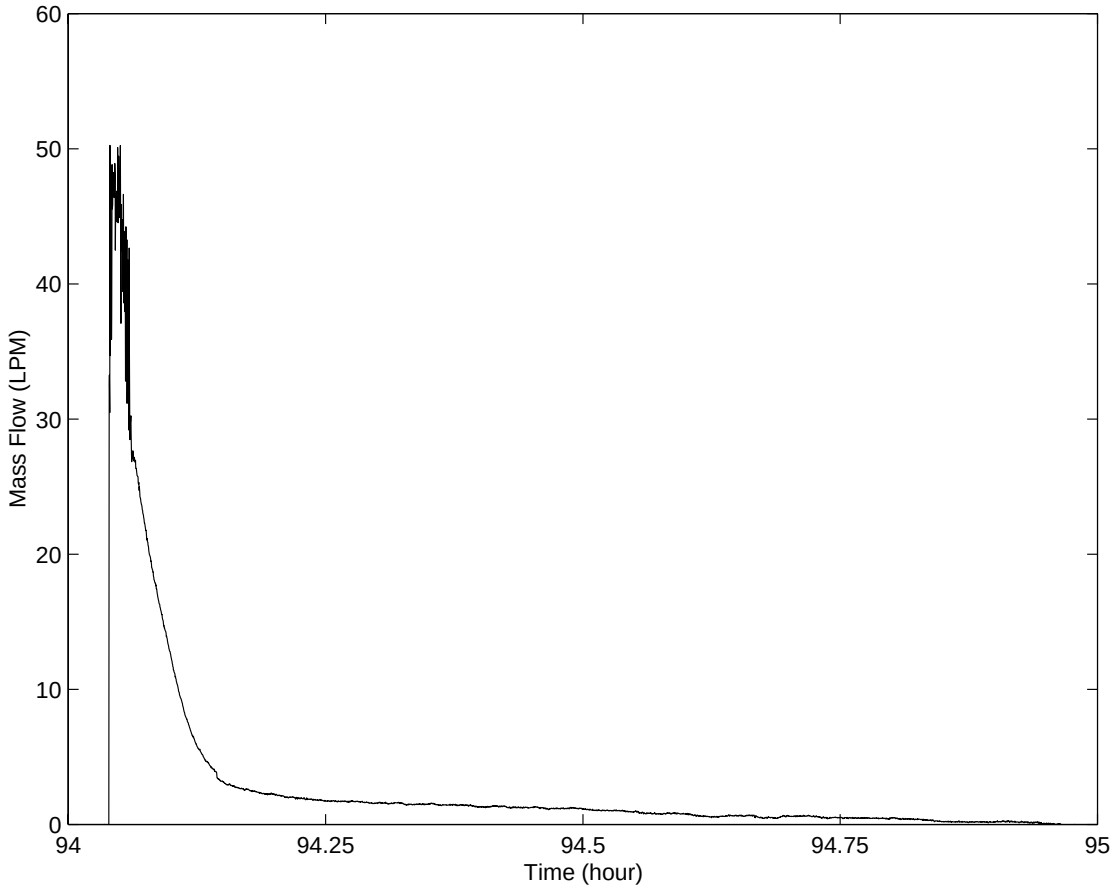

Figure 61. Time evolution of mass flow for hydrate dissociation in crushed ice sample.

Variations of vessel pressure and volumetric flow rate on an expanded scale are shown in Figure 62. It is seen that the decay patterns of pressure and volume flow rate follow the same trends. In particular, in the earlier stages both pressure and flow rate show some small scale oscillation, which is believe to be due to the high speed gas flow in the outlet pluming. After the initial stages, the decay of the vessel pressure and volume flow rate decay follow a smooth exponential decay.

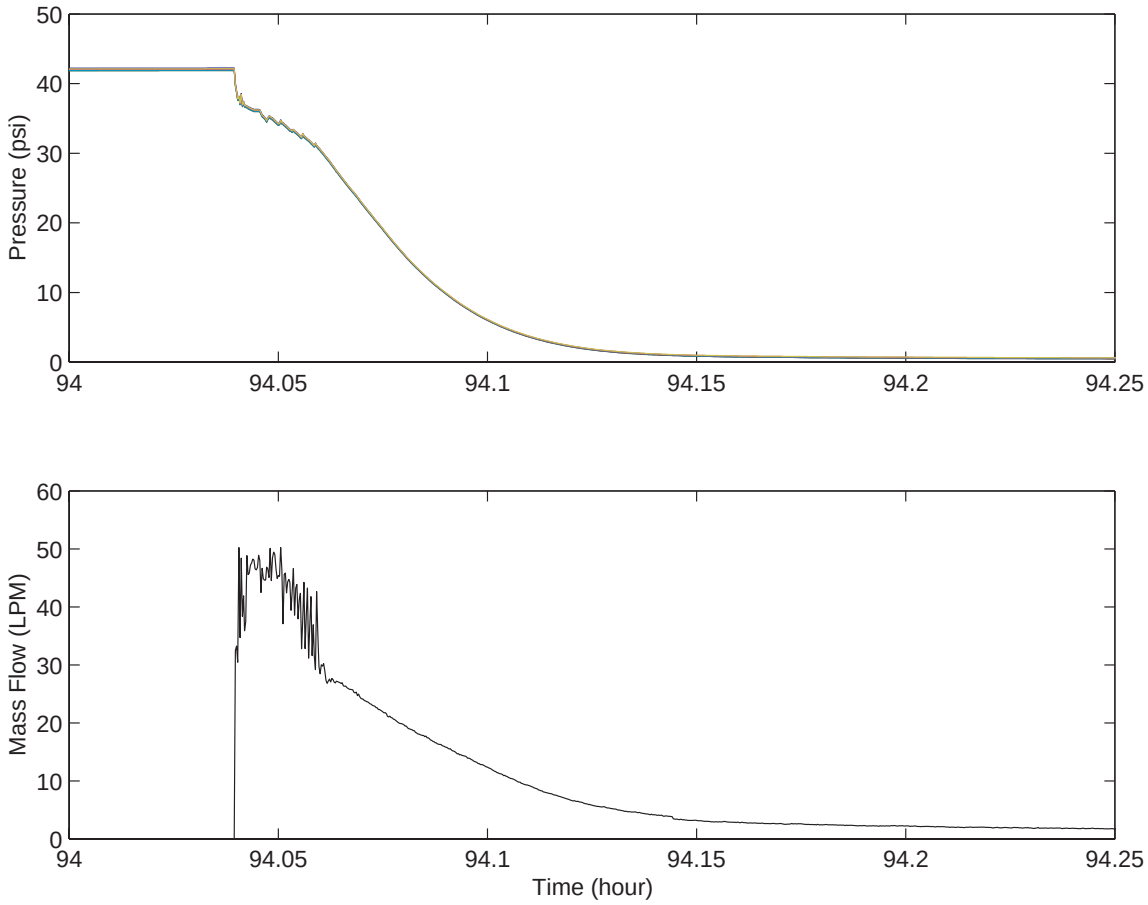

Figure 62. Time evolutions of pressure and mass flow rate for hydrate dissociation in The crushed ice sample.

Hydrate Dissociation in 75% Crushed Ice 25%-Glass Beads Mixtures

The experimental data for the propane hydrate dissociation for the mixture of 75% crushed ice and 25% glass beads are described in this section. Figure 63 shows the time evolution of the pressure. The rapid exponential decay of pressure is similar to that of the pure ice sample. However, the pressure for mixture of ice and glass beads approaches atmospheric condition in approximately half the time compared to the pure ice sample shown in Figure 57.

The experimental data for the pressure variation in the mixture sample is plotted in a semi-log scale in Figure 64 and is fitted to an exponential curve. This figure shows that the exponential decay fits the data very well. The corresponding decay rate is k_3=0.0177, which

is higher than the decay rate of k_3=0.011 for crushed ice. It should also be emphasized that the initial pressure for the pure crush ice case was 42 psi, while for the mixture case was about 38 psi.

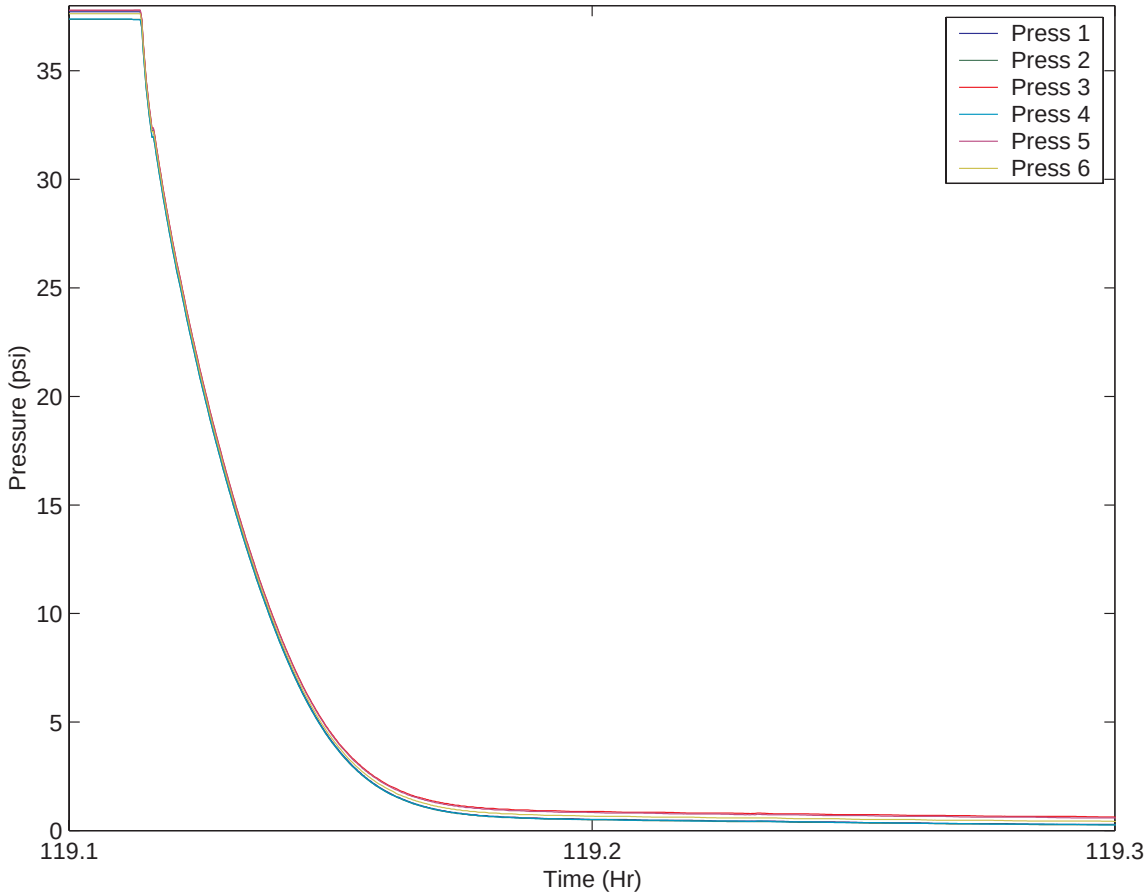

Figure 63. Time evolution of pressure for hydrate dissociation for the mixture of 75% crushed ice -25% glass beads sample.

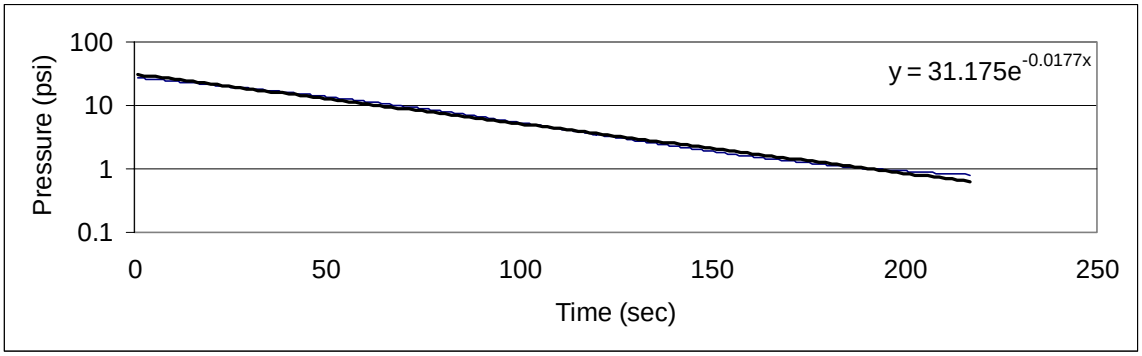

Figure 64. Comparison of the experimental data with an exponential fit for hydrate dissociation in mixture of crushed ice-glass beads sample.

Figure 65 compares the experimental data with the exponential curve fit. It is seen that the exponential decay provides for a reasonable representation of the pressure variation during the dissociation process.

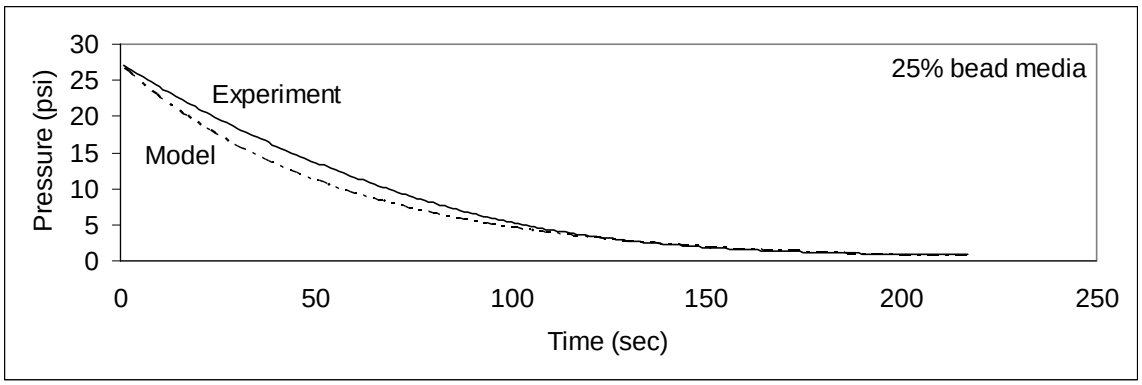

Figure 65. Comparison of the experimental data with the exponential fit for hydrate dissociation in the mixture of crushed ice-glass beads sample.

The time variations of temperature during the propane hydrate dissociation for the sample with 25% glass beads is shown in Figure 66. The general features of the temperature variation is similar those of Figure 60 for the pure crushed ice sample. The temperature drops rapidly from -9 ºC to about -35 ºC as the depressurization begins. The temperature then increases gradually and reaches the bath temperature in about 1.5 hours.

Figure 67 compares the temperature variations during the propane hydrate dissociation in pure crushed ice sample with the sample with 25% glass beads for first two hours. While the general features are comparable, there are certain differences. The temperature in the pure ice sample stays at -40 ºC for approximately 20 to 30 minutes before rising. The temperature in the sample with 25% glass remains at -38 ºC for about 10 to 12 minutes. One reason for the difference in behavior may be attributed to the fact that the crushed ice sample was prepared at higher pressure and contains larger amount of hydrate. The sample with 25% beads, however, was prepared at lower gas pressure and contains comparatively less hydrate. Thus, during the dissociation process the crushed ice sample maintains it lower temperature associated with the hydrate dissociation for a longer period.

Figures 66 and 67 show that the spatial distribution of the temperature in the vessel with 25% glass beads as recorded by the temperature sensors is different from that of the pure crushed ice sample. This observation further indicates that the flow and heat transfer in sample does not follow a simple trend. It is conjectures that the sample forms cracks and fracture that significantly affect the spatial distribution of pressure and temperature in the vessel. The spatial order of the temperature also appears to change in time.

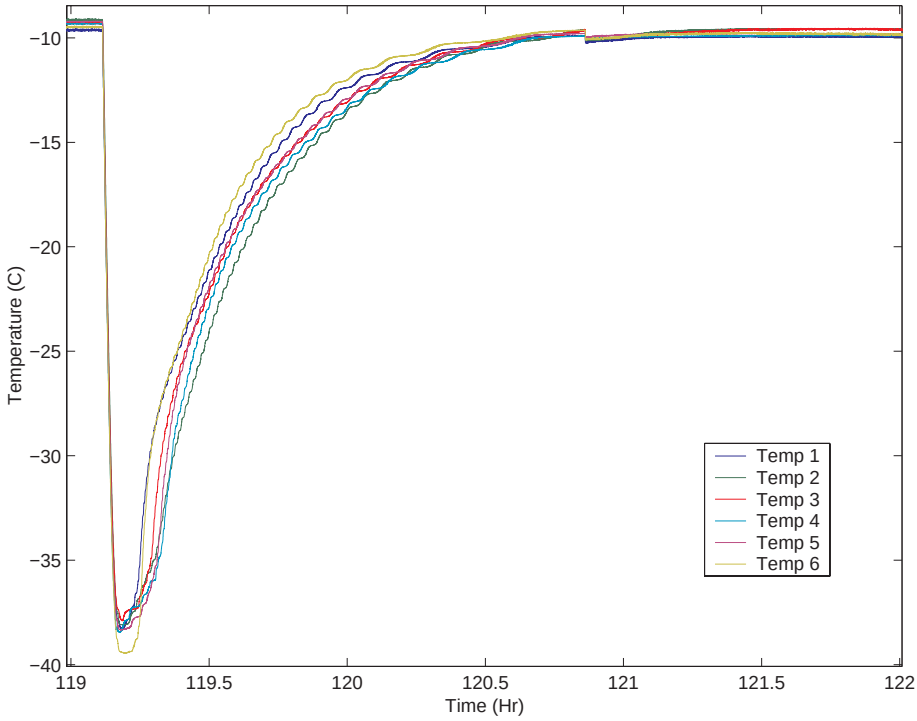

Figure 66. Time evolution of temperature for propane hydrate dissociation in the sample with 25% glass beads.

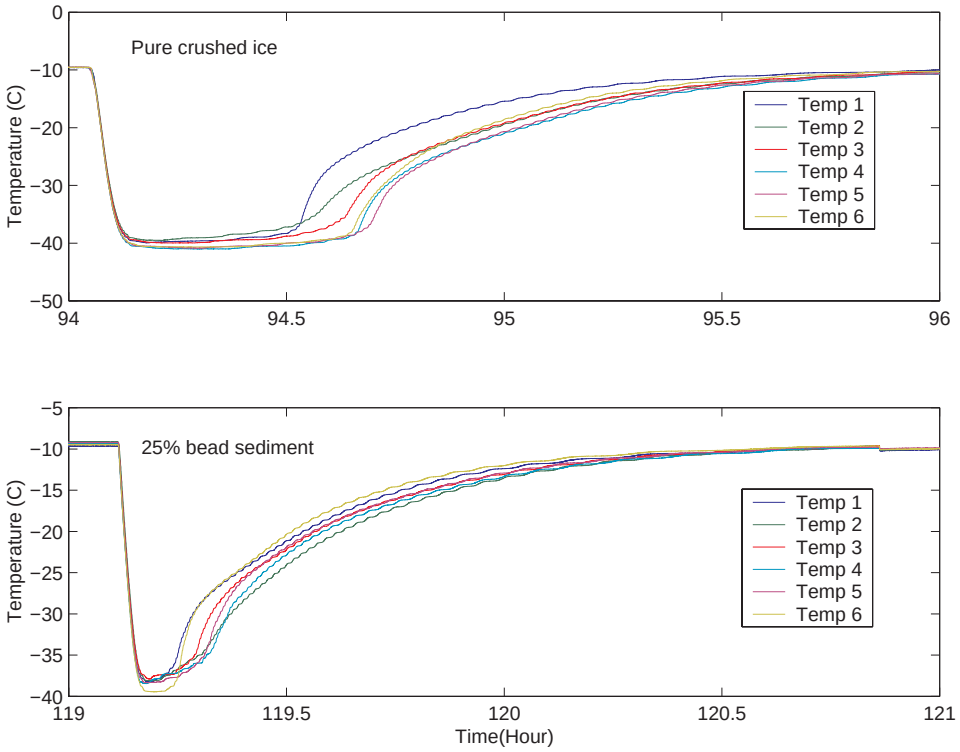

Figure 67. Comparison of time evolution of temperature during hydrate dissociation.

Figure 68 shows the volume flow rate during the propane hydrate dissociation in the sample with 25% glass beads. It is seen that the flow rate decreases sharply with time, and in about 6 minutes, 95% of the mass leaves the vessel. Comparing with the pure crushed ice case, the sample with 25% glass beads requires half as much time to reach to the limit of negligible flow rate. As noted before, the amount of propane injected into the vessel for the sample with 25% glass beads was about 3.9 L which is less than half of that for the pure crushed ice case.

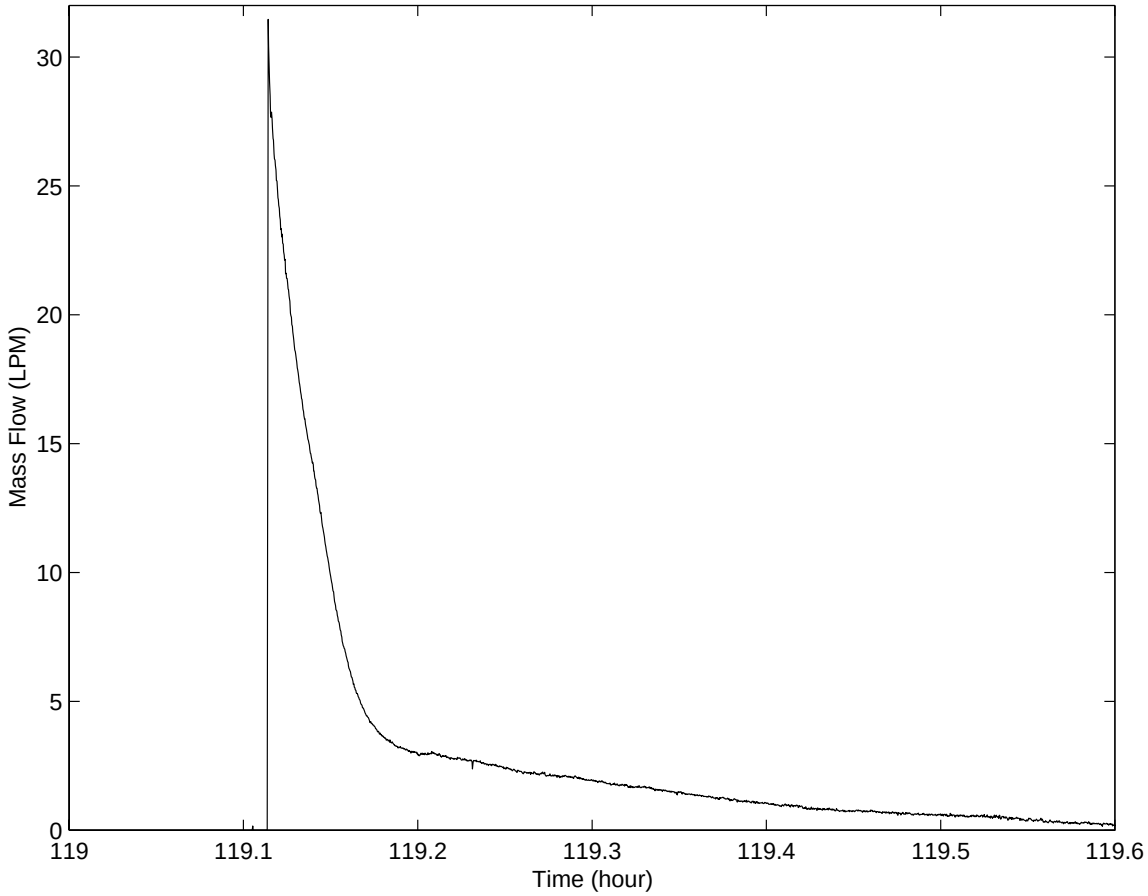

Figure 68. Time evolution of volumetric flow rate during propane hydrate dissociation for the sample with 25% glass beads.

GRADUATE STUDENTS

A number of graduate students (six Ph.D. and three M.S.) have been involved at various stages of this project. Three Ph.D. and two M.S. students have completed their degrees.

- K. Nazridous (Ph.D. 2006), Mech. & Aero. Engineering, Clarkson University. (Currently with CIIT)
- T.H. While (M.S. 2003), Mech. & Aero. Engineering, Clarkson University. (Currently with Proctor and Gamble)
- C. Ji (MS, 2002, Ph.D. student), Mech. & Aero. Engineering, Clarkson University.
- X. Zhang (Ph.D. Student), Mech. & Aero. Engineering, Clarkson University.
- W. Chen (Ph.D. Student) student, Mech. & Aero. Engineering, Clarkson University.
- A.R. Mazaheri (Ph.D. 2004) Mech. & Aero. Engineering, Clarkson University (Currently NRC Fellow at NETL, DOE)
- J. Cao (Ph.D. 2000) Mech. & Aero. Engineering, Clarkson University. (Currently with MBNA)
- R. Chavali (M.S. Student), Mech. & Aero. Engineering, Clarkson University.

PUBLICATIONS

Thesis

Kambiz Nazridous, Fundamentals and Applications of Environmental and Geophysical Multiphase Flows, Ph.D. Thesis, Clarkson University, Potsdam, NY, 2006.

Ali Reza Mazaheri, Fundamentals of Gas-Solid and Gas-Liquid Flows in Porous Media, Ph.D. Thesis Clarkson University, Potsdam, NY, 2003.

Timothy H. White, An Experimental Setup for Propane Hydrate Formation and Dissociation within Porous Media, MS Thesis, Clarkson University, Potsdam, NY 2003.

Chuang, Ji, Numerical Computation for Natural Gas Production from In-Situ Hydrate Reservoir, MS Thesis, Clarkson University, Potsdam, NY, 2002.

Chuang, Ji, Computational Modeling of Multiphase Flows During Hydrate Dissociation, Ph.D. Thesis, Clarkson University, Potsdam, NY, (In Progress).

Journals

Cao, J. and Ahmadi, G., "Gas-Particle Two-Phase Flow in Horizontal and Inclined Ducts," International Journal of Engineering Science, Vol. 38, pp. 1961-1981 (2000).

Ji, C., Ahmadi, G., and Smith, D.H., "Natural Gas Production from Hydrate Decomposition by Depressurization," Chemical Engineering Science, Vol. 56, pp. 5801-5814 (2001).

Ji, C., Ahmadi, G. and Smith, D.H., Experimental and Computational Study of Fluid Flow Phenomena in Carbon Dioxide Sequestration, Journal of Energy and Environment Research, Vol. 2, pp. 99-108 (2002).

Ji, C., Ahmadi, G. and Smith, D.H., Constant Rate Natural Gas Production from a Well in a Hydrate Reservoir, Energy Conversion and Management, Vol. 44, pp. 2403-2423 (2003).

Ahmadi, G., Mazahri, A.R. and, Smith, D.H. A Model for Multiphase Flows through Poroelastic Media, Journal Porous Media, Vol. 6, pp. 249-262 (2003).

Ahmadi, G., Ji, C. and Smith, D.H., Numerical Simulation of Natural Gas Production from Methane Hydrate Dissociation, Journal of Petroleum Science and Engineering, Vol. 41, pp. 269-285 (2004).

Mazaheri, A.R., Zerai, Ahmadi, G., Kadambi J.R., Saylor, B.Z., Oliver M., Bromhal, G.S., Smith, D.H., Computer Simulation of Flow through a Lattice Flow-Cell Model, Advances in Water Resources, Vol. 28, pp. 1267-1279 (2005)

Ahmadi, G., Cao, J., Schneider, L. and Sadiki, A., A Thermodynamical Formulation for Chemically Active Multiphase Turbulent Flows, International Journal of Engineering Science (In Press).

Ji, C., Ahmadi, G., and Smith, D.H., Natural Gas Production from Hydrate Dissociation: An Axisymmetric Model, Journal of Petroleum Science and Engineering, (In Press).

Ahmadi, G., Ji, C. and Smith, D.H., Production of Natural Gas From Methane Hydrate by A Constant Down-Hole Pressure Well**,** Journal of Energy Conversion and Management (In Press).

Conferences

C. Ji, G. Ahmadi and D.H. Smith, "Computational Simulation for Natural Gas Production from Hydrate Decomposition," Annual Technical Meeting of the Center for Advanced Material Processing (CAMP), Lake Placid, NY, May 23-25, 2000.

Sadiki, A. and Ahmadi, G., "A Thermodynamical Formulation for Chemically Active Multiphase Flows," Trends in Numerical and Physical Modeling for Industrial Multiphase Flows, Institut d'Etudes Scientifiques de Cargese (Corse), France. September 26-28, 2001.

Zhang, X. and Ahmadi, G., "Gas-Particle Two-Phase Flow in a Horizontal Channel," 20th Annual Conference of the American Association for Aerosol Research, AAAR 2001, Portland, Oregan, October 15-19, 2001.

G. Ahmadi, "Fundamentals of Natural Gas Flow in a Hydrate Reservoir," Methane Hydrates Interagency R&D Conference, Washington, DC, March 20-22, 2002.

K. Nazridoust, T. White, C. Ji, G. Ahmadi, D.H. Smith, M. Dean "Natural Gas Production from Hydrate Dissociation," Annual Technical Meeting of the Center for Advanced Material Processing (CAMP), Saratoga Spring, NY, May 13-15, 2002.

C. Ji, G. Ahmadi, W. Zhang and D.H. Smith, "Natural Gas Production from Hydrate Dissociation- A Comparison of Axisymmetric Models," 4th International Conference on Gas Hydrate, Yokohama, Japan, May 19-23, 2002.

K. Nazridoust, T. White, C. Ji, G. Ahmadi, M. Dean and D.H. Smith, "A Computer Model

for Natural Gas Production from Hydrate Reservoirs," 21st Annual Conference of the American Association for Aerosol Research, AAAR 2002, Charlotte, NC, October 7-11, 2002.

D.H. Smith, G. Ahmadi, Chuang Ji, G. Bromhal, and M. Ferer, "Experimental and Numerical Studies of Gas-liquid Displacement In Flow Cells, With Application To Carbon Dioxide Sequestration In Brine Fields," FEDSM2002-31296, Proceedings of ASME FEDSM'02, ASME Fluids Engineering Division Summer Meeting, Montreal, Quebec, Canada, July 14-18, 2002.

K. Nazridoust, T. White, C. Ji, G. Ahmadi, M. Dean and D.H. Smith, "A Computer Model for Natural Gas Production from Hydrate Reservoirs," 21st Annual Conference of the American Association for Aerosol Research, AAAR 2002, Charlotte, NC, October 7-11, 2002.

E. M. Noto and G. Ahmadi, "A Preliminary Study of Rheological Behavior of Bauxite Residue," 21st Annual Conference of the American Association for Aerosol Research, AAAR 2002, Charlotte, NC, October 7-11, 2002.

G. Ahmadi, A. R. Mazaheri and D.H. Smith, "Multiphase Flow Through Poro-Elastic Media-A Continuum Model," IMECE2002-32492, Proceedings of ASME International Mechanical Engineering Congress, New Orleans, LA, November 17-22, 2002.

G. Ahmadi, "Natural Gas Flow in a Hydrate Reservoir," Methane Hydrate R&D Conference and Gulf of Mexico Nationally Occurring JIP Workshops, Westminster, Colorado, September 29-October 1, 2003.

E. Noto, G. Ahmadi, and G. Campbell, "Rheological Behavior of Bauxite Residue and Bauxite Residue Derivative," 4th International Conference on Mechanics of Time Dependent Materials, Lake Placid, NY, October 7-10, 2003.

E. Noto, G. Ahmadi, and G. Campbell, "Characterization of Bauxite Residue and Derivatives at Varying pH Values," 75th Annual Meeting of Society of Rheology, Pittsburgh, PA, October 12-16, 2003.

A.R. Mazaheri, G. Ahmadi, and D.H. Smith, "Hysteresis and Dynamics Effects in Two-Phase Flows in Porous Media," 22nd Annual Conference of the American Association for Aerosol Research, AAAR 2003, Anaheim, CA, October 20-24, 2003.

A.R. Mazaheri, G. Ahmadi, and D.H. Smith, "Multiphase Flows through Porous Media," 22nd Annual Conference of the American Association for Aerosol Research, AAAR 2003,

Anaheim, CA, October 20-24, 2003.

G. Ahmadi, "Computational Modeling of Multiphase Flows – Environmental Applications," (Invited Lecture) Third International Symposium on Advanced Fluid Information, AFI-2003, New York, NY, November 21-22, 2003. Also in AFI-2003, Fluid-Informatics for Biomedical and Environmental Quality Applications, Ed. H. Higuchi and T. Hayase, pp. 15-20, 2003.

K. Nazridoust and G. Ahmadi, "Multiphase Fluid Flow Through an Artificially Induced CT-Scanned Fracture," Annual Technical Meeting of the Center for Advanced Material Processing (CAMP), Canandaigua, NY, May 12-14, 2004.

R. Mazaheri, G. Ahmadi, Z. Karpyn, K. Nazridoust, A.S. Grader, P.M. Halleck, A. R. Mazaheri, and D.H. Smith, "Single-Phase and Multi-Phase Fluid Flow through an Artificially Induced, CT-Scanned
Fracture," in the Proceeding of XVth International Conference of Computational Method in Water Resources (CMWR XV), Chapel Hill, NC, June 13-17, 2004.

G. Ahmadi, A.R. Mazaheri and D.H. Smith, "Multiphase Flows Through Fractured Rocks," ASME Heat Transfer/Fluid Engineering Summer Conference, Charlotte, NC, July 11-15, 2004.

K. Nazridoust, Z. Karpyn, G. Ahmadi, A.S. Grader, P.M. Halleck, A. Mazaheri, and D.H. Smith, "Single-Phase and Multi-Phase Fluid Flow Through an Artificially Induced, Ct-Scanned Fracture," 23rd Annual Conference of the American Association for Aerosol Research, AAAR 2004, Atlanta, GA, October 4-8, 2004.

A. R. Mazaheri, M. Ferer, G. Ahmadi, and D. H. Smith, "Navier-Stokes Pore Scale Modeling of Two-Phase Flow through an Artificial Porous Medium," American Geological Union (AGU) Meeting, December 13-17, 2004.

W. Chen and G. Ahmadi, "Bubble Size Distribution in Turbulent Bubbly Flows," Annual Technical Meeting of the Center for Advanced Material Processing (CAMP), Canandaigua, NY, May 11-13, 2005.

W. Chen, G. Ahmadi and J. Taylor, "Numerical and Study on Bubble Motion and Deformation in a Simple Shear Flow," Annual Technical Meeting of the Center for Advanced Material Processing (CAMP), Canandaigua, NY, May 11-13, 2005.

M. Richards, J. Cook, G. Ahmadi, S. Powers and D.H. Smith, "Experimental Study of Multiphase Fluid Flow through Porous Media," Annual Technical Meeting of the Center for Advanced Material Processing (CAMP), Canandaigua, NY, May 11-13, 2005.

K. Nazridoust and G. Ahmadi, “Single-Phase Flows Through Fractured Rocks,” Annual Technical Meeting of the Center for Advanced Material Processing (CAMP), Canandaigua, NY, May 11-13, 2005.

K. Nazridoust and G. Ahmadi, “Methane Hydrate Dissociation in Sand Stone Cores - A Numerical Simulation Approach,” Annual Technical Meeting of the Center for Advanced Material Processing (CAMP), Canandaigua, NY, May 11-13, 2005.

E. M. Humiston, G. Ahmadi, and G. Campbell, “Rheological Behavior of Bauxite Residue and Bauxite Residue Derivatives,” 79th ACS Colloid and Surface Science Symposium, Clarkson University, Potsdam, NY, June 12-15, 2005.

K. Nazridoust, G. Ahmadi and D.H. Smith, “A New Friction Factor Correlation for Laminar and Single-Phase Fluid Flow through Fractured Rocks,” 79th ACS Colloid and Surface Science Symposium, Clarkson University, Potsdam, NY, June 12-15, 2005.

K. Nazridoust, and G. Ahmadi, “Numerical Simulation of Methane Hydrate in Sandstone Cores,” 79th ACS Colloid and Surface Science Symposium, Clarkson University, Potsdam, NY, June 12-15, 2005.

K. Nazridoust, G. Ahmadi, Z. Karpyn, A.S. Grader, P.M. Halleck, A.R. Mazaheri, and D.H. Smith, "Gas-liquid Flows through a Rock Fracture," ASME Fluid Engineering Summer Conference, Houston, TX, June 19-23, 2005, paper FEDSM2005-77235

D. Crandall, G. Ahmadi, G. Bromhal, and D.H. Smith, “Volume Fraction Analysis of Two-Phase Flows in Fractures,” 2005 Eastern Section of American Association of Petroleum Geologists, 34th Annual Meeting, Morgantown, WV, September 18-20, 2005.

K. Nazridoust, G. Ahmadi, D.H. Smith, A New Friction Factor for Laminar, Single-Phase Flows Through Fractures, 24th Annual Conference of the American Association for Aerosol Research, AAAR 2005, Austin, TX, October 17-21, 2005.

D. Crandall, G. Ahmadi and D.H. Smith, “Flow through Fractures: Analysis of Commonly used Reservoir Scale Models,” Annual Technical Meeting of the Center for Advanced Material Processing (CAMP), Canandaigua, NY, May 17-19, 2006.

D. Crandall, G. Ahmadi and D.H. Smith, “Two-Phase Flow Analogies to Flow through Porous Media,” Annual Technical Meeting of the Center for Advanced Material Processing (CAMP), Canandaigua, NY, May 17-19, 2006.

D. Crandall, K. Nazridoust, G. Ahmadi, G. Bromhal and D.H. Smith, "Volume of Fluid Simulations of Multiphase Flow through Fractures: Analysis of Individual Fractures for Application in Reservoir Scale Models," Computational Methods in Water Resources XVI International Conference (CMWR XVI), Copenhagen, Denmark, June 18 – 22, 2006